A Comparative Study of Two Copper(II) Based Metal-Organic Frameworks: $Cu_{2\frac{1}{4}}(OH)_{\frac{1}{2}}B4C{\cdot}8H_2O$ and $Cu_2Na(OH)B4C{\cdot}7H_2O$

A thesis submitted in fulfilment of the requirements for the degree of

Master of Science

to

Rhodes University

by

Matthew Coombes

March 22, 2013

Abstract

This study focussed on two copper(II)-containing metal-organic frameworks (MOFs): $Cu_2Na(OH)B4C{\cdot}7H_2O$ and $Cu_{2\frac{1}{4}}(OH)_{\frac{1}{2}}B4C{\cdot}8H_2O$ (B4C = 1,2,4,5-benzenetetracarboxylate). They are both covalent, three-dimensional metal-organic framework polymers containing voids filled with water molecules. Both were characterised by elemental analysis, infrared spectroscopy, X-ray powder diffractometry (both *in situ* and regular), thermogravimetric analysis, differential scanning calorimetry and X-ray photoelectron spectroscopy. These two MOFs are essentially identical, with the only difference being the substitution of sodium by copper at every 4th site (disordered throughout the crystal).

The guest inclusion properties of both MOFs were studied and compared. Although both structures collapse on dehydration, it was observed that $Cu_2Na(OH)B4C{\cdot}7H_2O$ is able to take up significant amounts of water, methanol and ethanol. All these processes are fully reversible. Car-Parrinello molecular dynamics studies suggest that it is a strong interaction between the oxygen atoms on these molecules with the sodium cation of the MOF that is responsible for this significant uptake.

In contrast, $Cu_{2\frac{1}{4}}(OH)_{\frac{1}{2}}B4C{\cdot}8H_2O$, the MOF without a sodium cation, did not demonstrate any methanol or ethanol uptake, but was able to take up some water. The uptake of water, however, is not a fully reversible process. The absence of sodium likely results in insufficient energy to draw methanol and ethanol into the framework, while a subtle rotation of a carboxylate group on dehydration decreases the ability of the framework to form hydrogen bonds, thus reducing the ability to take up water.

A series of hydrothermal syntheses were performed in order to develop a method of synthesis superior to the current gel-based synthesis that requires several months and has poor yields. The hydrothermal products were characterised by elemental analysis, infrared spectroscopy, X-ray powder diffractometry, thermogravimetric analysis and differential scanning calorimetry. It was shown that the MOF $Cu_2Na(OH)B4C{\cdot}7H_2O$ may be synthesised in almost 100% yield by using a temperature of 120°C over a period of 72 hours.

It was not possible to synthesise $Cu_{2\frac{1}{4}}(OH)_{\frac{1}{2}}B4C{\cdot}8H_2O$ in a 100% yield - it was only obtained as a minor product.

Acknowledgements

I would like to acknowledge the following people for their help throughout the course of this thesis. Unfortunately these few words can not fully convey how much their assistance is appreciated:

- Prof. G. M. Watkins and Dr K. A. Lobb, for their supervision and guidance over the course of this thesis.
- Dr B. G. Anderson (SASOL R&D), for his support and assistance with all things SASOL related.
- Mr F. Chindeka and Mr J. Fourie, for their assistance in repairing the aging thermal analysis equipment time and time again.
- Mr A. Adriaan and Mr R. Douglas, for their assistance with all the odd jobs that I needed done.
- Dr E. Hosten (NMMU Chemistry Department), for the sodium and copper ICP-MS data, and Mr F. Chindeka for the CHNS microanalysis.
- The NIC, for the use of their XRPD and XPS instruments. In particular, I would like to thank Dr E. Antunes for her assistance in collecting the XPS data and for allowing me time on NIC instruments to gain practical experience.
- Dr E. du Plessis, Dr R. Forbes and Dr S. Lubhelwhana (SASOL R&D), for their assistance in collecting *in situ* XRPD data.
- Dr E. Hosten (NMMU Chemistry Department), Prof. S. Bourne (UCT Chemistry Department) and Mr A. Gerisch (Bruker AXS GmbH), for their attempts at solving the single crystal structure of Cu-B4C-Needles.
- Mr M. Randall (Rhodes Electron Microscopy Unit), for the acquisition of SEM images.

- Mrs B. Tarr, Ms B. L. Ah Yui, Ms G. Cobus, Ms M. Juleka and Mr. A. Nxopo, for their assistance in administrative matters.
- Mr I. Hodgson, Mr. A. Sobola, Ms T. Olalekan, Mr C. Mkhize and Mr U. Mpiti, my labmates, for their assistance, company and support.
- All friends and colleagues in the Chemistry Department, for all manner of assistance and thought-provoking discussion.
- Friends and family, for their support.
- SASOL, for funding my studies.

Contents

List of Figures

List of Tables

CCD Nomenclature

Table 1 contains the CCD abbreviation codes used in this thesis, together with their appropriate chemical formulae. Additionally, products synthesised during this work that are not yet deposited in the CCD also have their abbreviation codes given.

Table 1: CCD nomenclature used in this thesis.

Code	**Chemical Formula**
DIXGIB	$CuNa_2(H_2O)_8(H_2B4C)_2{\cdot}2H_2O$
HIFPOC	$(C_2H_{10}N_2)_2Cu_2(H_2O)_2(B4C)_2{\cdot}4H_2O$
HIFPUI	$(C_2H_{10}N_2)Cu(B4C)_2{\cdot}2.5H_2O$
MOFJEW	$Cu(H_2O)_3(H_2B4C){\cdot}3H_2O$
BOVTAH	$Cu_2(H_2O)_6B4C{\cdot}4H_2O$
MURBOQ	$Cu_2(H_2O)_4B4C{\cdot}2H_2O$
MURCEH	$Cu_3(OH)_2B4C$
NEHRAU	$(C_5H_{11}N)_2Cu_2(H_2O)_6(H_2B4C)_2{\cdot}3H_2O$
MEMGAN	$(C_3H_{12}N_2)CuB4C{\cdot}2H_2O$
xst-cu-b4c-rhombi	$Cu_4Na_4(B4C)_3{\cdot}14H_2O$
Cu-B4C-Xtals	$Cu_2Na(OH)B4C{\cdot}7H_2O$
Cu-B4C-Needles	$Cu_{2\frac{1}{4}}(OH)_{\frac{1}{2}}B4C{\cdot}8H_2O$

1 Introduction

1.1 Metal-Organic Frameworks

Metal-organic frameworks (MOFs) are an intriguing class of hybrid materials that exist as infinite crystalline lattices comprised of inorganic vertices (in the form of metal or metal oxides) and molecular-scale organic linkers which connect these inorganic vertices.[1] This description accounts for both MOFs which contain voids, often filled with guest or solvent molecules, and those which do not. Void-containing MOFs are often described as porous in the literature, although true porosity is only exhibited when the guest molecules may be exchanged with other guest molecules without loss of framework integrity. In this case, the MOF is termed an open-MOF.[2]

Whilst MOFs are structurally similar to the alumino-silicate-based zeolites, the major difference is found in the organic group linking the inorganic vertices, which may be functionalized to an almost limitless extent.[3–5] Since the organic linker is partly responsible for the properties of a given MOF, this functionalisation allows for a certain property to be tuned, or an entirely new property introduced. The type of metal vertex also contributes towards the properties of a given MOF. In addition, the pore size may easily be adjusted, to give pores ranging from several angstroms to several nanometres, by simply changing the length of the organic linker.[6] As with zeolites, synthesis is typically via a hydro(solvo)thermal method. However, other methods of synthesis have been used, such as ambient precipitation methods,[7] gel-synthesis (as is the case with the MOFs studied here), microwave assisted synthesis[8,9] , ultrasound assisted synthesis[10,11] and mechanochemical synthesis.[12] Formation of the crystalline framework takes place via the self-assembly of structural units to form an ordered network of metal-organic coordination bonds.

A wide variety of metals have been used in the synthesis of MOFs, although the most common in the literature are those of transition metals, specifically zinc and copper, owing to their versatility.[13] Organic molecules have tended to be mostly rigid aromatic compounds containing O-donor

groups. This favours the formation of highly crystalline and stable MOFs. The most common organic linkers used are 1,4-benzenedicarboxylate and 1,3,5-benzenetricarboxylate. However, MOFs with flexible ligands have been synthesised,[14] as well as MOFs containing N-donor ligands.[15]

It has been shown that the synthetic conditions play a large role in determining the resulting MOF that is formed. Changes in these conditions often result in the product failing to form, a product having a completely different three-dimensional structure, or a mixture of two or more different products. These conditions include, but are not limited to, temperature and pH,[16,17] solvent used during the synthesis,[17] and metal-to-ligand ratio.[18] In order to produce a MOF with vacant pores, the guest solvent molecules need to be removed, a process termed activation. This is commonly achieved by heating. The temperature and method (should a method different to heating be chosen) by which a MOF is activated is also critical, and can trigger collapse of the framework, resulting in much less porosity than one would expect.[19]

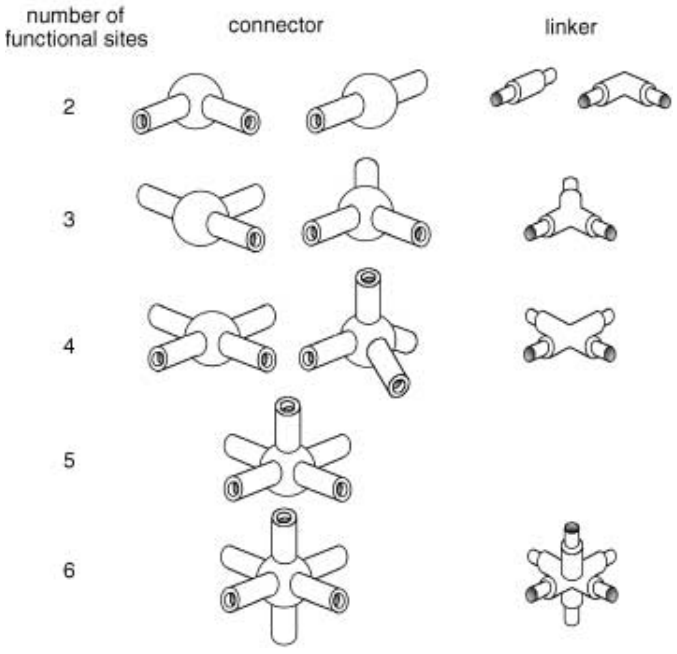

Figure 1: Several of the various geometries obtainable with different metal connectors and organic linkers.[13]

The most important factors in metal connectors and organic linkers to consider are the number and orientation of their binding sites (coordination number and coordination geometry respectively). Depending on the metal and its oxidation state, coordination numbers can range from 2 through to 7, resulting in a myriad of different possible geometries, some of which are visualised in figure 1. When this wide variety of connector and linker geometries is combined into a MOF, the results are hugely varied, as shown in figure 2.

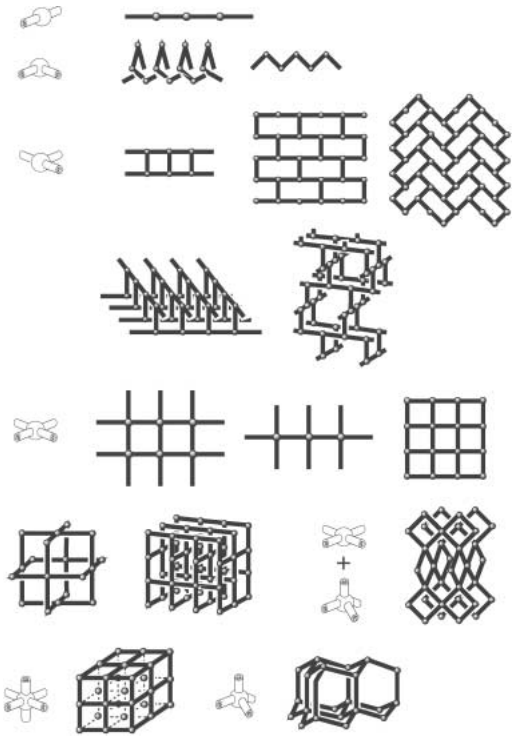

Figure 2: A sample of the wide variety of different possible 3-dimensional structures that are attainable in MOFs.[13]

MOFs can be categorized into two classes: rigid or flexible (dynamic).[20] Rigid MOFs usually have comparatively stable and robust porous frameworks with permanent porosity, similar to zeolites, whereas flexible MOFs possess dynamic, soft frameworks that respond to external stimuli, such as pressure, temperature, and guest molecules. This extraordinary sensitivity

to external stimuli affords MOFs special properties not observed in other adsorbent materials such as zeolites.

1.2 Uses of Metal-Organic Frameworks

MOFs have an extremely wide variety of possible uses. Some of the main features responsible for this include the functionalities of both their metal cluster and their organic linker ligand, the presence of micropores, large specific surface areas and, in some cases, high thermal stability.

1.2.1 Gas Storage

Gas storage is arguably the most popular topic of discussion when one considers MOFs. As with most solids, such as zeolites and activated carbon, the quantity of gas taken up is mainly affected by the surface area and pore size of the material. It is the extremely large, record-breaking specific surface areas of MOFs that make them most attractive for gas storage purposes. Some examples* are MOF-177[21] with a high surface area of 4500 $m^2.g^{-1}$, MIL-101[22] having a surface area of 5900 $m^2.g^{-1}$ and UMCM-2[23] which possesses a surface area of over 5200 $m^2.g^{-1}$. This allows large amounts of a given gas to be taken up (for a given mass of MOF) by the framework.

Hydrogen storage is of particular interest to the clean energy community, since hydrogen is readily obtainable from water and offers a much higher energy density than common petroleum based fuels per mass unit (nearly 3 times).[24] Hydrogen is held within a MOF by weak physisorption forces. Typical heats of adsorption are -4 $kJ.mol^{-1}$ for HKUST-1 and MOF-177[25] and -6.7 $kJ.mol^{-1}$ for $Cr_3(BTC)_2$.[26] These MOFs demonstrate hydrogen uptakes (by weight) of 3.6 wt%, 7.5 wt% and 1.9 wt% respectively.[27] However, these values are obtained at 77 K and approximately 70 bar pressure. It has been proposed that heats of adsorption in the range -20 $kJ.mol^{-1}$ to -25 $kJ.mol^{-1}$ are necessary for hydrogen storage at ambient temperatures.[28]

Studies have shown that hydrogen stored in MOFs is bound to open metal sites and concentrated in narrow pores.[26,29] This suggests that the key

*The surface areas quoted are obtained via the BET method.

factors influencing hydrogen storage in MOFs are the availability and high density of open metal sites and long, narrow pores. These pores should have an optimum diameter not much larger than twice the kinetic diameter of the hydrogen molecule (2.9 Å)[30] as this results in tighter packing of gas molecules in the adsorbed state.

Carbon dioxide capture has also elicited much interest from researchers, mainly because of the gas's greenhouse effects and a general global trend towards more environmentally friendly processes. When compared to the current benchmark materials for carbon dioxide capture (namely MAXSORB and zeolite 13X), MOF-177 stores twice as much carbon dioxide (at room temperature and approximately 40 bar pressure).[31] In addition, a cylinder filled with MOF-177 can hold 9 times as much carbon dioxide as an empty cylinder under the same temperature and pressure conditions. This is illustrated in figure 3.

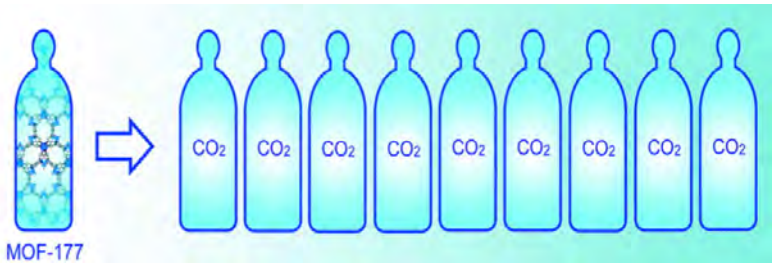

Figure 3: A visual illustration of the extraordinary carbon dioxide storage capabilities of MOF-177[31].

As with hydrogen, open metal sites appear to be favourable binding sites for carbon dioxide. This attraction is mainly electrostatic in nature and occurs between the negative quadrupole moment of the carbon dioxide molecule and the positively charged open metal sites.[32] This type of interaction has the added advantage of being able to separate (quadru)polar/non-polar gas pairs and this has been demonstrated with the MOF series CPO-27-M (M = Ni, Mg), where carbon dioxide was separated from binary mixtures of carbon dioxide and methane/nitrogen.[33] Certain MOFs containing flexible ligands have demonstrated "breathing" modes (this relates to structural changes of

the framework) which aid in the selective uptake of carbon dioxide.[34,35] Post-synthetic modifications of DMOF-1 have shown that the length of an alkyl chain has an effect on these breathing modes.[36]

Unlike hydrogen, the heats of adsorption are considerably larger, ranging from 20 kJ.mol^{-1} to 50 kJ.mol^{-1} for most MOFs,[37] while some[38] have been reported to have heats of adsorption up to 90 kJ.mol^{-1}. It is important to note that a higher heat of adsorption is not necessarily good in terms of the carbon dioxide storage or separation because of the large energy requirement associated with the desorption of the gas from the MOF.

Apart from hydrogen storage and carbon dioxide capture and separation, MOFs have been used for methane storage and separation[39] as well as the separation of short chain hydrocarbons.[40,41] It is important to note that in all cases, the large surface area and controlled pore geometries of the MOF play an important role. In addition, the chemical tunability of the MOF (either through the nature of the metal centres or functionalities of the organic linker) also plays a vital role.

1.2.2 Heterogeneous Catalysis

Zeolites are extensively used in the industry as shape-selective catalysts,[42] since they possess a well-defined system of pores and cavities, as well as high thermal stability and the possibility of introducing functional sites on the cavity walls. With this in mind, it would seem that MOFs are good candidates for selective and active heterogeneous catalysts, owing to their tunable porosity, large surface areas and essentially limitless possibilities for functionalization. However, their use as catalysts has been rather limited to date. The reason for this is two-fold.[43,44] Firstly, MOFs are not as stable towards high temperature, moisture and some reactants and impurities. This is a result of the weaker metal-ligand bond in the MOF, when compared to the strong silicon-oxygen bond in zeolites. Secondly, the coordination sphere around the metal ion is often completely blocked by the organic linker and as such, the metal ion is unavailable to participate in the reaction. However, certain MOFs have part of this coordination sphere filled with solvent

molecules and removal of these results in open metal sites.[45,46]

In general, there are three possible ways that a MOF may be responsible for catalytic activity.

The first is by providing an active metal site. The catalytic activity observed for these MOFs is directly related to their metallic vertices, be they isolated metal centers, clusters,[6] chains[47] or sheets.[48] These MOFs may be further subdivided[42] into MOFs containing only one type of metal ion, in which case the metal ion serves as both the catalytic site and the inorganic vertex, or a bimetallic MOF in which one metal is the active catalyst whilst the other performs only a structural role within the framework.

The second way is through the presence of a reactive functional group. As the name suggests, the catalytic activity in this case is associated with a particular functional group of the organic linker. Suitable linkers must contain both coordinating groups to bind to the metal vertices, as well as unbound functional groups to catalyze a given reaction. The number of MOFs falling into this group is small. The requirement that the reactive group be free and accesible to the substrate of interest is the limiting factor in this regard. Some examples of these MOFs include L-proline-based ligands in MIL-101 catalyzing asymmetric aldol reactions[49] and a cadmium based MOF incorporating 1,3,5-benzene tricarboxylic acid *tris*[N-(4-pyridyl)amide] that showed excellent activity and recyclability when performing a Knoevenagel condensation reaction.[50]

The third possibility involves the use of the MOF simply as a host matrix.[42] In this case, reactions occur within the numerous pores of the MOF without the metal vertices or organic linkers themselves being directly involved in the reaction.

1.2.3 Sensors

A sensor is a device that measures a physical quantity and converts it into a signal, which may then be detected by an instrument or observer and subsequently read. Important factors to consider with regards to chemical sensors are sensitivity, selectivity, response time, material stability, and reusability.

Whilst the use of MOFs as sensors has not been as well studied as for gas separation and storage, the exceptional tunability of both the MOF structure and its properties, as well as its recyclability and specificity should give them an advantage over other classes of chemo-sensory materials.[51]

Sensing in MOFs takes on many different forms, the most common being luminescence-based sensing. Luminescence can be caused by a variety of different processes.[52] The first of these is linker-based luminescence, which is often exhibited by the conjugated linkers used in MOFs. It is either centred on the ligand, or involves a charge transfer to or from the metal vertices.[53–55]

The second process involves the metal ions at the vertices of the MOF. Lanthanoid ions are often employed in this regard since they emit sharp, but weak luminescence from forbidden Laporte transitions (f-f).[52] There is also minimal peak broadening from solvent effects, since the $4f$ orbitals (where the transitions occur) are shielded by the $5d$ orbitals. Proximity to an organic fluorophore, either within the framework or adsorbed within the pore, can produce an antenna effect and a pronounced increase in the luminescence intensity.[56,57]

Other processes include MOF pores trapping luminescent molecules in an otherwise non-emisive framework, as well as $\pi - \pi$ interactions between adjacent conjugated linkers,[58] or between a linker and a guest molecule, that produces an excited complex.[59]

Solvatochromism is another sensing mechanism in MOFs, and is arguably the simplest. It involves a large shift in the absorption spectrum of a material in response to a change in the identity of the guest solvent, producing a visible colour change which is easy to detect. In some cases the polarity of the solvent affects the difference in the dipole moment between the ground and excited states[60] (charge transfer) whilst in others it changes the coordination sphere of the metal ions at the vertices.[61]

Other forms of sensing which do not involve the absorption or emission of light include measurement of the refractive index of the MOF, which changes depending on the nature and quantity of included guest molecule.[51] Detection may be via interferometry[62] or surface plasmon resonance spectroscopy,[63] where MOFs are used to preferentially concentrate the analyte of interest.

1.2.4 Other

MOFs have found uses in a variety of other fields. The very well-defined pores have been used to synthesise metallic nanoparticles within a very small size range.[64,65] These nanoparticles may be left within the framework to serve as a catalyst on support system, or the framework may be disintegrated to obtain isolated nanoparticles.

The tunable pore size of MOFs and ability to functionalize the framework play an integral role in the potential of MOFs for use as drug storage and drug delivery devices. The organic linkers allow for a wide range of biocompatabilities whilst the inorganic vertices help with the controlled release of the drug.[66] The one major drawback of MOFs in this regard is that their pores are nanosized, really limiting the size and number of drug molecules that may be taken up by the framework. Certain mesoporous MOFs have been synthesised and shown to take up a large amount of drugs and release them at a controlled rate.[67] Initial desorption of the drug from the MOF was via the simple process of diffusion, whilst the drug released after a longer period of time was more strongly bound to the framework by $\pi - \pi$ interactions (between the drug and framework aromatic groups).

1.3 Copper(II) Based Structures Incorporating H_xB4C (where x = 1-4)

Quite a number of compounds involving copper(II) and 1,2,4,5-benzenetetracarboxylic acid (H_4B4C), or any one of its deprotonated anions, have been reported in the literature. A survey of the Cambridge Structural Database* (CSD) yielded 61 structures incorporating the copper(II) cation and H_xB4C (where x = 0,1,2,3, or 4, dependent on the degree of deprotonation). Of these structures, 38 contain fully deprotonated B4C and 18 contain the doubly-protonated form. Only two of the structures contain a monoprotonated form, whilst the remaining one was singly deprotonated.

Of theses structures, 52 are mixed-ligand systems involving nitrogen-

*The search was performed using Conquest 1.14[68] and the 2012 release of CSD.[69]

donor ligands togther with the B4C. Two of these systems have the B4C anion present merely as a counter ion,[70,71] whilst the remaining structures contain the B4C in a coordinated environment. In some cases, the B4C exists as a non-bridging ligand,[72–75] whilst in others it is bridged with copper(II) to form dimers or tetramers,[71,76,77] infinite linear chains,[72,78–85] two-dimensional sheets[77,82,86–90] or fully covalent three-dimensional, coordination structures.[70,77,82,91–107] Those compounds that do not have a fully covalent three-dimensional coordination structure generally contain a hydrogen bonding network that combines the sheets or chains into a three-dimensional supramolecular network.

The remaining nine structures do not contain any coordinated organic ligands apart from B4C. Any other organic groups are present as either solvents or as cationic counter ions. Each of these structures is detailed below, and is referred to by its CSD reference code. The chemical formula for each of these CCD structures is given in table 1. All images are generated from the CIF files, obtained from the CSD, using PLATON software.[108]

DIXGIB is a heteronuclear sodium- and copper(II)-containing structure containing a partly deprotonated 1,2,4,5-benzenetetracarboxylic acid.[109] It is synthesised under ambient conditions via the slow evaporation of the solvent (in this case a methanol/water mixture in a ratio of 2:3). The product crystallises into the monoclinic spacegroup with a C2/m symmetry. The unit cell is visualised in figure 4. Both the sodium and copper(II) cations exist in distorted octahedral environments. The sodium atom is coordinated to two carboxyl oxygen atoms from two B4C ligands and four oxygen atoms of four bridging water molecules. The copper(II) atom is coordinated to six water molecules in which four are bridging and two are non-bridging. The bridging water molecules regularly link one copper(II) and two sodium atoms to form a one-dimensional linear chain. An extensive network of hydrogen bonding is present in the structure which joins all the chains into a three-dimensional network. No other form of characterisation has been reported for this structure.

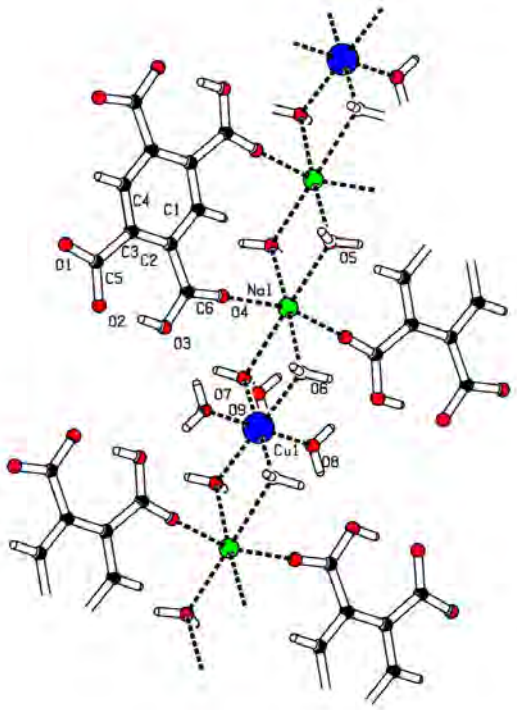

Figure 4: The crystal structure of DIXGIB showing atomic positions and how the bridging waters combine the sodium and copper(II) centres into an infinite linear chain (blue = copper, red = oxygen, green = sodium, black = carbon).

The coordination polymer HIFPOC consists of two-dimensional anionic sheets of copper(II) coordinated to B4C, counterions in the form of ethylenediammonium, and free waters.[110] A copper(II) ion in a distorted square-based pyrimidal geometry is coordinated to four separate carboxylic oxygens (from separate B4C anions), with the axial site being occupied by a water oxygen. These anionic layers are separated by an ethylenediammonium cation and two free water molecules. An extensive network of N-H--O and O-H--O hydrogen bonds connects these sheets into a three-dimensional supramolecular

structure. The asymetric unit is visualised in figure 5.

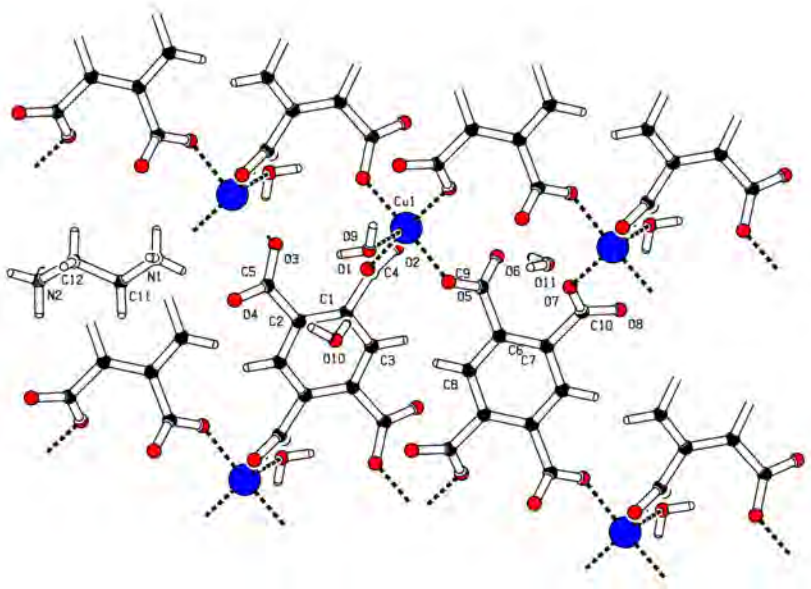

Figure 5: The crystal structure of HIFPOC, illustrating the coordination between copper(II) and B4C, as well as the positions of the ethylenediammonium cations (blue = copper, red = oxygen, black = carbon, violet = nitrogen).

The supramolecular structure HIFPUI has been reported by two separate groups[110,111] and is very similar to HIFPOC above. Its crystal structure is visualised in figure 6. It also contains anionic sheets comprising of copper(II) coordinated to B4C. These sheets are topologically homologous to the ones of HIFPOC above. These sheets are once more separated by ethylenediammonium cations, acting as counter-ions, and free waters, with the hydrogen-bonded network present to create a three-dimensional supramolecular structure. The only difference between HIFPUI and HIFPOC is that the copper(II) cation in this case is in a square-planar geometry, with the axial water no longer present in the structure. In addition, a further free water molecule is disordered over two sites. Both of these supramolecular structures (HIFPOC and HIFPUI) are synthesised via the slow evaporation of

solvent under ambient conditions. Slight differences in synthetic conditions are present in the formation of HIFPOC (solution corrected to pH 4.0) and HIFPUI (solution corrected to pH 3.0). This is a good example to illustrate the role of synthetic conditions on the product obtained when looking to synthesise a given MOF.

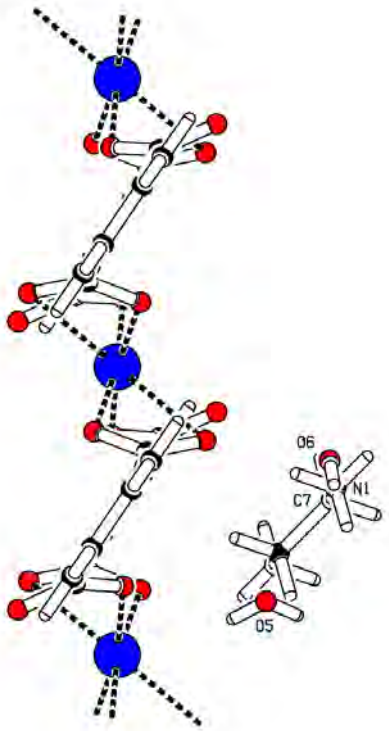

Figure 6: The crystal structure of HIFPUI, illustrating a slight staggering in the sheets as a result of the coordination environment, as well as the position of the ethylenediammonium cation (blue = copper, red = oxygen, black = carbon, violet = nitrogen).

Copper(II)-B4C compounds containing just water in the voids have also been synthesised.[112,113] The coordination polymer MOFJEW has copper(II) surrounded by three coordinated water molecules and two carboxyl groups, from two separate H_2B4C groups, in a five-coordinate, distorted trigonal

bipyramidal environment. The copper(II) ions are bonded in a monodentate form to oxygen atoms of different H_2B4C ligands. These oxygen atoms are located on opposite sides of the benzene ring and as a result, the copper(II) ions are linked by ligand molecules. These bonds form an infinite linear chain as illustrated in figure 7.

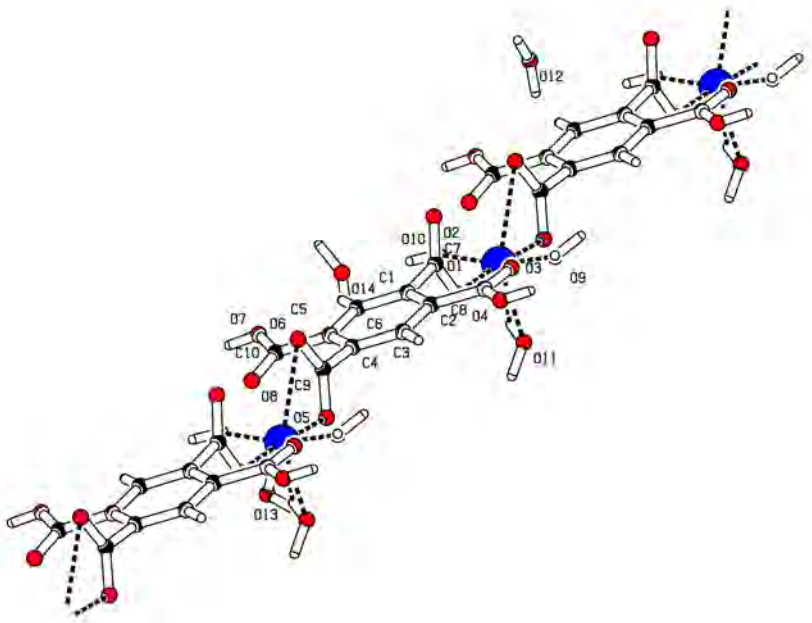

Figure 7: The crystal structure of MOFJEW showing the one-dimenstional chains and the hydrogen-bonding network (blue = copper, red = oxygen, black = carbon).

There are three additional water molecules of crystallisation in this structure that remain uncoordinated. These are involved in medium and long range hydrogen bonds. The H_2B4C ligand is an acceptor of two medium and three long hydrogen bonds from water molecules. The coordinated water molecules are donors to one medium and two long hydrogen bonds. The H_2B4C ligand is a donor of two medium hydrogen bonds to these waters of crystallisation. All these hydrogen bonds were confirmed using infrared and Raman spectroscopies, as well as through computer simula-

tions. This hydrogen-bonded network combines the linear chains into a three-dimensional supramolecular structure.

The thermal behaviour of this polymer has also been studied.[113] Thermal gravimetric analyis (TGA) indicates that on heating, the three coordinated and three uncoordinated water molecules are lost between 71°C and 180°C. Differential thermal analysis (DTA) shows that this is an endothermic process with an activation energy of 134.75 kJ.mol^{-1}. There are a further two mass loss stages. These occur between 180°C and 280°C, and 280°C and 320°C. They correspond respectively to the loss of the two uncoordinated carboxy groups followed by the loss of the remaining organic residue, with the final residue being copper(II) oxide. No attempts were reported concerning the reversibility of the initial water loss step.

Additionally, the copper(II)-B4C structure BOVTAH has also been synthesised.[92,112] As with MOFJEW, each copper(II) centre exists in a distorted trigonal bipyramidal geometry and is coordinated to two carboxyl oxygens from two separate B4C ligands. However, the B4C anion in this case is fully deprotonated and coordinates to four different copper(II) cations. The water molecules of crystallisation occupy the remaining coordination sites. As a result, the structure is comprised of two-dimensional sheets, rather than a linear chain. This is visualised in figure 8. Finally, additional waters of crystallisation occupy the voids between the sheets. They are involved in medium and long hydrogen bonds with the ligand and each other, resulting in a three-dimensional supramolecular structure together with the copper(II)-B4C sheets. Both BOVTAH and MOFJEW are synthesised under ambient conditions.

Figure 8: The crystal structure of BOVTAH, illustrating the coordination of B4C to 4 different copper(II) cations to form a 2-dimensional sheet. The vacant voids contain water molecules (not shown in the figure) (blue = copper, red = oxygen, black = carbon).

MURBOQ is a copper(II)-B4C complex having rectangular channels of dimensions 6.5 x 4.5 Å.[102] All of the carboxylic acid groups of the B4C ligand are deprotonated. Each of two *p*-carboxylate groups of B4C adopts a bidentate bridging coordination mode with a copper(II) cation, while each of the other two adopts a monodentate coordination mode, and the whole ligand acts as a μ_6-bridge linking six copper(II) ions. This is visualised in figure 9. The copper(II) ion exists in a square-based pyramidal geometry. The coordination sites in the equatorial plane are occupied by two carboxyl oxygens and two water oxygens, whilst the axial coordination site is occupied by a third carboxyl oxygen. This results in the formation of staggered two-dimensional sheets. These are connected via hydrogen bonds to form the channels mentioned earlier. The channels are occupied by waters of crys-

tallisation. The structure is synthesised under ambient conditions using a water-methanol mixture as a solvent. The solution was corrected to a pH of 4.0. It is interesting to note that while water is present in the structure, no methanol was present either as a coordinated molecule, or as a guest in the rectangular channels.

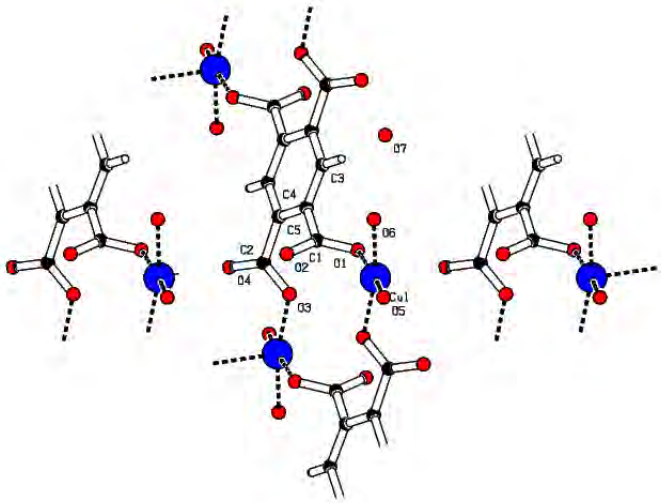

Figure 9: The crystal structure of MURBOQ showing the staggered two-dimensional sheet structure and the μ_6-bridging of the B4C ligand (blue = copper, red = oxygen, black = carbon).

The first and only example of a hydrothermally synthesised Cu(II)-B4C structure in the literature is MURCEH.[102] The precursors used in the synthesis were heated in a 1:1 methanol-water solution at 140°C for two days. The resulting product consisted of green, block-like crystals. The structure, visualised in figure 10, contains two crystallographically distinct copper(II) cations. One is coordinated by two hydroxide oxygen atoms and two oxygen atoms from bridging carboxylate groups in a square planar geometry; the other is coordinated by two hydroxide oxygen atoms, one oxygen from a monodentate carboxylate group, and one oxygen from a bridging carboxylate group in a slightly distorted square planar geometry. The coordination environment of these copper(II) cations is, however, square-based pyramidal, with the axial positions being occupied by the other copper(II) cation.

This results in a paddlewheel dinuclear metal centre, a structural feature of HKUST-1,[114] one of the first MOFs to be properly studied.

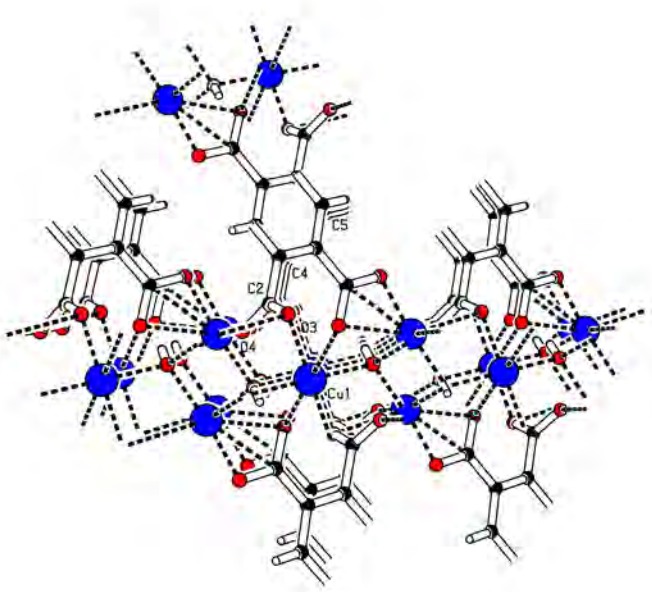

Figure 10: The crystal structure of MURCEH showing the dinuclear copper(II) paddlewheel and the coordination between the copper(II) cations, B4C ligands and hydroxy oxygens (blue = copper, red = oxygen, black = carbon).

The coordination environment of the B4C ligand is similar to MURBOQ above, with two of the carboxylate oxygens adopting a monodentate mode of coordination, while the other two demonstrate a bidentate coordination mode. Each dinuclear copper(II) unit links four separate B4C ligands to form a two-dimensional porous layer structure. The layers are further connected by links through copper(II)-oxygen bonding from the remaining oxygen atoms of bridging carboxylate and hydroxy groups, completing the μ_3-bridging and yielding a final three-dimensional structure with channels of 7.4 x 9.6 Å.

NEHRAU is an example of a coordination polymer that has been synthesised via a slow diffusion method[115] whereby separate solutions of the reagents (in this case dipiperidine 1,2,4,5-benzenetetracarboxylate and cop-

per(II) perchlorate hexahydrate) were placed in the opposite arms of an H-tube and the two solutions, in direct contact with each other, were allowed to diffuse into one another. At the interface of the precursor solutions, blue crystals of the product were formed.

Each of the copper(II) ions is five-coordinate in a square-based pyramidal geometry and is coordinated to five oxygen atoms. The axial position, as well as two planar positions, is occupied by water molecules, while the remaining two positions are occupied by oxygen atoms from two different H_2B4C molecules. As a result, infinite one-dimensional chains are produced. An extensive hydrogen-bonding network exists between these chains, the uncoordinated dipiperidine and uncoordinated 1,2,4,5-benzenetetracarboxylic acid molecules to produce a three-dimensional supramolecular structure. Unfortunately, the CIF file deposited in the CSD is incomplete (it lacks 3D coordinates for the atoms), and as such the structure could not be visualised.

TGA indicates that the uncoordinated dipiperidine as well as water is lost when heated to 127°C. This led the authors to study the dehydration/rehydration behaviour of this structure. A sample was heated to 130°C for 3 hours, whereafter it was exposed to water vapour at room temperature for 24 hours. X-ray powder diffraction was used to monitor the process, as seen in figure 11. On heating, there was a disappearance of characteristic peaks, indicating that the sample had changed structure. On rehydration, it was shown that the sample was not restored to its original form, but rather to an alternate structure, a phenomenon common in many zeolites. This is most often a result of distortion of the pore shapes and sizes.[116]

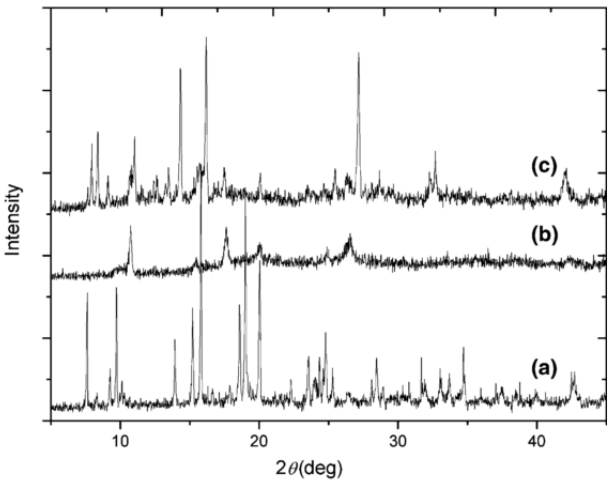

Figure 11: XRPD patterns for NEHRAU. (a) Taken at room temperature, (b) after heating at 130°C for 3 hours, (c) after rehydration of sample for 24 hours at room temperature in the presence of water. Of interest is the change in structure on heating, as well as the different structure that is formed on rehydration.

MEMGAN is a three-dimensional structure containing trimethylenediammonium cations as a templating agent within the crystal voids.[117] In the first coordination sphere the copper(II) ions are coordinated to four carboxylate oxygen atoms (figure 12) from four different B4C anions yielding a coordinaton geometry that is tetrahedrally distorted/square-planar. An additional four oxygen atoms from the same carboxylate groups are located around the copper(II) at larger distances, forming a distorted sphenoid. If these secondary, longer copper(II)-oxygen bonds are ignored, then every B4C anion acts as *tetrakis*-monodentate ligand bridging four copper(II) ions. In this way a three-dimensional framework is produced.

The framework has two sets of channels, which are large enough to accommodate species such as the trimethylenediammonium cations and water molecules. The first, wider channels extend parallel to the [1,1,0]/[1,−1,0] directions and contain the guest trimethylenediammonium cations, which are oriented perpendicular to the channel axis. These channels have an elongated octagonal cross section with approximate dimensions of 7 x 3 Å and occupy some 30% of the cell volume. The second, narrower channels are rectangular

in cross-section and run parallel to the c-axis of the crystal. They contain water molecules and constitute 10% of the cell volume. TGA indicates that the two guest water molecules are lost in a single-step process between 46°C and 150°C. The dehydrated framework is stable up to 219°C, whereafter it decomposes. It was not indicated whether this water loss was reversible or not, or whether there was a structural change accompanying this water loss.

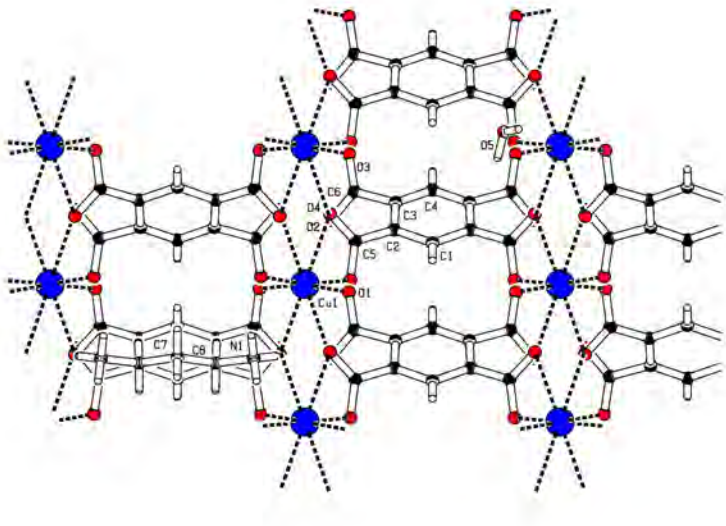

Figure 12: The crystal strucutre of MEMGAN showing the coordination sphere of the copper(II) cations and the position of the B4C anions (blue = copper, red = oxygen, black = carbon).

The final structure to be discussed in this section is xst-cu-b4c-rhombi. This structure is not present in CSD, but is instead reported in a PhD thesis.[118] It is a covalent three-dimensional metal-organic framework comprised of two crystallographically distinct copper(II) ions and two sodium cations. It contains two fully deprotonated B4C units, one a μ_{10}-type and the other a μ_{11}-type. Both the sodium cations, as well as both copper(II) ions, are found in distorted octahedral geometries. The basic unit of xst-cu-b4c-no3-rhombi is visualised in figure 13. A total of 13 water molecules per four copper(II)/sodium ions are trapped in the voids created by the framework.

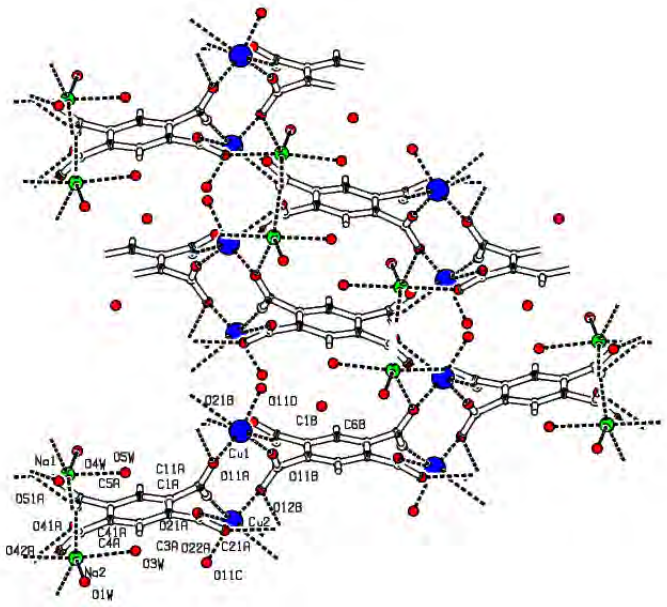

Figure 13: The crystal strucutre of xst-cu-b4c-rhombi demonstrating the arrangement of copper(II), sodium and B4C units, as well as the positions of the water molecules within the voids (blue = copper, red = oxygen, black = carbon, green = sodium).

xst-cu-b4c-rhombi is synthesised via the slow diffusion of either a copper(II) sulfate, nitrate or chloride solution into a sodium metasilicate gel impregnated with B4C. It forms over a period of several months alongside three other products. These products are BOVTAH and MURBOQ (discussed above) and $Cu_{2\frac{1}{4}}(OH)_{\frac{1}{2}}B4C{\cdot}8H_2O$, one of the MOFs of interest in this thesis.

Upon heating, all 13 void waters are lost by 165°C in three overlapping steps, as evidenced by TGA. The framework also transforms to a new structure, as evidenced by the XRPD pattern of the dehydrated material. The dehydrated framework remains stable just beyond 300°C, whereafter the framework decomposes. DSC data only indicated two endothermic steps prior to 165°C which corresponded to the second and third of the mass loss steps observed with TGA. This suggests the water lost during the first mass loss step is very weakly bound.

The dehydrated compound was investigated for its guest inclusion capabilities with water and methanol. It demonstrated a partial restoration to its orignal structure on exposure to water. It was proposed that the formation of new coordination bonds during the dehydration process resulted in changes to the framework that could not be fully reversed upon exposure to water vapour. Uptake of methanol by the dehydrated framework was not observed.

1.4 The MOFs $Cu_2Na(OH)B4C{\cdot}7H_2O$ (Cu-B4C-Xtals) and $Cu_{2\frac{1}{4}}(OH)_{\frac{1}{2}}B4C{\cdot}8H_2O$ (Cu-B4C-Needles)

The MOF $Cu_2Na(OH)B4C{\cdot}7H_2O$, hereafter referred to as Cu-B4C-Xtals, as well as the MOF $Cu_{2\frac{1}{4}}(OH)_{\frac{1}{2}}B4C{\cdot}8H_2O$, hereafter referred to as Cu-B4C-Needles, are both synthesised via a gel-based method.[118] Cu-B4C-Needles, as mentioned in chapter 1.3, is synthesised alongside xst-cu-b4c-no3-rhombi, BOVTAH and MURBOQ. Cu-B4C-Needles is synthesised via the same procedure, with the use of copper(II) acetate as the source of copper(II) ions as opposed to copper(II) nitrate, sulfate or chloride.

At the time of synthesis, Cu-B4C-Needles was shown to be essentially isostructural to Cu-B4C-Xtals, based on near identical X-ray powder diffraction data, mid-infrared spectra and thermal analysis data. However, the crystal structure of Cu-B4C-Needles was not determined at the time and as a result, the MOF was only characterized at a rudimentary level. It has been hypothesised that the only difference between Cu-B4C-Xtals and Cu-B4C-Needles is the substitution of the sodium cation by a copper(II) cation at every fourth site, with the hydroxy group for charge balance. Comparison of these two systems will thus allow logical deductions to be made as to what role the presence (or conversely the absence) of the sodium cation might play in the guest inclusion behaviour of this class of MOFs. Since Cu-B4C-Xtals is well characterized, the important results are summarised here.

The gel synthesis of Cu-B4C-Xtals may take on one of two forms. The first involves the impregnation of 1,2,4,5-benzenetetracarboxylic acid in a sodium metasilicate gel, corrected to a pH of approximately 6.5 (chapter 2.1.1 contains more information regarding this choice of pH). The B4C-impregnated

gel is contained in a straight-tube. A solution of copper(II) acetate is then added and the straight tube is covered and allowed to stand at 40°C. The second method makes use of a U-tube. In this case, the sodium metasilicate gel (once again corrected to pH 6.5) is in the middle of the U-tube, and separate solutions of 1,2,4,5-benzenetetracarboxylic acid and copper(II) acetate are added to either arm. In both cases the solutions diffuse through the gel, forming large single crystals of Cu-B4C-Xtals after several months. This period of time is too long should there be a need to produce Cu-B4C-Xtals in bulk. As such, a faster method of synthesis, such as a hydrothermal synthesis, is required.

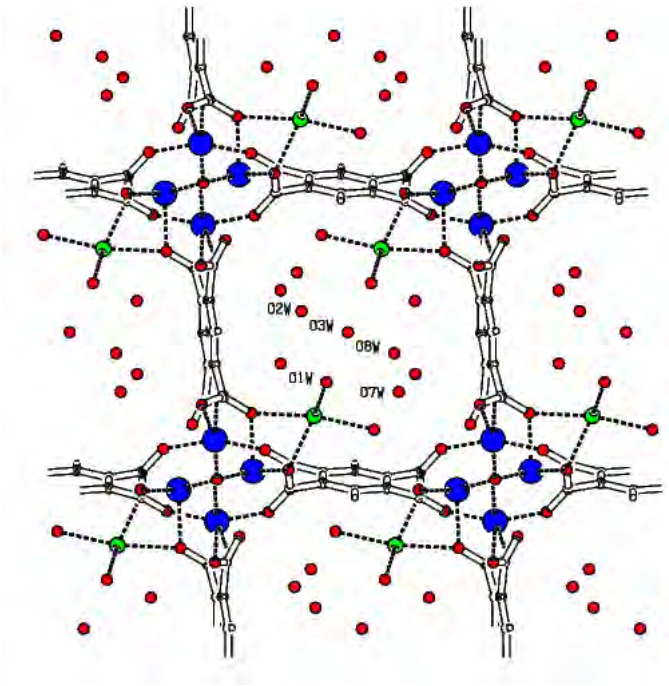

Figure 14: Crystal structure of Cu-B4C-Xtals illustrating the large cavities containing guest water molecules (blue = copper, red = oxygen, black = carbon, green = sodium)

Structurally, Cu-B4C-Xtals is a three-dimensional metal-organic framework consisting of tetrameric copper(II) clusters linked together by 1,2,4,5-benzenetetracarboxylate ligands. The structure is traversed by channels

which contain guest water molecules, as shown in figure 14. There are two types of 1,2,4,5-benzenetetracarboxylate anion: the one type is μ_{10}-bridging and makes up the floor (or ceiling) of the channels as shown; the other is μ_8-bridging and makes up the walls of the channels.

The SBU[2] of this metal-organic framework is shown in figure 15. Two crystallographically equivalent copper(II) ions (2) are doubly linked by μ_3-bridging oxygens, believed to be hydroxides, which also link this pair of copper ions to non-equivalent copper(II) atoms (1) as shown. The interatomic distance for the hydroxo-bridged Cu(2)-Cu(2) pair is 2.912 Å. Cu(1) and Cu(2) pairs are linked together by bridging carboxyl groups, as shown. Sodium cations are present, coordinated to the carboxyl oxygen atoms as shown. The copper(II) ions and the sodium ions all exist in distorted, square based pyrimidal geometries.

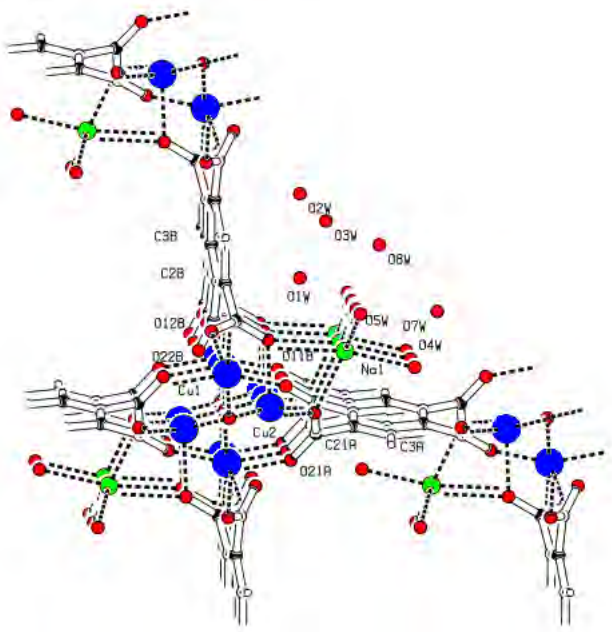

Figure 15: The SBU of Cu-B4C-Xtals illustrating the nature of the metal vertices, the position of the sodum cations and the water-containing voids (blue = copper, red = oxygen, black = carbon, green = sodium).

Some ambiguity exists regarding the number of guest water molecules

present in the channels of Cu-B4C-Xtals. Crystallographic data suggests the presence of eight water molecules per formula unit, whilst thermal analysis strongly suggests the presence of seven. The TGA of Cu-B4C-Xtals is shown in figure 16. Three steps are evident in the thermogram. The first two steps are overlapping, and correspond to a loss of six water molecules. These two steps are endothermic, as evidenced by DSC, with an enthalpy change of 420.5 $J.g^{-1}$ of parent material. The third step occurs over a broad temperature range and corresponds to the loss of the remaining water (or two waters, should you assume there are 8 included water molecules per formula unit). Loss of this final water molecule is followed by the irreversible decomposition of the MOF into metallic copper, carbon and sodium hydroxide. This suggests that some of the water molecules, likely those which are coordinated to the sodium centres, play a vital roll in the structural stability of the MOF.

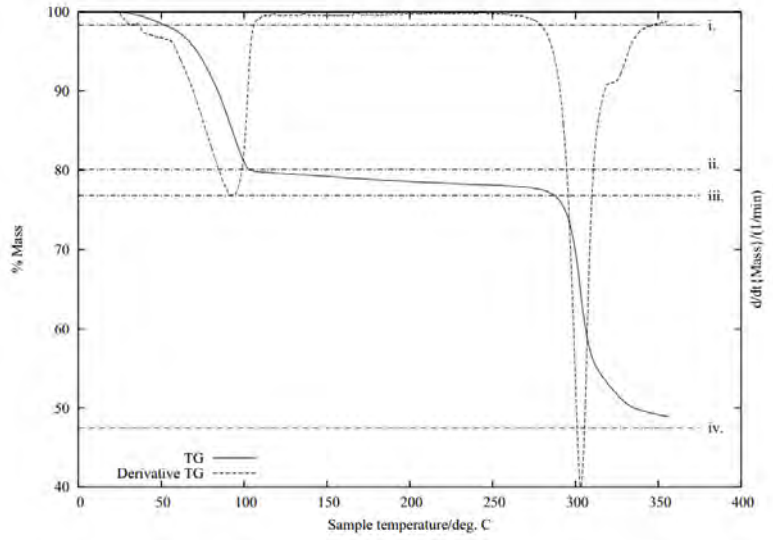

Figure 16: TGA thermogram for Cu-B4C-Xtals heated at 10°C.min[1] under nitrogen.

Cu-B4C-Xtals was investigated for its guest inclusion behaviour with a wide range of solvents*. The MOF was first activated by removing 6 of the guest water molecules. This was achieved by heating the MOF to 150°C in a nitrogen atmosphere. The activated MOF was then placed in a sealed dessicator that was saturated with the solvent vapours of interest and left for 24 hours.

On activation, the MOF was shown to transform to a different crystal structure. However, instrument limitations at the time resulted in partial rehydration during X-ray powder diffraction runs and so it was not certain to what extent the framework changed. On exposure to water and methanol, large amounts of solvent were taken up by the MOF. Uptake of water resulted in the MOF returning to an identical crystal structure, whilst methanol uptake resulted in an almost identical structure to the original MOF (as evidenced by XRPD data). Ethanol was also taken up by the activated MOF, but in much smaller amounts and at a very slow rate. The majority of the included water, methanol and ethanol were removed by heating to just over 100°C. However, evolved gas analysis indicated that some solvent did indeed come off just prior to decomposition at 300°C, suggesting that the solvents were actually substituting for the coordinated water in the framework. It was further shown that the MOF was recyclable with regards to water and methanol, as it survived multiple activation-rehydration steps with these guest solvents. Figure 17 is a DSC thermogram indicating the repeatable uptake of methanol and water after successive activation-rehydration steps. None of the other solvents demonstrated any appreciable uptake, in fact some of them appeared to break the framework down.

*The solvents included water, methanol, ethanol, formaldehyde, acetaldehyde, pyridine, acetonitrile, N,N'-dimethylformamide, formamide, dimethylsulfoxide and carbon disulfide. Water, methanol, ethanol and pyridine were investigated initially,[118] whilst the remaining solvents were investigated shortly after.[119]

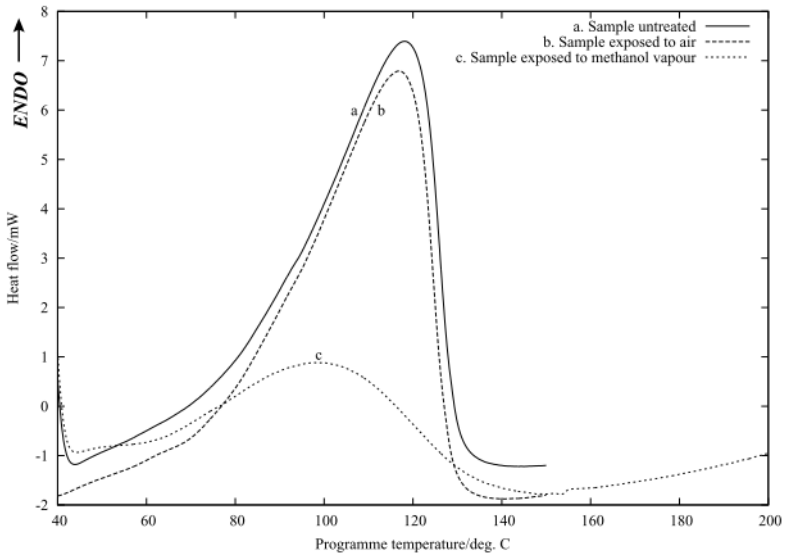

Figure 17: DSC thermogram for Cu-B4C-Xtals heated at 10°C.min^{-1} under nitrogen, showing the repeatable uptake of methanol and water.

The guest-inclusion behaviour of Cu-B4C-Needles has not been studied. Since the only difference between Cu-B4C-Needles and Cu-B4C-Xtals is the presence of the sodium cation, a study of the guest inclusion behaviour of Cu-B4C-Needles (comparing it to Cu-B4C-Xtals) will provide valuable insight into the role played by the sodium cation in this class of MOFs.

1.5 Aims of the Study

The aims of this study were threefold:

- Further characterise the MOFs Cu-B4C-Xtals and Cu-B4C-Needles to gain a greater understanding of the subtle difference in structure between these two MOFs.
- Study the guest inclusion behaviour of Cu-B4C-Needles and compare with Cu-B4C-Xtals in order to gain insight into the role played by the sodium site of Cu-B4C-Xtals.
- Attempt hydrothermal syntheses of Cu-B4C-Xtals in order to accelerate the rate of synthesis.

2 Experimental

2.1 Synthesis

2.1.1 Synthesis of Cu-B4C-Xtals ($Cu_2Na(OH)B4C{\cdot}7H_2O$)

1.00 g of 1,2,4,5-benzenetetracarboxylic acid (H_4B4C - 3.9 mmol) was added to 25 mL of deionized water. The solution was heated to dissolve all the H_4B4C and to remove any dissolved air. 5 mL of sodium metasilicate stock solution* was added to the H_4B4C solution. The pH of the metasilicate-H_4B4C solution was adjusted to 6.5† by the slow addition of acetic acid‡. The pH was measured using a pH meter. The gel solution was poured into the bottom half of a boiling tube, covered with aluminium foil and allowed to set overnight at 40°C.

1.56 g of copper(II) acetate ($Cu(Ac)_2{\cdot}H_2O$ - 7.8 mmol) was dissolved in 25 mL of deionized water. The resulting solution was then *slowly* added to the top of the H_4B4C-containing gel, in order to leave the surface of the gel undisturbed. The boiling tube was covered with aluminium foil and kept at 40°C. Square, blue-green crystals of Cu-B4C-Xtals formed over a period of approximately 4-6 months.

2.1.2 Synthesis of Cu-B4C-Needles ($Cu_{2\frac{1}{4}}(OH)_{\frac{1}{2}}B4C{\cdot}8H_2O$)

1.00 g of 1,2,4,5-benzenetetracarboxylic acid (H_4B4C - 3.9 mmol) was added to 25 mL of deionized water. The solution was heated to dissolve all the H_4B4C and to remove any dissolved air. 5 mL of sodium metasilicate stock solution was added to the H_4B4C solution. The pH of the metasilicate-H_4B4C

*The sodium metasilicate stock solution had a concentration of 488 $g.L^{-1}$, and was prepared as described in literature.[120]

†The optimum pH for rapid gelling of sodium metasilicate solutions is 8.[120] However, straight-tube experiments with various metals at this pH, and slightly higher, failed at times, owing to the fact that the metals were being trapped by the formation of insoluble hydroxides.[118] Better results were obtained for these metals at a pH of 6.5, thus 6.5 is used as the starting pH.

‡Acetic acid was chosen as its conjugate base is acetate, the anion of the copper(II) salt to be used.

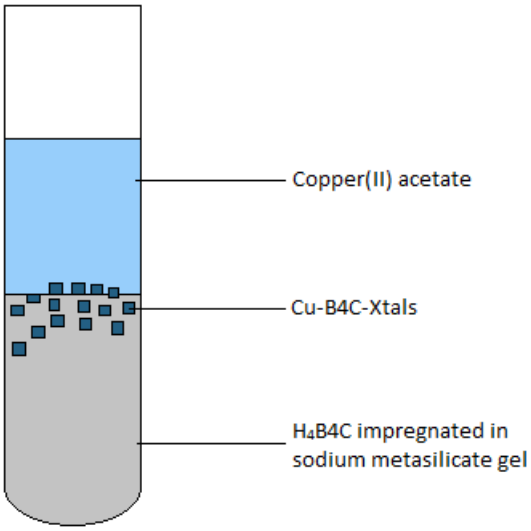

Figure 18: Experimental setup for the synthesis of Cu-B4C-Xtals after a period of 3 months.

solution was adjusted to 6.5 by the slow addition of hydrochloric acid.* The pH was measured using a pH meter. The gel solution was poured into the bottom half of a boiling tube, covered with aluminium foil and allowed to set overnight at 40°C.

1.32 g of copper(II) chloride ($CuCl_2 \cdot 2H_2O$ - 7.8 mmol) was dissolved in 25 mL of deionized water.† The resulting solution was then *slowly* added to the top of the H_4B4C-containing gel, in order to leave the surface of the gel undisturbed. The boiling tube was covered with aluminium foil and kept at 40°C. Multiple products formed over a period of several weeks, one of which was long, blue-green needles of the Cu-B4C-Needles, which formed after 6-8 weeks. The other products are MURBOQ, BOVTAH and Xst-Cu-B4C-Rhombi and these have been discussed previously in chapter 1.3.

*Hydrochloric acid was chosen as its conjugate base is chloride, the anion of the copper(II) salt to be used.

†It is also possible to synthesise Cu-B4C-needles using 1.88 g of copper(II) nitrate ($Cu(NO_3)_2 \cdot 3H_2O$ - 7.8 mmol) or 1.95 g of copper(II) sulfate ($CuSO_4 \cdot 5H_2O$ - 7.8 mmol) instead.[118] The gel should then be corrected to pH 6.5 using nitric acid or sulfuric acid respectively.

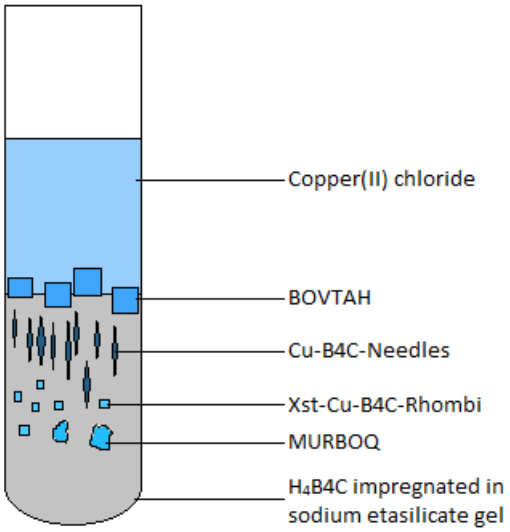

Figure 19: Experimental setup for the synthesis of Cu-B4C-Needles after a period of 2 months.

2.1.3 Hydrothermal Syntheses

The first products that were synthesised were those with a varying starting pH*. The temperature conditions were kept constant in all cases. The general synthesis procedure for Cu-B4C-Na-acet-X (where X = pH4, pH5, pH6, pH6.5) was as follows:

> 1.006 g (3.96 mmol) of H_4B4C was dissolved in 25 mL deionized water. In a separate beaker, 1.581 g (7.92 mmol) of copper(II) acetate and 1.078 g (13.1 mmol) of sodium acetate were dissolved in 25 mL of deionized water. The two solutions were then combined in a Berghof BR-300 high pressure reactor, with a 230 mL TEFLON® insert. The resulting solution, which immediately demonstrated the formation of a blue precipitate, was pH corrected to the appropriate pH by the dropwise addition of NaOH (1 $mol.L^{-1}$). The pH was measured using a pH meter.

*For the rationale behind the choice of reagents and reaction conditions, please see appendix C.

The resulting mixture was then subjected to a temperature programme, with the details for each sample given in table 2. Upon completion, the sample was allowed to cool naturally to room temperature. Thereafter it was vacuum filtered and washed with deionised water. All products were green-tinged, blue powders, except Cu-B4C-Na-acet-pH6.5 which was a grey-blue colour.

These syntheses were moderately successful in their attempt to synthesise either Cu-B4C-Xtals or Cu-B4C-Needles. The details of their characterisation are presented in chapter 3.3. What was evident was that the syntheses at pH 6 and above resulted in the formation of copper(II) oxide deposits on the side of the TEFLON® insert. Since pH 5 and pH 4 yielded similar results, it was decided to use pH 5 in the temperature dependent syntheses. The reasoning behind this was to introduce the maximum amount of fully deprotonated B4C as possible. It was also decided to pH correct the H_4B4C solution first, before addition to the copper(II) acetate, as it was believed that some of the precipitate forming initially was Cu_2B4C·0.65H_2O. The aim was to eliminate the formation of this (or any other) undesired phase.

As such, the general synthesis procedure for Cu-B4C-Na-acet-X (where X = 12h, 48h, 72h, short, cool, glass) was as follows:

1.006 g (3.96 mmol) of H_4B4C was dissolved in 25 mL deionized water and pH corrected to 5.0 by the dropwise addition of NaOH (1 mol.L^{-1}). The pH was measured using a pH meter. In a separate beaker, 1.581 g (7.92 mmol) of copper(II) acetate and 1.078 g (13.1 mmol) of sodium acetate were dissolved in 25 mL of deionized water. The two solutions were then combined in a Berghof BR-300 high pressure reactor, with a 230 mL TEFLON® insert. The sample to be run in glass was placed in a glass vessel prior to insertion into a metal autoclave. The resulting mixture was then subjected to a temperature programme, with the programme conditions for each sample given in table 2. Upon completion, the sample was allowed to cool naturally to room temperature. Thereafter it was vacuum filtered and washed with

deionized water. All products were blue powders with a green tinge.

Table 2: The various temperature programmes for each of the hydrothermal syntheses. All samples were initially at room temperature. All heating and cooling rates were 10°C.min^{-1}. Upon completion of the temperature programme, all samples were allowed to cool to room temperature.

Sample	**Temperature Programme**
Cu-B4C-Na-acet-pH4	120°C (24 hr) → 100°C (12 hr) → 80°C (12 hr)
Cu-B4C-Na-acet-pH5	120°C (24 hr) → 100°C (12 hr) → 80°C (12 hr)
Cu-B4C-Na-acet-pH6	120°C (24 hr) → 100°C (12 hr) → 80°C (12 hr)
Cu-B4C-Na-acet-pH6.5	120°C (24 hr) → 100°C (12 hr) → 80°C (12 hr)
Cu-B4C-Na-acet-12h	120°C (12 hr) → 100°C (12 hr) → 80°C (12 hr)
Cu-B4C-Na-acet-48h	120°C (48 hr) → 100°C (12 hr) → 80°C (12 hr)
Cu-B4C-Na-acet-72h	120°C (72 hr) → 100°C (12 hr) → 80°C (12 hr)
Cu-B4C-Na-acet-cool	100°C (12 hr) → 80°C (12 hr)
Cu-B4C-Na-acet-short	120°C (0 hr)
Cu-B4C-Na-acet-glass	120°C (48 hr) → 100°C (12 hr) → 80°C (12 hr)

2.2 Characterisation Techniques

2.2.1 Microanalysis

CHNS analysis was performed on a Vario MICRO V1.6.2 elemental analysis system. Copper content was determined using both an iCAP 600 series ICP-OES spectrometer (Cu(II) detected at wavelengths of 224.7, 221.8 and 213.5 nm) and a Perkin Elmer AAnalyst 200 Atomic absorption spectrometer (with a copper lamp). Additionaly copper and sodium content was determined using a Perkin-Elmer Elan 6100 ICP-MS (Plasma power 1100 W and Ar flow rate 0.99 L/min). For CHNS analysis, samples were used as is. Copper and sodium analysis required the samples to be digested in concentrated nitric acid prior to solutions being made.

CHNS analysis is a form of gravimetric analysis whereby the analyte of interest (in this case carbon, nitrogen, hydrogen and sulfur) is separated from all other elements by converting it to a gas of known chemical composition.[121] The mass of this gas then serves as a measure of the concentration of the analyte within the sample. In this manner, the weight percentages of carbon, nitrogen, hydrogen and sulfur may be obtained.

ICP, AAS and flame ionization spectrometry make use of either the emission or absorption of photons of a very specific energy. The energy of the photons is determined by the difference in energy between the intial and final states, ΔE, and this is dependant on the nature of the atom or ion emitting or absorbing the energy.[122] As such, unique energies are observed for different elements. Absorption measurements have an advantage over emission measurements, mainly in that their signal-to-noise ratio is better.[123]

All these techniques combine to yield empirical formulae for the synthesised MOFs. It is important to know which elements are present in the structure, as well as the relative amounts of each of these. From this information, one can start drawing conclusions on the nature of coordination, the number and coordination environment of the metals at the vertices, as well as the number and type of guest molecules. While this is not conclusive on its own, it does provides invaluable insight into the structure when combined with the techniques described below.

2.2.2 Infrared Spectroscopy

A Perkin-Elmer Spectrum 100 FT-IR spectrometer with ATR attachment was used in this study. Wavenumbers between 4000 cm^{-1} and 650 cm^{-1} were scanned. A total of four scans were collected. The instrument resolution was 4 cm^{-1}. All samples were baseline corrected and smoothed using Spectrum version 6.3.5 software.

Transitions between vibrational levels within a molecule occur between 10000 and 100 cm^{-1}. Infrared spectra originate from transitions between a vibrational ground state and excited state, and are observed as absorption spectra in the infrared region.[124] The number and position of these transitions is a reflection of the structure of the molecule of interest, and may be used to validate a certain structural model.[124] Unfortunately, the symmetry of a molecule in the crystalline state is generally lower (as a result of intermolecular interactions) than in the isolated (gaseous) state. As such, the IR spectra must be interpreted with caution.

The bands in the IR spectrum that are of interest are mainly the COO stretches, observed between 1300 cm^{-1} and 1650 cm^{1}. By observing the difference between the ν(C=O) and ν(C–O) vibrations (alternatively, the ν_a(C=O) and ν_s(C=O) vibrations respectively, depending on the symmetry of the carboxylate group), and comparing it to the value obtained for Na_4B4C ($\Delta\nu$ = 95 cm^{-1}), one may determine the nature of coordination of the carboxylate group.[102] Values greater than this are indicative of a unidentate binding mode, values lower than this indicate a bidentate mode and values that are approximately the same suggest a bridging mode of coordination. This trend is also observed for sodium acetate and corresponding metal acetato complexes.[124]

2.2.3 X-ray Powder Diffraction

The X-ray powder diffraction patterns were recorded on a Bruker D8 Discover X-ray powder diffractometer, using copper K_α radiation (λ_1 = 1.54060 Å, λ_2 = 1.54439 Å, ratio = 0.5) and a nickel filter. The generator tube was operated at a potential of 40 kV and a current of 40 mA. The divergence slit

width was 0.6 mm and the primary Soller slit 4.0°.

In situ X-ray powder diffraction patterns were collected using an Anton Paar XRK600 coupled to the Panalytical XPert Pro multi-purpose diffractometer, with a cobalt source. The tube voltage was 40 kV and the tube current was 50 mA. The anti-scatter slit was 2° and the Soller slit 2.29°.

When X-rays of a given wavelength impinge on a target, they are scattered by each of the atoms in the target, with the scattering for a crystalline sample being goverened by the Laue equations.[125] However, it is more practical to view these X-rays as reflecting off of the lattice planes of the crystalline sample. This is governed by the Bragg equation, $n\lambda = 2d\sin\theta$ where n is an integer, λ is the wavelength of the X-ray, θ is the angle of impingement and d is the distance between 2 successive lattice planes. From the positions of these reflections i.e. the value of θ, the elements of the unit cell may be determined.[126] This includes lattice vectors (both magnitude and relative angles) as well as the relative atomic coordinates within the unit cell.

Since the X-ray reflections will change position with a change in the structure of a crystalline solid, X-ray powder diffraction may be used to to determine whether two MOFs have the same or similar structure, as well as whether the MOF has changed structure on activation or upon the uptake of various guest molecules. This is especially important in evaluating whether a MOF has been successfully activated or not. Unsuccesful activation is usually noticable as a large change in the crystal structure, as well as a decrease in crystallinity. Successful activation usually involves only small structural changes as well as a slight shrinking of the unit cell volume.

2.2.4 Thermogravimetric Analysis

A Perkin-Elmer TGA 7 thermogravimetric analyzer with Pyris version 4.01 software was employed in this study. A powdered sample (see discussion at the end of this section as to why a powdered sample was used) of known mass (approximately 2 mg) was heated from 50°C to 650°C at a rate of 10°C.min^{-1} under a nitrogen atmosphere (flow rate 20 ml.min^{-1}). The mass of the sample was recorded throughout the heating profile.

TGA is a technique in which the mass of a sample is measured against time (or temperature) while the temperature of the sample, in a controlled atmosphere, is programmed.[127] By following all the effects of heat on the changing mass of the sample, it is possible to obtain information on the various stages of analysis and the temperatures required to bring about their completion.

For MOFs, this is of particular importance for two reasons. Firstly, guest molecules need to be removed from within the voids in order to provide free void space for the uptake of other guest molecules.[50,114] TGA allows one to see at which temperature the various guests are removed. It is also invaluable in structural elucidation, to determine the number of guest solvent molecules within the framework.

Upon removal of the guest molecules, the MOF is only stable up to a certain temperature. This is one of the major limiting factors in using MOFs as heterogeneous catalysts.[43] As such, the second major importance of TGA is that it can provide invaluable insight into what value this temperature is for a given MOF.

The nature of the sample is of importance in the acquisition of thermal analysis data.[128] Differences are observed with differences in particle size, with the best samples being a packing of fine powders. This is a result of fine particles having a better thermal conductivity than a loose collection of larger grains. As such, the samples for this experiment, which are originally obtained as large crystals, were ground into a fine powder prior to analysis to ensure consistency across all the runs.

2.2.5 Differential Scanning Calorimetry

DSC thermograms were collected using a Perkin-Elmer DSC 7 differential scanning calorimeter, employing the power-compensating principle, with Pyris version 4.01 software. A powdered sample of known mass (approximately 5 mg) and a reference were heated from 40°C to 500°C at a rate of 10°C.min^{-1} under a nitrogen atmosphere (flow rate of 20 ml.min^{-1}). The difference in the power supplied to the furnaces of the sample and reference is recorded.

In power-compensating DSC instruments, the aim is to maintain the sample and reference material at the same temperature throughout the controlled temperature programme.[127,129] Any energy-requiring process in the sample (exothermic or endothermic) will tend to change the temperature of the sample. The difference in power that is supplied by the instrument in order to maintain a constant temperature in both sample and reference materials is recorded. Quantification of the peak area for a given process is assumed to be proportional to the enthalpy change, ΔH.[129]

The enthalpy associated with removal of various guest molecules is of particular importance for MOFs, particularly in the fields of gas-storage and seperation. Should the enthalpy, which is a measure of the interaction energy between the guest molecules and the MOF, be too low, the guest molecule's own thermal energy will be sufficient to overcome the arising interaction forces.[130] On the other hand, high interaction energies make it difficult to remove certain guest molecules from the MOF, an undesirable situation given the possibility of using MOFs as leaner, more efficient alternatives for various storage and separation applications.

2.2.6 X-ray photoelectron Spectroscopy

A Kratos Axis Ultra DLD, equipped with aluminium (monochromatic) anode and charge neutraliser was used for all scans.

Wide XPS scans were performed with an emmission current of 10 mA and the anode (HT) at 15 kV. The operating pressure was below 5×10^{-9} torr. A hybrid lens was used and the resolution to acquire survey scans was at 160 eV pass energy in slot mode. The centre used for the scans was at 520 eV and the width at 1205 eV, with a step size of 1 eV and a dwell time of 500 ms.

For high resolution scans, the resolution was changed to 40 eV pass energy in slot mode with a step size of 0.1 eV and a dwell times of 500 ms for each element. The centre and width for each scan respectively is summarized in table 3:

Table 3: The centre and width energies for each of the high-resolution XPS runs.

Element	**Centre [eV]**	**Width [eV]**
C 1s	288.5	23
O 1s	543	22
O 2s	24	23
Cu 2p	946	50
Cu 3p	110	50

Etching runs were performed using the wide scan parameters. An argon ion gun (4kV) was used to etch each sample for 5 s (x10).

XPS is based on the photoelectric effect, whereby a photon may remove an electron from a sample if the photon has an energy greater than the electron binding energy.[131] By bombarding the sample with photons of a fixed energy, and measuring the energy of ejected electrons, once may determine the binding energy of the ejected electrons. These are dependent on the chemical environment of the atom from which they are ejected. Thus, XPS may be used to understand differences in the chemical environment of various atoms within the sample. Specifically for these copper(II)-based MOFs, it is of interest to study the copper(II) ions, as well as the oxygen and carbon atoms with the MOF, in order to gain a deeper insight into the nature of their chemical environments.

2.2.7 Scanning Electron Microscopy

The scanning electron microscope (SEM) employed in this study was a TESCAN Vega TS 5136LM, operated at 20 kV and at a working distance of 20 mm. Each sample of hydrothermally synthesised MOF was coated with gold using a gold sputter machine before imaging to prevent electrostatic charging.

As with all microscopes, a SEM produces a magnified image of the sample of interest. It achieves this by targeting the sample with a beam of electrons

of a certain energy. A variety of different images may be produced depending on whether backscattered electrons, Auger electrons, secondary electrons, or characteristic X-rays are collected and recorded.[132] While the uses of SEM are hugely varied, it was employed in this study simply to observe the microcrystalline structure of the hydrothermally synthesised products in order to determine whether a mixture of products had formed.

2.2.8 Molecular Dynamics

Initially, density functional theory (DFT) geometry optimizations were performed on the guest molecules of interest using the guassian03 software.[133] B3LYP was chosen as the functional and 6-31G(d) as the basis set. The cartesian coordinates of the crystal unit cell, with six of the eight void waters removed, were obtained from the cif file and, using simple translations, these guest molecules were placed in the unit cell of the crystal.

The molecular dynamics was performed using the CPMD code,[134] which makes use of plane wave basis sets and periodic boundary conditions. As a result of the periodic boundary conditions, only the atoms within 1 unit cell of the framework need to be described. The BLYP functional was chosen for this study. Martins-Troullier norm-conserving pseudopotentials were used for the copper atoms, whilst the ultrasoft Goedecker-type pseudopotentials were chosen for the remaining atoms. The dynamics involved three stages, with each following from the previous:

1. A geometry optimization was performed on the crystal structure, making use of a DIIS algorithm,[135] as well as Anderson mixing.[136]

2. An equilibration run was performed to temper the initial high forces of the crystal structure that would otherwise destroy it. The equilibration run made use of a fictitious electron mass of 600 at a variety of temperatures.

3. The dynamics run was performed, using a timestep of 4.0 a.u (4.0 a.u. = 0.0967554 fs). The resulting trajectory was visualised using the VMD program.[137]

Molecular dynamics simulation begins with the imparting of kinetic energy to each of the constituent atoms of a system. It is then possible to calculate how these atoms are moving by solving the Newtonian equations of motion. As such, one can then predict the motion of all atoms within the system over a very short duration.[138]

For modelling chemical interactions, the preferred technique is usually considered to be quantum mechanical in nature. However, if the whole system is to be described explicitly, the large number of atoms makes *ab initio* quantum mechanics* impractical,[139] since large computational power is required. However, the Car-Parinello (CP) approach[140] alleviates some of the computational requirement. The CP approach involves the electronic and nuclear dynamics being performed simulatneously. The CP method of simulation does not require the electronic configuration of the system to be at a minimum in coefficient space for each molecular dynamics time step.[139]

While models like these are not perfect replicas of the system under consideration, they do emphasise particular features of a chemical system which agree with what is known about molecules in general. As a result, they are capable of providing links between observation and theory.[141] In this study it is achieved through a visualisation of the interactions between guest solvent molecules and the host framework at a molecular level. This provides additional insight into the nature of the interaction that is not readily obvious using the other techniques employed in this study.

2.3 Desolvation/Resolvation Technique

The sample to be desolvated was placed in an aluminium or platinum pan† and weighed, prior to heating in a DSC furnace from 40°C to 150°C at 10°C.min^{-1}. The sample was held at 150°C for a further 10 min. This is to ensure that all loosely bound water molecules are removed. The sample was allowed to cool before reweighing. It was *immediately* placed in a dessi-

**Ab initio* quantum mechanics involves the solution of the Schrödinger wave equation, usually via an iterative procedure.

†The platinum pan was used for sample to be characterized by TGA, all other techniques made use of an aluminium pan.

cator that was saturated with the vapours of the guest molecules of interest. The sample remained in the dessicator for 24 hours. This was to allow the vapours sufficient time to diffuse through the dehydrated MOF and interact with it. Finally, the sample was weighed once more prior to characterisation by either TGA, DSC, IR or XRPD.

3 Characterisation

3.1 Cu-B4C-Xtals ($Cu_2Na(OH)B4C{\cdot}7H_2O$)

Although Cu-B4C-Xtals has been well characterised[118] and reported in chapter 1.4, several additional techniques have been used in the characterisation of Cu-B4C-Needles. Since comparison is to be made between Cu-B4C-Xtals and Cu-B4C-Needles, it is prudent that these other techniques also be applied to Cu-B4C-Xtals. As such, they are presented in the following section.

3.1.1 X-ray Powder Diffraction

During the desolvation/resolvation procedure of Cu-B4C-Xtals, an XRPD pattern was collected of a dehydrated sample i.e. one with 6 of the 7 formula waters removed. This showed the presence of new peaks indicating a change in structure. However, the original powder pattern was also evident in that of the dehydrated sample, which suggested either that the structure remained largely the same upon dehydration, or that the sample rehydrated in the presence of moisture in the air. *In situ* XRPD was used to gain more insight into the dehydration (activation) process.

The *in situ* data, presented in figure 20, shows 3 distinct regions, labeled I, II and III. Region I, which was obtained at 30°C, is the original structure with all the water molecules in the voids.

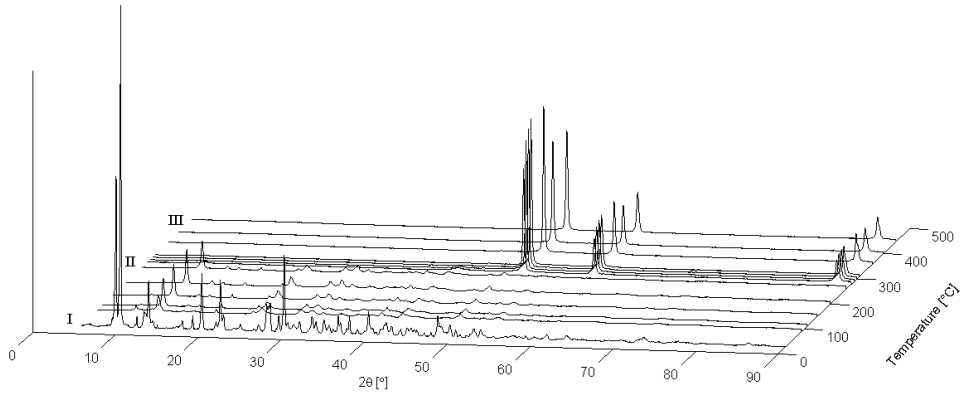

Figure 20: *In situ* XRPD pattern of Cu-B4C-Xtals under helium. The data shows 3 separate regions, corresponding to the original structure, the dehydrated structure and the decomposition products.

On heating to 90°C, there is an immediate change in phase to that represented in region II. The identity of this phase is unknown. It is known (based on the TGA evidence) that water molecules are being lost at this stage. As such, the phase represented in region II is that of the dehydrated material. It is evident that this does not have any of the peaks corresponding to the 100 family of reflections in the original sample. The disappearance of certain peaks corresponding to the original sample, together with the emergence of new peaks suggests a change to a new structural phase on dehydration, rather than the original framework remaining intact. This is further illustrated in figure 21, which shows the disappearance of peaks corresponding to the original sample (labeled A) and the appearance of new peaks (labelled B), indicating the formation of a new phase. This suggests that the previously reported dehydrated XRPD obtained previously[118] was not a true reflection of the dehydrated structure, but rather that the sample had rehydrated in the presence of moisture in the air.

Additionally, it must be noted that the dehydrated sample shows broader peaks than those of the original sample. This is indicative of a decrease in crystallite size, thus it appears the sample loses crystallinity during the dehy-

dration process. The final transformation is to the decomposition products, which in this case are metallic copper and carbon. The carbon is likely to be X-ray amorphous, thus only metallic copper is expected to be visible. This is indeed the case, as confirmed by pattern fitting using TOPAS[142] software.

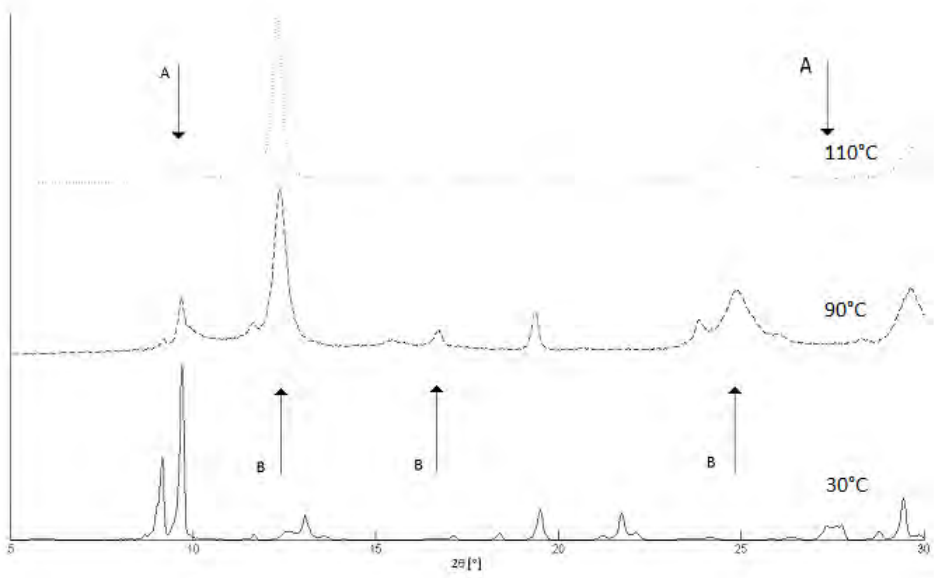

Figure 21: *In situ* XRPD pattern of Cu-B4C-Xtals, with focus on the low 2θ values and the lower temperatures to illustrate the change in structure from the original sample to the dehydrated one.

3.1.2 X-ray Photoelectron Spectroscopy

Since the XPS spectra are collected from a sample under ultra high vacuum conditions, it is likely that some of the water molecules in the voids of Cu-B4C-Xtals have been removed prior to the collection of any XPS spectra. This complicates the data interpretation, since the sample is likely in the dehydrated phase, whose structure is unknown.

The wide scan XPS spectrum, shown in figure 22, indicates the presence of carbon, oxygen and copper, as expected. An etching run was performed to remove small layers of the surface and probe the sample below. In all

cases, etching lasted 5 seconds, whereafter another set of wide scan data was collected. Of interest is the decrease in intensity of the O 1s peak after the first etch. This may be understood by the fact that Cu-B4C-Xtals is synthesised in a sodium metasilicate gel and XPS is a surface probe. It is thus likely that there is a thin layer of sodium metasilicate on the surface which was removed during the first etch, thus resulting in a lowering of intensity. This is further supported by the increase in intensity of the Cu 2p peaks after the first etch. Also of interest is the variation in peak shape of the Cu 2p peak which suggests non uniformity of the Cu sites as one etches further into the sample. It was not possible to identify a sodium peak, which is expected in the region of 1070.8 eV*.

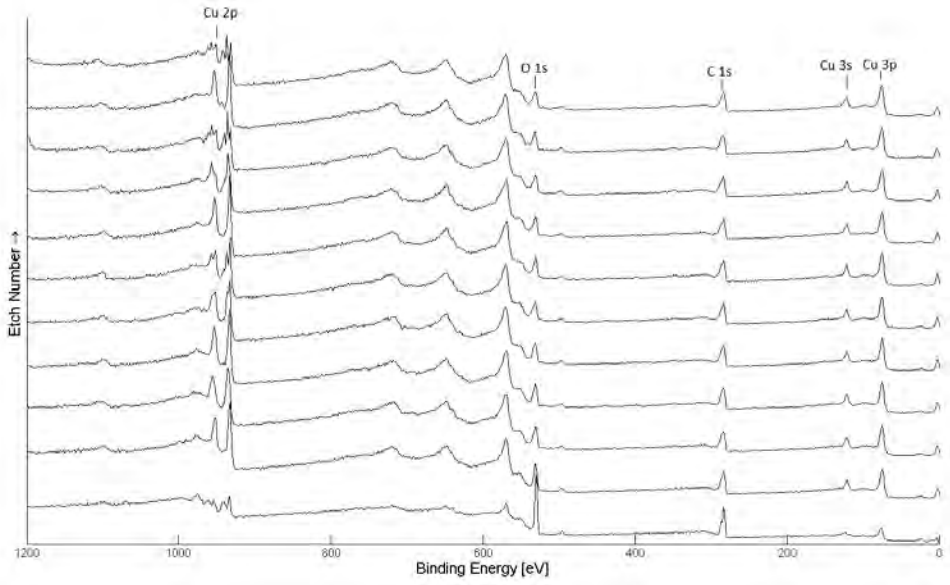

Figure 22: Wide scan XPS spectrum of Cu-B4C-Xtals after every 5 second etch cycle.

High resolution scans of the C 1s, O 1s and Cu 2p regions were collected after the final etch and are shown in figure 23. In all cases, theoretical Gaussian-Lorentzian curves were fitted to the collected data. The C 1s region

*All elemental binding energies in this chapter and chapter 3.2.4 are taking from the same source.[143]

in figure 23a is best described by two peaks. They are centred at 282.6 eV and 286.0 eV. It is also possible to describe the smaller peak as two separate peaks centred at 284.2 eV and 286.5 eV. These may be attributed to aromatic carbons (282.6 eV) and carboxylate carbons (286.0 eV). These are all shifted from the binding energy of elemental carbon, which has a binding energy of 284.2 eV. HKUST-1, a copper(II)-1,3,5-benzenetetracarboxylate MOF has also been characterized by XPS.[44] In this case, binding energies of 284.6 and 288.5 were attributed to aromatic carbons and carboxylate carbons respectively.

The O 1s region of the spectrum is also best described by two peaks, in this case centred at 529.9 eV and 531.7 eV respectively. The appearance of the different peaks may be attributed to carboxylate oxygens, as well as hydroxide and water oxygens. As with the C 1s peaks, the values are shifted from elemental oxygen, which is centred at a binding energy of 543.1 eV.

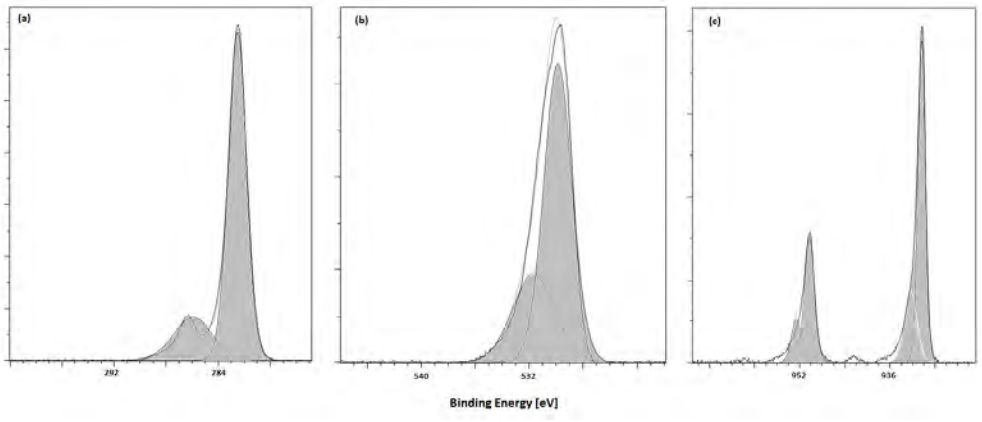

Figure 23: XPS spectra of Cu-B4C-Xtals showing the (a) C 1s, (b) O 1s and (c) Cu 2p regions.

The copper 2p peaks are best described by two peaks, centred at 930.4 eV and 932.4 eV for the $2p_{\frac{3}{2}}$ state and at 950.3 eV and 952.6 eV for the $2p_{\frac{1}{2}}$ state. The binding energy of elemental copper is centred at 932.7 eV and 952.3 eV for the $2p_{\frac{3}{2}}$ and $2p_{\frac{1}{2}}$ states repectively. This binding energy is very similar to that attributed to copper(I) in both copper(I) oxide[144] and in a mixed copper(I)-copper(II) MOF.[145] However, this binding energy has also

been reported as the binding energy for copper(II) in HKUST-1.[44] There is therefore no reason to suspect that the MOF contains any copper ions in the monovalent state.

3.2 Cu-B4C-Needles ($Cu_{2\frac{1}{4}}(OH)_{\frac{1}{2}}B4C{\cdot}8H_2O$)

3.2.1 Elemental Analysis

The work in this section (section 3.2.1) is not original work, but is instead taking from the original source,[118] and rediscussed here for completeness' sake.

Table 4 gives the weight percentages of each of the elements present in different samples of Cu-B4C-Needles, as well as the predicted values based on a variety of possible formulas. The experimental values are clearly denoted by an "Exp" tag. In all cases, the sum of the square of the residuals (SSR) was calculated to use as a measure of the best choice of empirical formula, with a lower SSR indicating a better fit of the calculated values to those obtained experimentally. The sodium content was at most 0.6 wt% in all cases and was attributed to trace amounts of sodium metasilicate gel on the surface of the crystals, rather than sodium incorporated within the MOF. As such, sodium values were omitted from table 4. Chloride, sulfate, nitrate and various silicates were excluded from the possible formulas, since X-ray Fluorescence measurements suggested only trace amounts were present, likely as surface contamination.

When considering the weight percent of each element, it is important to note that the metal:ligand ratio (Cu:B4C) is significantly greater than 2:1 in all cases. This suggests that Cu-B4C-Needles is not simply Cu-B4C-Xtals without the sodium, but is instead more complicated in structure, containing additional copper within the framework. The SSR values are lowest for the case when Cu:B4C is either 2.25:1 or 2.33:1, suggesting a quarter or third of a copper(II) ion extra per formula unit. The value of 2.25:1, corresponding to a formula for Cu-B4C-Needles of $Cu_{2\frac{1}{4}}(OH)_{\frac{1}{2}}B4C{\cdot}8H_2O$, was selected as the best fit, since this reconciles best with the thermal data in chapter 3.2.2. Additionally, it is simple to visualise this structure as being identical to

that of Cu-B4C-Xtals, with a copper(II) ion at every 4th sodium site, with the remaining sodium sites vacant. The hydroxide is present for balance of charge. It is likely that this additional copper(II) is disordered throughout the MOF, which might explain the difficulties in obtaining a structure from single crystal experiments.

Table 4: Elemental analysis results for various Cu-B4C-Needles samples synthesised from the chloride, sulfate and nitrate copper(II) precursors.

Formula	**% C**	**% H**	**% Cu**	**Cu:B4C**	**SSR**
Cu-B4C-Needles-Cl (Exp)	21.99	3.16	26.66	2.29:1	-
$Cu_2B4C{\cdot}7H_2O$	23.86	3.20	25.25	2.00:1	5.49
$Cu_{2\frac{1}{4}}(OH)_{\frac{1}{2}}B4C{\cdot}7\frac{1}{2}H_2O$	22.38	3.29	26.64	2.25:1	0.17
$Cu_{2\frac{1}{3}}(OH)_{\frac{2}{3}}B4C{\cdot}8H_2O$	21.68	3.40	26.77	2.33:1	0.16
$Cu_{2\frac{1}{2}}(OH)B4C{\cdot}8\frac{1}{2}H_2O$	20.74	3.48	27.43	2.50:1	2.27
Cu-B4C-Needles-SO_4 (Exp)	21.99	3.21	26.18	2.25:1	-
$Cu_2B4C{\cdot}7\frac{1}{2}H_2O$	23.44	3.34	24.81	2.00:1	4.01
$Cu_{2\frac{1}{4}}(OH)_{\frac{1}{2}}B4C{\cdot}8H_2O$	22.01	3.42	26.20	2.25:1	0.04
$Cu_{2\frac{1}{3}}(OH)_{\frac{2}{3}}B4C{\cdot}8H_2O$	21.68	3.40	26.77	2.33:1	0.48
$Cu_{2\frac{1}{2}}(OH)B4C{\cdot}8\frac{1}{2}H_2O$	20.74	3.48	27.43	2.50:1	3.21
Cu-B4C-Needles-NO_3 (Exp)	21.82	3.25	26.95	2.33:1	-
$Cu_2B4C{\cdot}7H_2O$	23.86	3.20	25.25	2.00:1	7.05
$Cu_{2\frac{1}{4}}(OH)_{\frac{1}{2}}B4C{\cdot}7\frac{1}{2}H_2O$	22.38	3.29	26.64	2.33	0.41
$Cu_{2\frac{1}{3}}(OH)_{\frac{2}{3}}B4C{\cdot}8H_2O$	21.68	3.40	26.77	2.33:1	0.07
$Cu_{2\frac{1}{2}}(OH)B4C{\cdot}8H_2O$	21.07	3.36	27.87	2.50:1	1.42

3.2.2 Thermal Analysis

Thermal gravimetric analysis (TGA) results, shown in figure 24, indicate that Cu-B4C-Needles loses water molecules in three overlapping steps. Mass loss (i) corresponds to 1.49 ± 0.13 wt% and is complete at 65°C. It is followed immediately by mass loss (ii), occuring between 65°C and 115°C, which has a final mass loss of 18.31 ± 0.21 wt%. This may be understood as the initial loss of 0.5 water molecules (calculated loss: 1.65 wt%) followed by the immediate loss of a further five water molecules (calculated loss: 16.51 wt%) to give a total loss of 5.5 water molecules by 115°C (calculated loss: 18.16 wt%) during steps (i) and (ii).

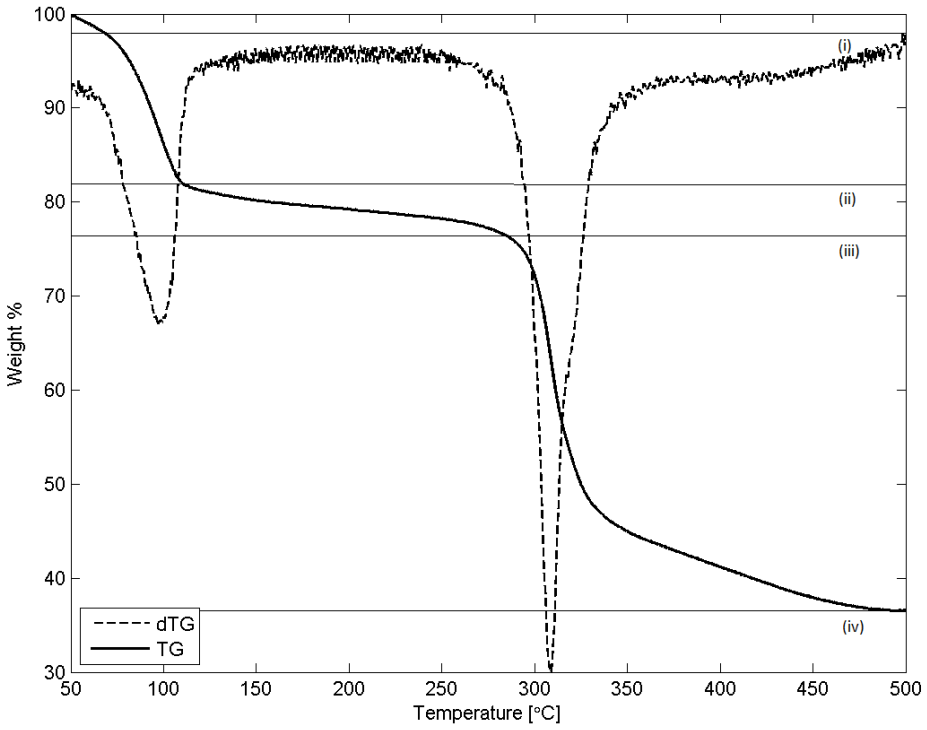

Figure 24: TGA and the associated derivative curve of Cu-B4C-Needles heated at 10°C.min^{-1} under a nitrogen purge (flow rate 25 ml.min^{-1}).

Stage (iii), which occurs between temperatures 115°C and 290°C, ends with a total mass loss of 23.90 ± 0.53 wt%. This corresponds to the loss of a further 2 water molecules from Cu-B4C-Needles (calculated loss: 6.60 wt% to give a total mass loss of 24.76 wt%). The final mass loss step (iv) involves the loss of the remaining 0.5 water molecules as well as the decomposition of the MOF into its decomposition products (metallic copper and carbon), to give a final mass of 38.22 ± 0.55 wt%.

Differential scanning calorimetry (DSC) (the thermogram is given in figure 25), reveals 2 endotherms, A and B, corresponding to mass losses (i) and (ii) observed via TGA. The enthalpy change associated with each of these processes is 3.47 ± 0.23 $J.g^{-1}$ and 379 ± 23 $J.g^{-1}$ of parent material. This is lower than the enthalpy change associated with Cu-B4C-Xtals, which is 420.5 $J.g^{-1}$ of parent material. This does suggest that the water molecules in Cu-B4C-Needles are more weakly bound to the framework on average than in Cu-B4C-Xtals. Since water is coordinated to the sodium site of Cu-B4C-Xtals, this lower energy is to be expected as a result of the absence of such a sodium site in Cu-B4C-Needles.

It is possible to get an idea of the average energy required to remove each of the water molecules within the framework. For endotherm A, the enthalpy change of 3.47 ± 0.23 $J.g^{-1}$ corresponds to 1.89 ± 0.12 $J.mol^{-1}$ of the parent material. Since this process involves the loss of half a water molecule, or 0.5 moles of water per mole of parent, this would correspond to an energy of 3.79 ± 0.25 $kJ.mol^{-1}$ required to remove the initial water molecules. Similarly, for endotherm B which corresponds to the loss of five water molecules, the energy required to remove a water molecule is 41.3 ± 2.6 $kJ.mol^{-1}$. This value is significantly higher, but not surprising, since one would expect the waters that are liberated at higher temperatures to be more strongly bound to the framework, thus requiring more energy to remove. The associated energy in Cu-B4C-Xtals is 38 $kJ.mol^{-1}$, which is not significantly different to that obtained for Cu-B4C-Needles. Attempts were made to identify additional peaks in endotherm B (by decreasing the heating rate as low as 1°$C.min^{-1}$), which was expected to reveal more information on the energies required to remove the separate water molecules. This proved unsuccesful, with the only

result being a shift of endotherm B to a lower temperature.

The decomposition process, which is not shown in figure 25, is largely exothermic. However, it contains many small endotherms and exotherms which are poorly resolved, indicating a complex decomposition process.

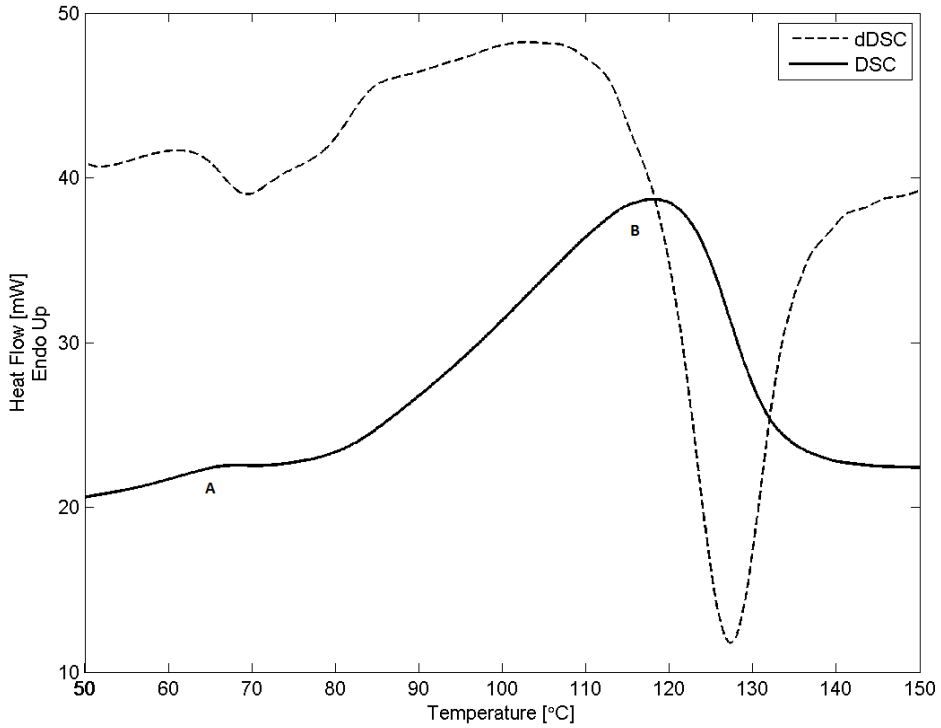

Figure 25: DSC and the associated derivative curve of Cu-B4C-Needles heated at 10°C.min^{-1} under a nitrogen purge (flow rate 20 ml.min^{-1}).

3.2.3 X-ray Powder Diffraction

Figure 26 presents the XRPD patterns of both Cu-B4C-Needles and Cu-B4C-Xtals. The structural similarity between the 2 MOFs is easily seen, especially by noting the reflections outlined by box A, which are indicative of the unit cell being similar in both MOFs. This is supported by single crystal data which suggests the unit cell is almost identical in both the MOFs. However, there are noticeable differences throughout the remainder of the pattern, which suggests subtle differences in the assymetric unit of the structure (single crystal evidence suggests both systems are monoclinic with a $P\bar{1}$ symmetry). Table 15 presents the crystal data of both Cu-B4C-Xtals and Cu-B4C-Needles for comparison. It may be found with images of both structures* in Appendix A.

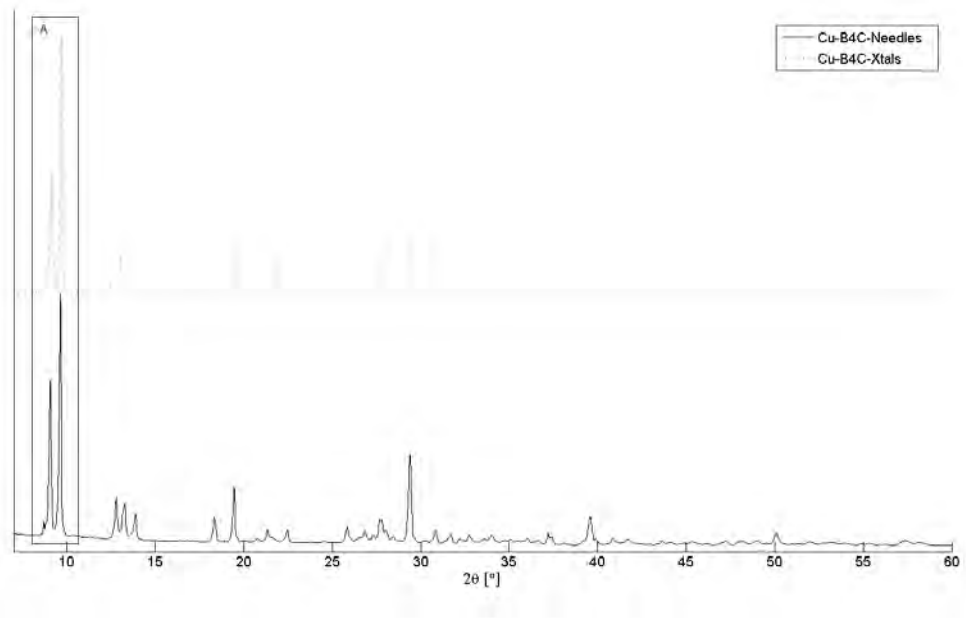

Figure 26: XRPD pattern of both Cu-B4C-Needles and Cu-B4C-Xtals using a cobalt source, illustrating the similarity in structure between these 2 MOFs.

As with Cu-B4C-Xtals, the *in situ* data for Cu-B4C-Needles may be di-

*The structure for Cu-B4C-Needles is not considered solved, but is instead the best refinement that has been obtained to date.

vided into 3 distinct regions. This is illustrated in figure 27. Region I, which was collected at a temperature of 30°C, is the XRPD pattern of the original Cu-B4C-Needles, with all water molecules in the voids. On heating to 90°C, there is an immediate change in phase to that represented in region II. Since TGA evidence suggests the loss of water prior to this temperature, this phase may be ascribed to that of the dehydrated framework, however the structure is once again unknown. The disappearance of the (100), (010) and (001) reflections in the original sample, and the appearance of reflections around 10° and 12° 2θ, is indicative of a decrease in unit cell volume. The change is illustrated more clearly in figure 28. As with Cu-B4C-Xtals, there is significant peak broadening, suggesting a decrease in crystallite size upon dehydration. Region (III) has been confirmed through powder pattern fitting, with TOPAS software, to be metallic copper, in agreement with the decomposition products suggested by TGA data.

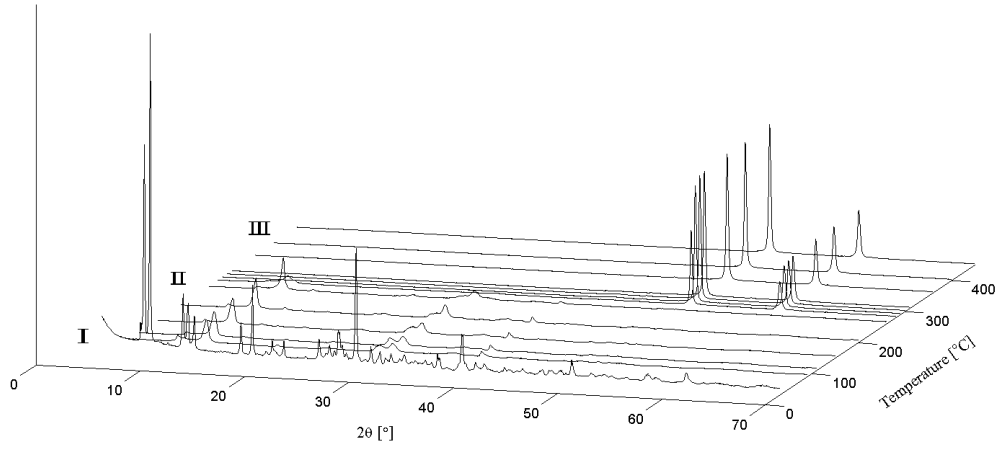

Figure 27: *In situ* XRPD pattern of Cu-B4C-Needles under helium. The data shows 3 separate regions, corresponding to the original structure, the dehydrated structure and the decomposition products.

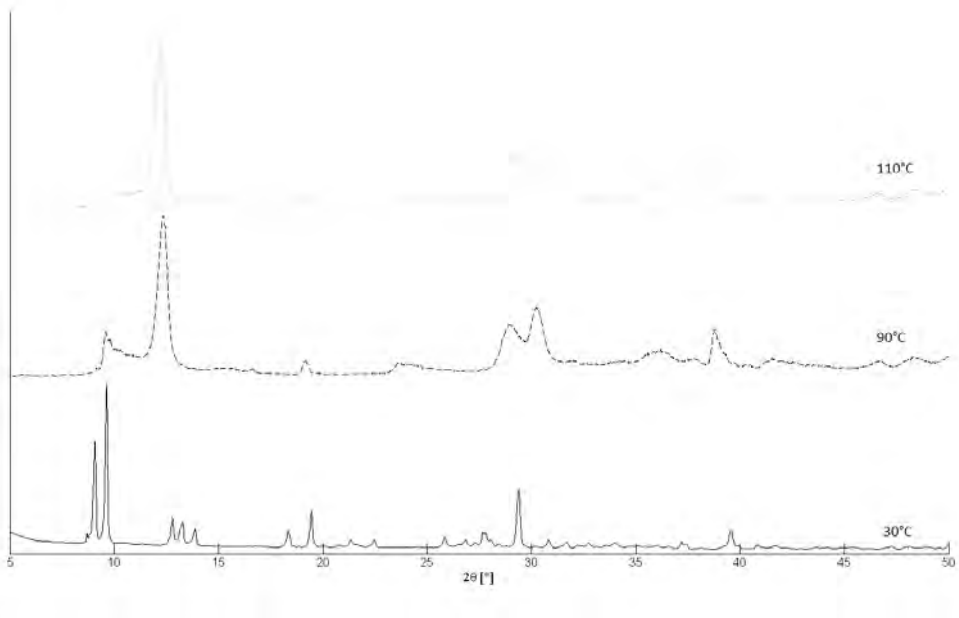

Figure 28: *In situ* XRPD pattern of Cu-B4C-Needles, with focus on the low 2θ values and the lower temperatures to illustrate the change in structure from the original sample to the dehydrated one.

3.2.4 X-ray Photoelectron Spectroscopy

Since the XPS spectra were collected from a sample under ultra high vacuum conditions, as with Cu-B4C-Xtals, it is likely that some of the water molecules in the voids of Cu-B4C-Needles have been removed even before XPS spectra are collected. This complicates the data interpretation, since the sample is likely in the dehydrated phase, whose structure is unknown.

The wide scan XPS spectrum, shown in figure 29, shows the presence of carbon, oxygen and copper, as expected. An etching run was performed to remove small layers of the surface and probe the sample below. In all cases, etching lasted 5 seconds, whereafter another set of wide scan data was collected. Of interest is the decrease in intensity of the O 1s peak after the first etch. As with Cu-B4C-Xtals, Cu-B4C-Needles is synthesised in a sodium metasilicate gel and XPS is a surface probe. It is thus likely that there is a thin layer of sodium metasilicate on the surface which was removed during

the first etch, thus resulting in a lower intensity. This is further supported by the increase in intensity of the Cu 2p peaks after the first etch. Unlike Cu-B4C-Xtals, Cu-B4C-Needles shows no changes in the Cu 2p region as was evident with Cu-B4C-Xtals.

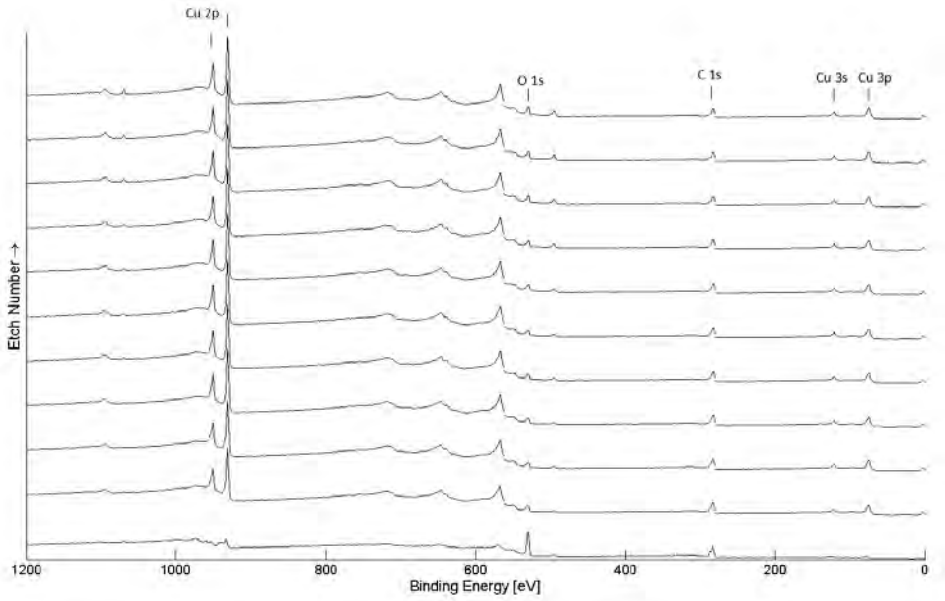

Figure 29: Wide scan XPS spectrum of Cu-B4C-Needles every 5 s after etching.

High resolution scans of the C 1s, O 1s and Cu 2p regions were collected after the final etch and are shown in figure 30. In all cases, theoretical Gaussian-Lorentzian curves were fitted to the collected data. The C 1s region in figure 30a is best described by two peaks. They are centred at 282.4 eV and 285.3 eV. These values are esentially the same as those obtained for Cu-B4C-Xtals and are attributed to aromatic carbons and carboxylate carbons respectively. This is once again similar to the values obtained for HKUST-1.[44] All the binding energies are shifted from the binding energy of elemental carbon, which has a binding energy of 284.2 eV.[143]

The O 1s, figure 30b, is also best described by two peaks, in this case centred at 529.4 eV and 531.9 eV respectively. Once more, the values are shifted from elemental oxygen, which is centred at a binding energy of 543.1 eV and are attributed to carboxylate oxygen as well as hydroxide and water

oxygen.

The copper 2p peaks, figure 30c, are each described by two fitted peaks, centred at 930.6 eV and 931.8 eV for the $2p_{\frac{3}{2}}$ state and at 950.5 eV and 952.7 eV for the $2p_{\frac{1}{2}}$ state. The binding energy of elemental copper is centred at 932.7 eV and 952.3 eV for the $2p_{\frac{3}{2}}$ and $2p_{\frac{1}{2}}$ states repectively.

It was hoped that the high resolution scan of the copper 2p region would indicate a third copper peak, originating from the disordered copper that is not present in Cu-B4C-Xtals. This is not the case and it is assumed that the binding energy of this disordered copper atom is not sufficiently different to be able to resolve it from the other copper peaks. The fact that not just the copper, but also the carbon and oxygen binding energies for Cu-B4C-Needles are so similar to those of Cu-B4C-Xtals only strengthens the hypothesis that they are isostructural, with only the substitution of sodium by copper as the difference between the 2 MOFs.

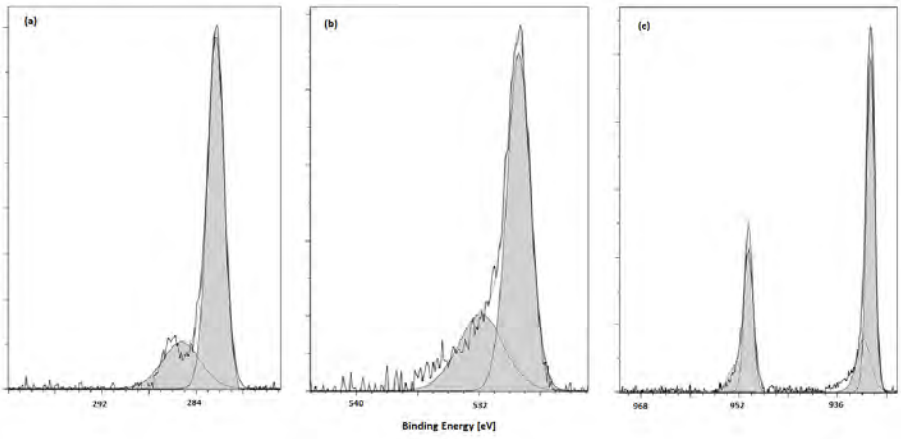

Figure 30: XPS spectra of Cu-B4C-Xtals showing the (a) C 1s, (b) O 1s and (c) Cu 2p regions.

3.3 Hydrothermal Syntheses

3.3.1 Elemental Analysis

The experimentally obtained values for each of the hydrothermally synthesised products are given in table 5. In each case, the ratio of copper to sodium is calculated, as well as the ratio of copper to B4C ligand. The expected values for these are 2:1 in both cases should the synthesised product be Cu-B4C-Xtals, or 0 and 2.25:1/2.33:1 should the synthesised product be Cu-B4C-Needles. It can be seen from the table that the resultant product seldom is within error of these expected values, but rather falls between some average value of this, suggesting that a mixture of products has formed in most cases.

In order to confirm the presence of a mixture of products, some SEM images were taken. Figure 31 and figure 32 are micrographs of Cu-B4C-Na-acet-pH5 and Cu-B4C-Nat-acet-pH6 respectively. Cu-B4C-Na-acet-pH5 demonstrates small bundles of very fine crystallites, as well as much longer, needle-like crystallites. Cu-B4C-Na-acet-pH6 contains similar small bundles of fine crystallites in addition to much larger, flat plate-like crystals. These lend support to the idea that the samples are a mixture of products.

Table 5: Elemental analyses for all the hydrothermally synthesised samples. Numbers in brackets are the uncertainties in the last given decimal place.

Sample	**% C**	**% H**	**% Cu**	**% Na**	**Cu:Na**	**Cu:B4C**
Cu-B4C-Na-acet-pH4	21.61(1)	3.33(3)	27.0(3)	2.70(3)	3.62:1	2.37:1
Cu-B4C-Na-acet-pH5	21.43(1)	3.45(3)	26.2(3)	3.12(1)	3.04:1	2.31:1
Cu-B4C-Na-acet-pH6	20.74(6)	2.7(2)	26.9(3)	3.40(5)	2.86:1	2.45:1
Cu-B4C-Na-acet-pH6.5	18.09(1)	2.77(7)	31.4(6)	3.09(3)	3.68:1	3.28:1
Cu-B4C-Na-acet-12h	22.1(1)	3.1(4)	22.4(2)	3.88(3)	2.08:1	1.91:1
Cu-B4C-Na-acet-48h	22.0(1)	2.9(3)	23.2(3)	4.15(4)	2.02:1	1.99:1
Cu-B4C-Na-acet-72h	22.11(8)	2.93(5)	22.9(3)	4.34(4)	2.34:1	2.08:1
Cu-B4C-Na-acet-cool	22.18(8)	3.2(2)	24.5(3)	3.79(3)	2.33:1	2.08:1
Cu-B4C-Na-acet-short	21.70(8)	3.15(1)	23.4(3)	3.48(4)	2.42:1	2.04:1
Cu-B4C-Na-acet-glass	22.1(2)	3.2(2)	22.7(3)	4.39(4)	1.87:1	1.94:1

The pH-varied samples Cu-B4C-Na-acet-X (where X = pH4, pH5, pH6 or pH6.5), all demonstrate a copper content that is higher than expected. The syntheses performed at pH 6.5 and pH 6 both demonstrate low hydrogen and carbon contents compared to what is expected for Cu-B4C-Xtals (22.1 wt% and 3.15 wt% respectively and Cu-B4C-Needles (22.0 wt% and 3.42 wt% respectively). This is especially apparent in Cu-B4C-Na-acet-pH6.5. The sodium content suggests the formation of some Cu-B4C-Xtals.

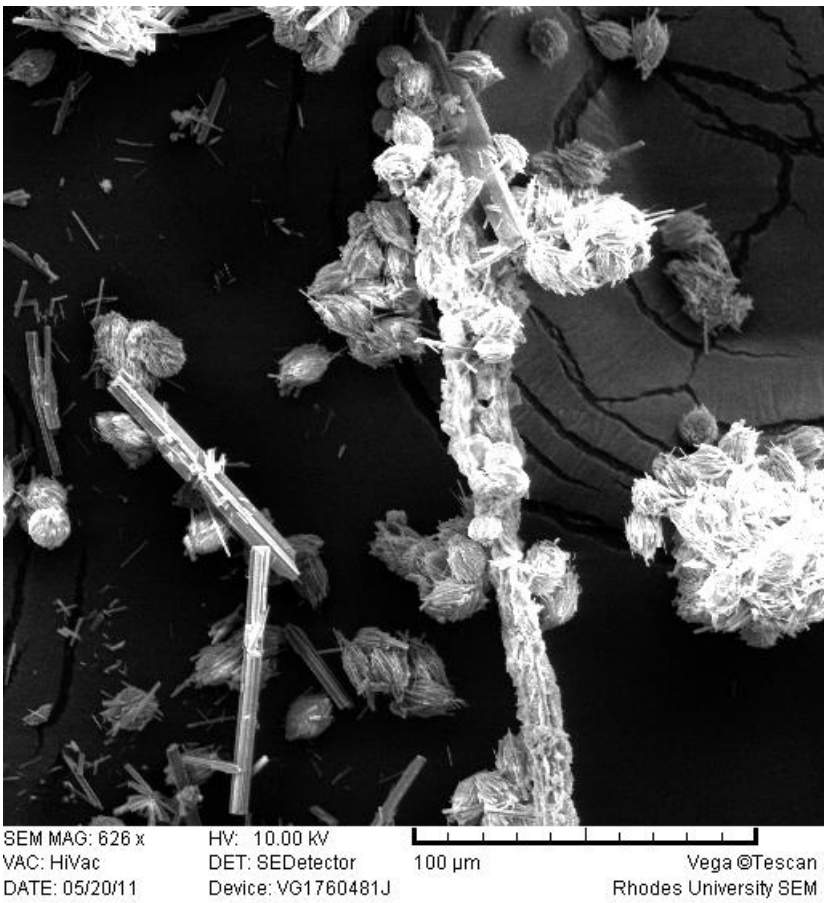

Figure 31: SEM micrograph of Cu-B4C-Na-hydro-pH5, indicating both small bundles of crystallites and long, needle-like crystallites.

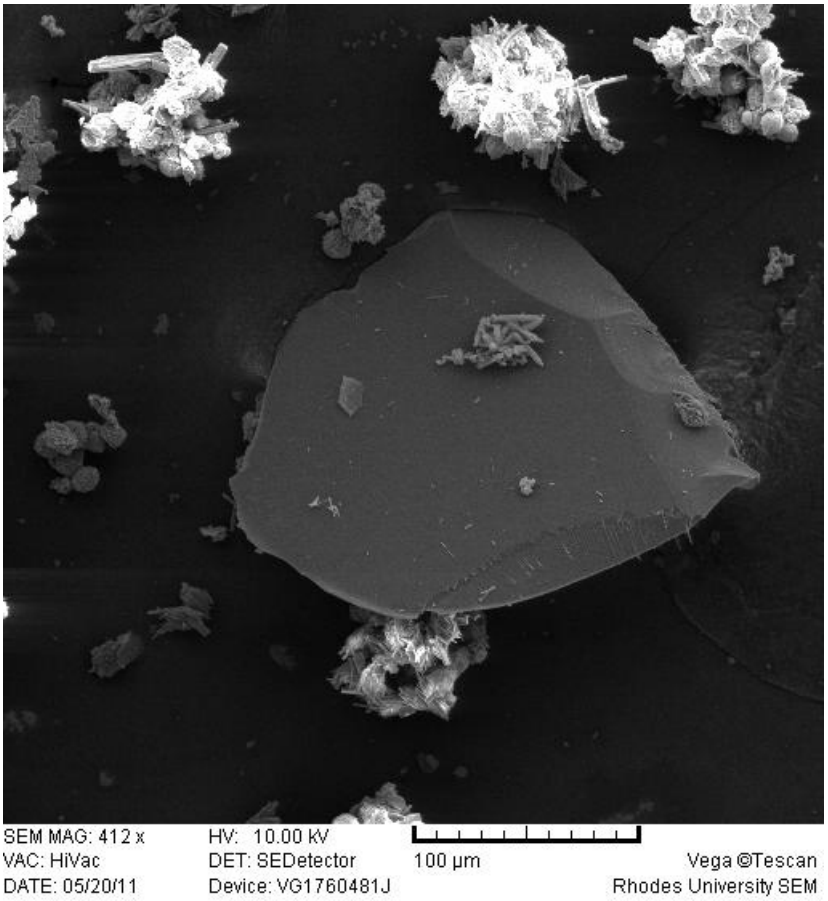

Figure 32: SEM micrograph of Cu-B4C-Na-hydro-pH6, indicating both small bundles of crystallites and large, flat plate-like crystallites.

This is confirmed by XRPD, the data presented in chapter 3.3.2. It is also likely, based on the high Cu:B4C ratios, that there is a certain amount of Cu-B4C-Needles present. In all cases, deposits of what appeared to be copper(II) oxide or copper(II) hydroxide were observed on the TEFLON® insert, suggesting the presence of some copper(II) oxide or copper(II) hydroxide in the sample itself. The data were fed into a spreadsheet and the relative percentages of these compounds calculated. The previously synthesised hydrothermal compound $Cu_2B4C{\cdot}0.65H_2O$ was also included. This information is shown in table 6. The sum of the squares of the residuals is used as a measure of the fit in each case.

In all cases, the major product formed is Cu-B4C-Xtals, with Cu-B4C-Needles occuring as the secondary product. Cu-B4C-Na-acet-pH6.5 shows a significantly higher percentage of copper(II) oxide and copper(II) hydroxide. This is consistent with its difference in colour. Interestingly, none of the samples demonstrate a large amount of $Cu_2B4C{\cdot}0.65H_2O$, which was obtained in 100% yield when no sodium was used, or when there was no pH correction. Since the samples synthesised at pH 5.0 and pH 6.0 were so similar, either of these pH values could have been used in the temperature-varied syntheses. However, the synthesis of Cu-B4C-Na-acet-pH6 still resulted in some copper(II) oxide/hydroxide residue on the TEFLON® insert. As such, pH 5 was chosen to use in the temperature varied syntheses.

It should be noted that there are many variables in these calculations, such as the number of possible products to consider. As such, the elemental data is in itself not conclusive, but is tied together with the XRPD data in chapter 3.3.2 and thermal analysis data in chapter 3.3.3 to form a more complete picture.

Table 6: Calculated relative amounts of various compounds in the hydrothermally synthesised samples.

Sample	**% Xtals***	**% Needles***	**% $Cu_2B4C{\cdot}0.65H_2O$**	**% $Cu(OH)_2$**	**% CuO**	**SSR**
Cu-B4C-Na-acet-pH4	60	38	0	1	1	$5.09x10^{-3}$
Cu-B4C-Na-acet-pH5	74	19	2	5	0	$5.56x10^{-3}$
Cu-B4C-Na-acet-pH6	80	14	0	3	3	$3.71x10^{-3}$
Cu-B4C-Na-acet-pH6.5	74	8	0	13	5	$3.72x10^{-3}$

*Xtals and Needles are used as concise forms for Cu-B4C-Xtals and Cu-B4C-Needles to minimise column width

Table 7: Calculated relative amounts of various compounds in the hydrothermally synthesised samples.

Sample	**% Cu-B4C-Xtals**	**% Cu-B4C-Needles**	**SSR**
Cu-B4C-Na-acet-12h	91	9	$4.95x10^{-3}$
Cu-B4C-Na-acet-48h	98	2	$4.70x10^{-3}$
Cu-B4C-Na-acet-72h	100	0	$4.82x10^{-3}$
Cu-B4C-Na-acet-short	81	19	$4.83x10^{-3}$
Cu-B4C-Na-acet-cool	85	15	$5.18x10^{-3}$
Cu-B4C-Na-acet-glass	100	0	$5.52x10^{-3}$

For the temperature/time-varied samples, the elemental data (table 5) is much closer to that of Cu-B4C-Xtals than in the pH-varied samples. In most cases, the sodium content is a bit lower and the copper content a bit higher than expected for pure Cu-B4C-Xtals. This suggests the presence of Cu-B4C-Needles in the samples as well. The same process of determining the relative amounts of the various compounds was also applied to this set of samples, with the results given in table 7. However, all cases resulted in essentially zero copper(II) hydroxide, copper(II) oxide and $Cu_2B4C{\cdot}0.65H_2O$, thus they were regarded as being zero. As such, they are not presented in the table.

An interesting trend may be noted, one that is perhaps better visualised in figure 33. Figure 33 graphs the calculated percentage formation of Cu-B4C-Xtals for the various samples that were synthesised in the TEFLON® insert. The samples are arranged such that the amount of time they spent in the reactor increases from left to right. Cu-B4C-Na-acet-short was subjected to a simple heating to 120°C, whereafter it was immediately allowed to cool to room temperature. It thus spent the shortest time at an elevated temperature. Compare this to Cu-B4C-Na-acet-72h, which was heated to 120°C, where it was held for 72 hours, before cooling to 100°C for 12 hours, then to 80°C for a further 12 hours, thus spending the longest total time at an elevated temperature. The data suggets that the longer the reagents spend in the reactor, the more the product is shifted towards the formation of Cu-B4C-Xtals.

The elemental data suggests that Cu-B4C-Na-acet-glass, synthesised in a glass vessel as opposed to a TEFLON® insert, is 100% Cu-B4C-Xtals. Cu-B4C-Na-acet-glass was heated to 120°C, where it was held for 48 hours, before cooling to 100°C for 12 hours and then 80°C for a further 12 hours. Thus it was subject to the same temperature programme as that of Cu-B4C-Na-acet-48h. However, the elemental data suggests that Cu-B4C-Na-acet-48h consists of 98% Cu-B4C-Xtals and 2% Cu-B4C-Needles. The errors associated with these calculations are such that this difference is not significant. As a result, it is not possible to conclude whether a glass vessel, as opposed to a TEFLON® one, had any effect on the selective formation of Cu-B4C-Xtals.

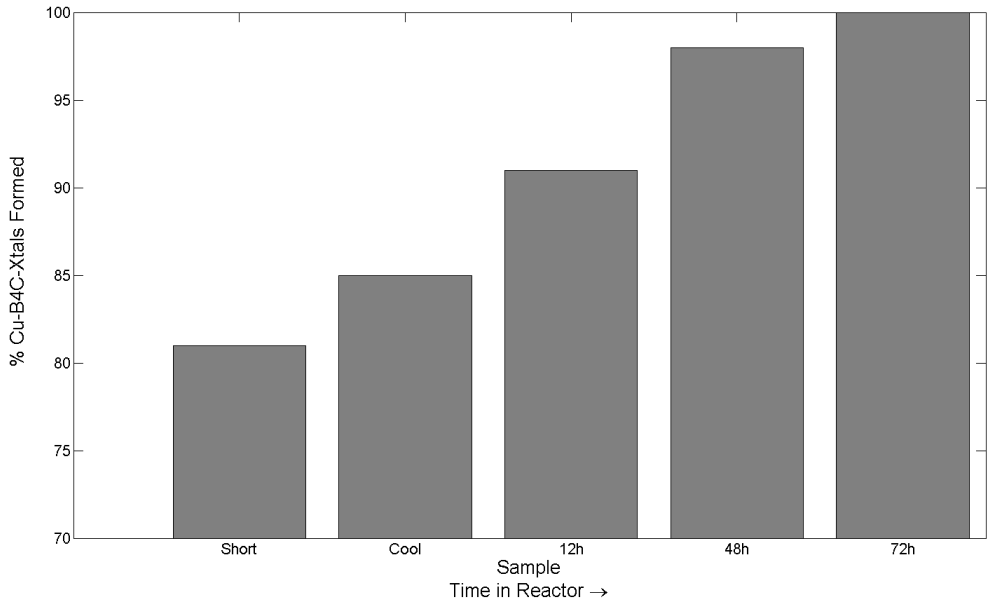

Figure 33: The percentage formation of Cu-B4C-Xtals in each of the temperature/time-varied samples. The other sample formed is Cu-B4C-Needles. There is a trend suggesting an increase in the formation of Cu-B4C-Xtals with an increase in time spent in the reactor.

3.3.2 X-ray Powder Diffraction

The XRPD patterns for each of the hydrothermally synthesised samples are shown in figure 34 and figure 35. The XRPD patterns of Cu-B4C-Xtals and Cu-B4C-Needles are also shown in each of the figures for comparison. In all cases, the samples correspond to Cu-B4C-Xtals, supporting the elemental data which suggests that this is the major compound in each product. This is evidenced by the presence of two peaks at 14.8° and 15.8° 2θ which are present in Cu-B4C-Xtals, but not in Cu-B4C-Needles. Owing to the similarity in structure between these two MOFs, it is difficult to distinguish one from the other in any other part of the diffraction pattern.

Based on simulated powder diffraction patterns (using version 1.14 mercury software[146]) for copper(II) oxide,[147] it is expected that major diffraction peaks will occur at 35.6°, 38.8° and 48.8° 2θ. Similarly for copper(II) hydrox-

ide,[148] major diffraction peaks are expected to occur at 16.7°, 23.8°, 34.1° and 39.8° 2θ. All the hydrothermally synthesised products contain peaks at these values, however it is not possible to determine whether these peaks are resultant from the presence of copper(II) oxide and copper(II) hydroxide, since Cu-B4C-Xtals and Cu-B4C-Needles also have peaks at these values. Quantitative phase analysis, using the Rietveld method,[149] was not attempted owing to the unknown structure of Cu-B4C-Needles.

Finally, it can be observed that peaks are generally broader in the hydrothermally synthesised samples than in either Cu-B4C-Xtals or Cu-B4C-Needles. This suggests that the hydrothermal synthesis conditions (temperature, time, pH *etc.*) result in the formation of smaller crystallites than the gel-synthesis method. Cu-B4C-Na-acet-short, the sample which spent the least amount of time in the reactor, shows significantly broader peaks than any of the other samples. This is understandable since it spent the least amount of time at an elevated temperature in the growth medium.

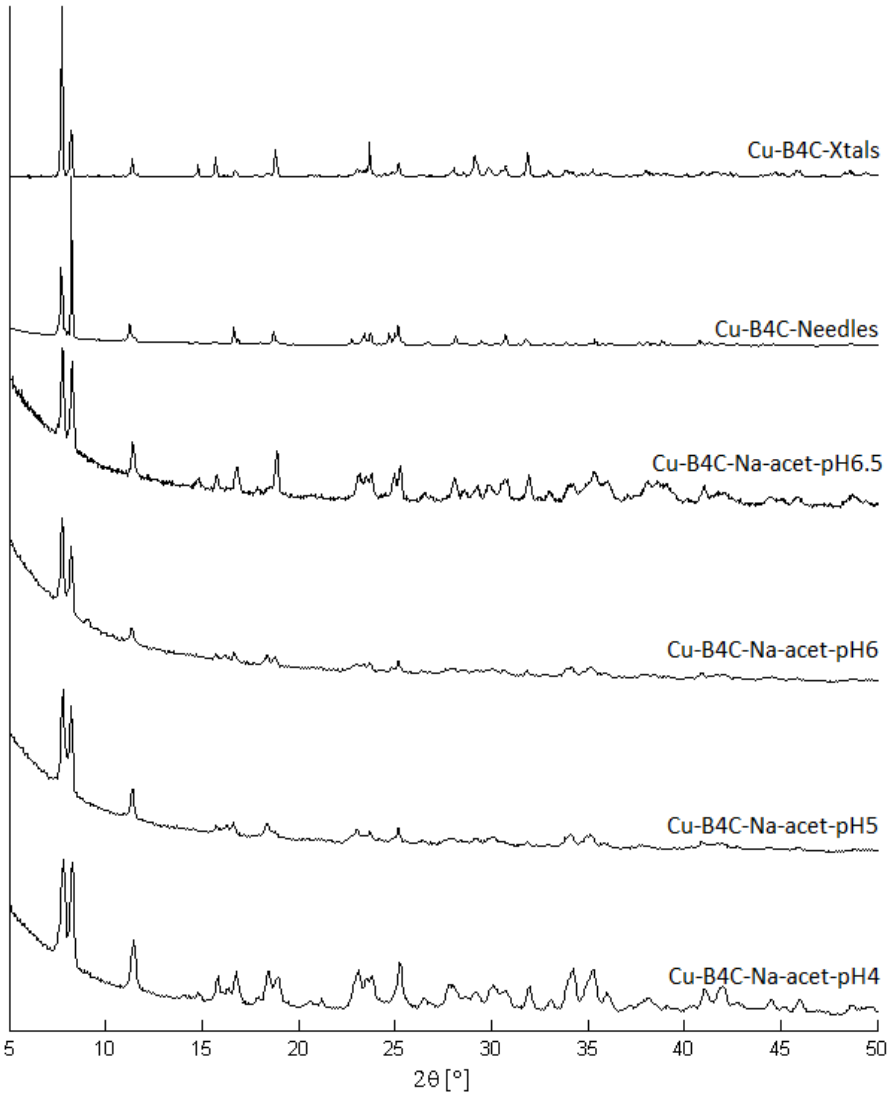

Figure 34: XRPD patterns of Cu-B4C-Na-acet-pH4, Cu-B4C-Na-acet-pH5, Cu-B4C-Na-acet-pH6 and Cu-B4C-Na-acet-pH6.5 using Cu radiation. The XRPD patterns of Cu-B4C-Xtals and Cu-B4C-Needles are added for reference.

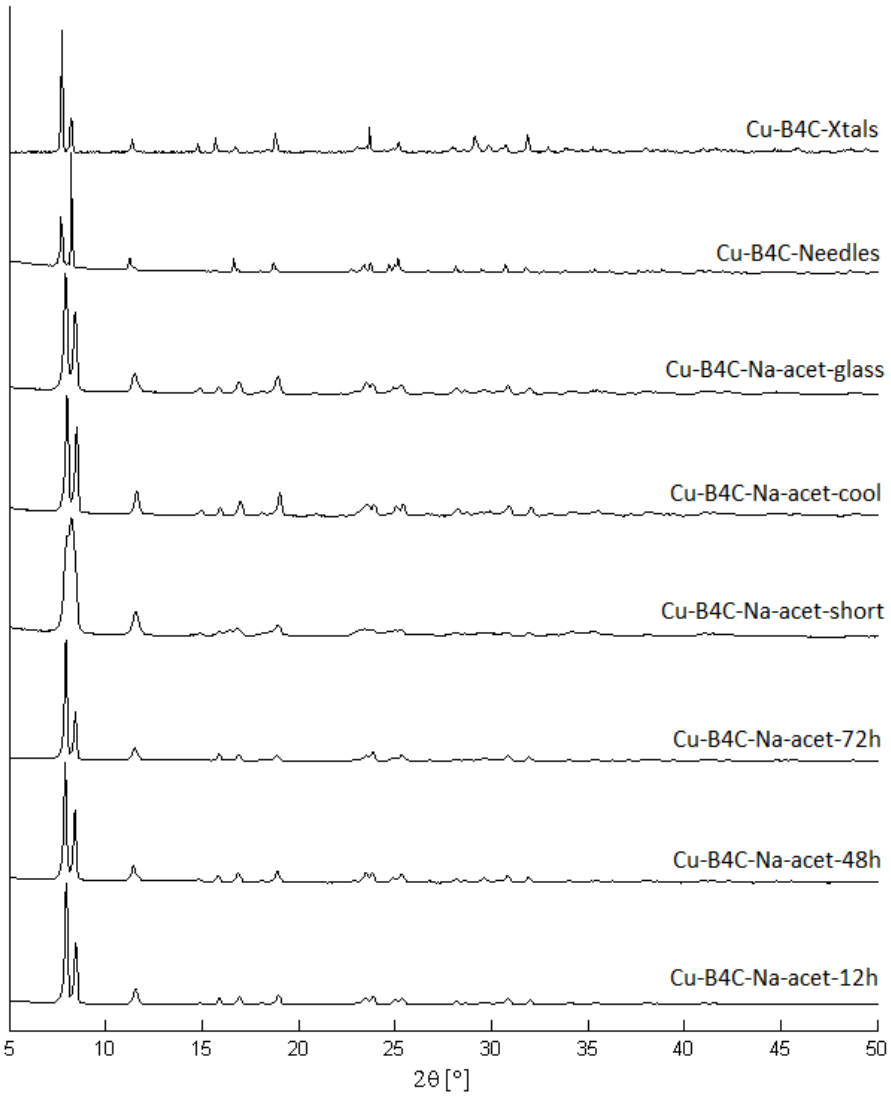

Figure 35: XRPD patterns of Cu-B4C-Na-acet-12h, Cu-B4C-Na-acet-48h, Cu-B4C-Na-acet-72h, Cu-B4C-Na-acet-short, Cu-B4C-Na-acet-cool and Cu-B4C-Na-acet-glass using Cu radiation. The XRPD patterns of Cu-B4C-Xtals and Cu-B4C-Needles are added for reference.

3.3.3 Thermal Analysis

The thermal analysis data for the hydrothermally synthesised samples is in good agreement with the XRPD and elemental data. Figure 36, figure 37 and figure 38 present the TGA thermograms (and their associated derivative curves) for each of the hydrothermally synthesised samples. All samples showed 4 distinct regions of mass loss, except Cu-B4C-Na-acet-pH5, which showed 5. The total percentage mass lost upon completion of each mass loss stage is summarised in table 8.

All the samples exhibit thermal behaviour similar to that of Cu-B4C-Xtals, supporting the elemental data which suggests that Cu-B4C-Xtals forms the bulk of the product. However, there are subtle differences in some cases that suggest the samples are not pure Cu-B4C-Xtals.

In each case an initial mass loss, labelled (i), of approximately 1.5 wt% was observed. This mass loss is always complete by 60°C. This is characteristic of both Cu-B4C-Needles and Cu-B4C-Xtals. As such, it provides no meaningful information regarding the relative amounts of these two MOFs.

Thereafter, there was a second mass loss stage, labelled (ii), that corresponds to the loss of water molecules from the voids of Cu-B4C-Xtals and Cu-B4C-Needles. This stage is complete by approximately 100°C. In all cases, except that of Cu-B4C-Na-acet-pH6.5 shown in figure 36d, the total mass loss at this stage was approximately 19 wt%. Cu-B4C-Xtals has a slightly greater mass loss at this point than Cu-B4C-Needles (see chapter 1.4 and chapter 3.2.2 respectively). As such, it is expected that the sample containing more Cu-B4C-Needles will have a smaller mass loss by the completion of step (ii). Unfortunately, the errors are too large to obtain the relative amounts of Cu-B4C-Xtals and Cu-B4C-Needles from this mass loss step. While Cu-B4C-Na-acet-pH6.5 does demonstrate a significantly smaller mass loss step at this point, this is not as a result of an increased proportion of Cu-B4C-Needles, but may understood by the fact that Cu-B4C-Na-acet-pH6.5 is expected to contain large fractions of copper(II) oxide and copper(II) hydroxide (5% and 13% respectively). In all the other samples, the estimated amount of copper(II) oxide and copper(II) hydroxide is very small, and as

a result does not infuence the TGA thermograms. However, the amount is significant in the case of Cu-B4C-Na-acet-pH6.5 and this is supported by the TGA evidence.

Copper(II) hydroxide decomposition to copper(II) oxide begins at 80°C if the copper(II) hydroxide is wet and at 190°C if it is dry.[150] However, since the mass change associated with this decomposition is only 18.5 wt% and the mass fraction of copper(II) hydroxide is expected to be below 1% in all products with the exception of Cu-B4C-Na-acet-pH6.5 (resulting in an expected mass loss of less than 0.185 wt%), it was not possible to identify this decompostion process in any of the TGA thermograms.

Mass loss stage (iii) corresponds to the slow loss of either one water molecule in the case of Cu-B4C-Xtals, or two water molecules in the case of Cu-B4C-Needles, and occurs between 100°C and 290°C. Cu-B4C-Na-acet-pH4, Cu-B4C-Na-acet-pH5, Cu-B4C-Na-acet-pH6 and Cu-B4C-Na-acet-short all demonstrate larger mass losses during this step than the other samples. The thermograms, shown in figures 36a, 36b, 36c and 38a respectively, all indicate a steeper slope over the course of mass loss (iii) that is characteristic of Cu-B4C-Needles, as opposed to the other samples (Cu-B4C-Na-acet-pH6.5 once again discounted), which have flatter slopes. This supports the elemental data, which suggests that these samples contain higher proportions of Cu-B4C-Needles. Once again, Cu-B4C-Na-acet-pH6.5 demonstrates a lower mass loss, which suggests significant amounts of copper(II) oxide and copper(II) hydroxide.

Cu-B4C-Na-acet-pH5 (figure 36b) demonstrates a two-step mass loss during stage (iii) that is clearly evidenced by the derivative curve. This two-stage loss which is not evident in any of the other samples, is fully reproducible. Elemental analysis suggested that Cu-B4C-Na-acet-pH5 was the only sample to contain $Cu_2B4C{\cdot}0.65H_2O$. However, $Cu_2B4C{\cdot}0.65H_2O$ has been shown[118] to decompose at approximately 350°C, while in this case, the second portion of the mass loss begins at 250°.

It is possible that some interaction with one of the other products was able to lower the decomposition temperature. It is also possible that there is another compound present in the product that has not been accounted

for. However, none of the known copper(II)-B4C MOFs show any significant mass loss in this temperature region (The mass loss would have to be significant to show up, since it is likely that only a few percent of the sample is present in the product). Other unpublished work within the research group* suggests that a mass loss at this temperature corresponds to the loss of acetate groups from the sample. It is thus possible that pH 5 was favourable for the incorporation of acetate groups within the products formed.

The final mass loss step (iv), which occurs from 290°C, corresponds to the decomposition of Cu-B4C-Xtals and Cu-B4C-Needles. This step in Cu-B4C-Xtals and Cu-B4C-Needles is a two-step process, with the two steps overlapping to a very large extent. However, all the hydrothermally synthesised samples exhibit a very distinct two-step mass loss during step (iv). This is likely a result of the difference in crystallite size between the hydrothermally synthesised products, and Cu-B4C-Xtals and Cu-B4C-Needles. The hydrothermally synthesised products consist of much smaller crystallites, as evidenced by XRPD (chapter 3.3.2).

Cu-B4C-Xtals and Cu-B4C-Needles have final masses equal to 40 wt% and 38 wt% of the original sample mass respectively. Cu-B4C-Na-acet-pH6.5 has a final mass equal to 43.5 wt% of the original sample mass. This further supports the conclusion reached from elemental analysis that it contains copper(II) oxide and copper(II) hydroxide. Copper(II) oxide has a molar mass of 79.55 $g.mol^{-1}$, approximately 6.8 times less than that of Cu-B4C-Xtals and Cu-B4C-Needles. A mass discrepency of 3.5% would imply that the original sample contained approximately 2.5% copper(II) oxide by mass. This corresponds to 19% copper(II) oxide and copper(II) hydroxide by number (5% and 14% respectively). This is in good agreement with the values obtained from the elemental data.

Cu-B4C-Na-acet-pH4, Cu-B4C-Na-acet-pH5 and Cu-B4C-Na-acet-short demonstrate lower final masses than the other samples (approximately 37 wt% compared to 40 wt%). This suggests that the samples contain a larger proportion of Cu-B4C-Needles, consistent with the elemental data. However, elemental data did suggest the presence of some copper(II) oxide and cop-

*This information has been obtained via personal communication with Ivan Hodgson.

per(II) hydroxide in the former two samples. This is not consistent with the TGA data, since this would result in a slightly higher final mass than that which was observed. It is therefore likely that there were small proportions of an additional phase present in these products. Cu-B4C-Na-acet-pH6 is also expected to contain a relatively high proportion of Cu-B4C-Needles. It has a final mass of 40 wt%. However, the error in this case is fairly large, and a small amount of copper(II) oxide or copper(II) hydroxide present in the original sample, as suggested by elemental data, would account for the slight increase in final mass. All the other final masses are approximately 40 wt%, consistent with the suggestion that the product consists mainly of Cu-B4C-Xtals.

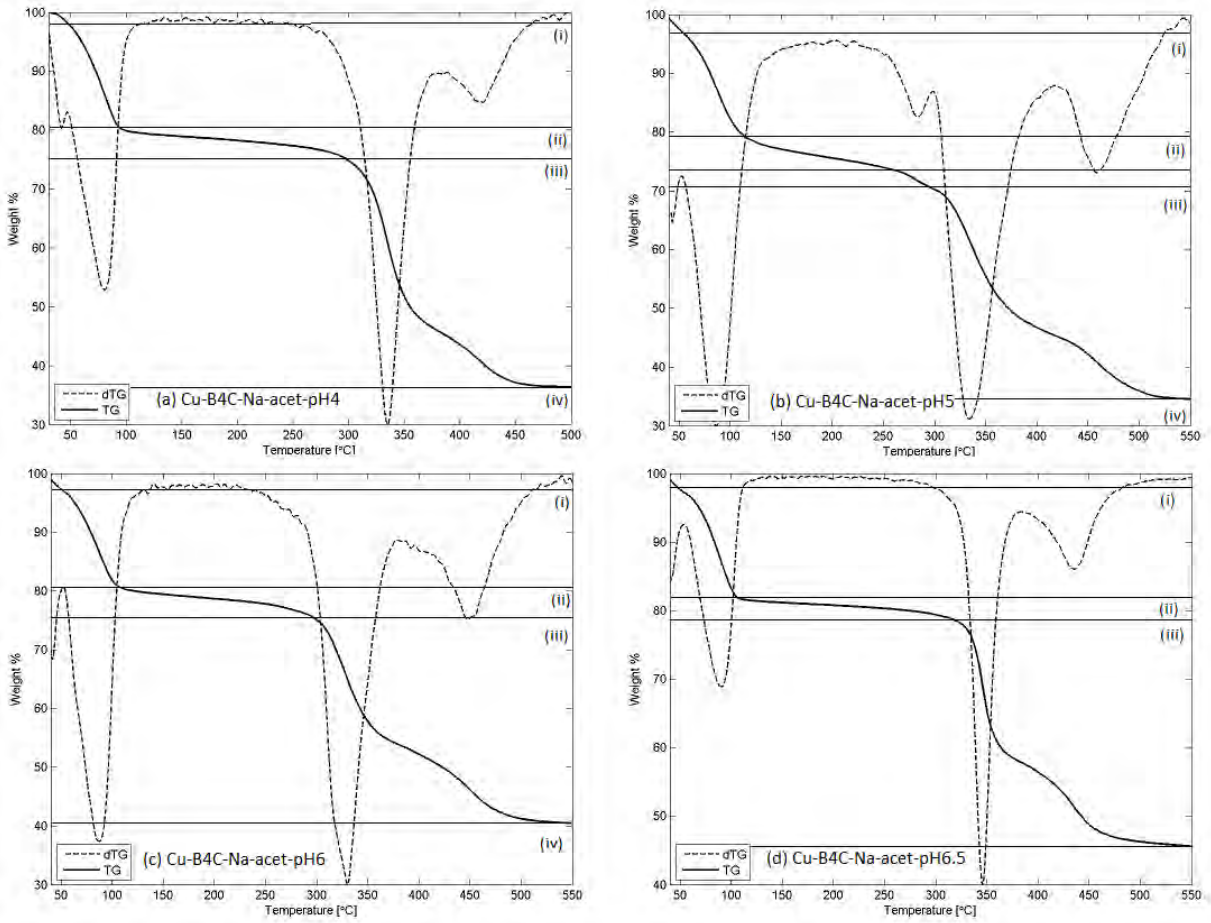

Figure 36: TGA and the associated derivative curve of (a) Cu-B4C-Na-acet-pH4, (b) Cu-B4C-Na-acet-pH5, (c) Cu-B4C-Na-acet-pH6, (d) Cu-B4C-Na-acet-pH6.5, heated at 10°C.min^{-1} under a nitrogen purge (flow rate 25 ml.min^{-1}).

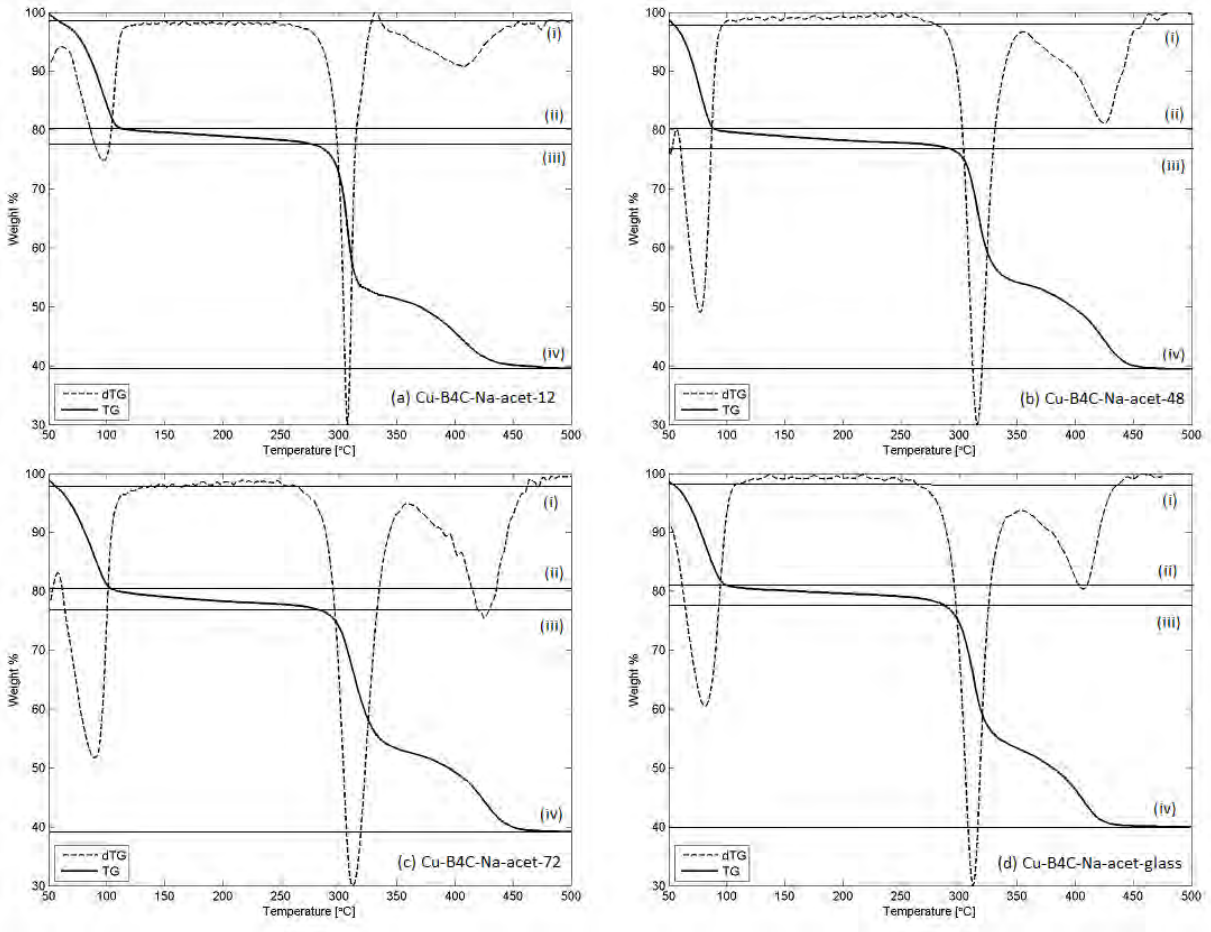

Figure 37: TGA and the associated derivative curve of (a) Cu-B4C-Na-acet-12h, (b) Cu-B4C-Na-acet-48h, (c) Cu-B4C-Na-acet-72h, (d) Cu-B4C-Na-acet-glass, heated at 10°C.min^{-1} under a nitrogen purge (flow rate 25 ml.min^{-1}).

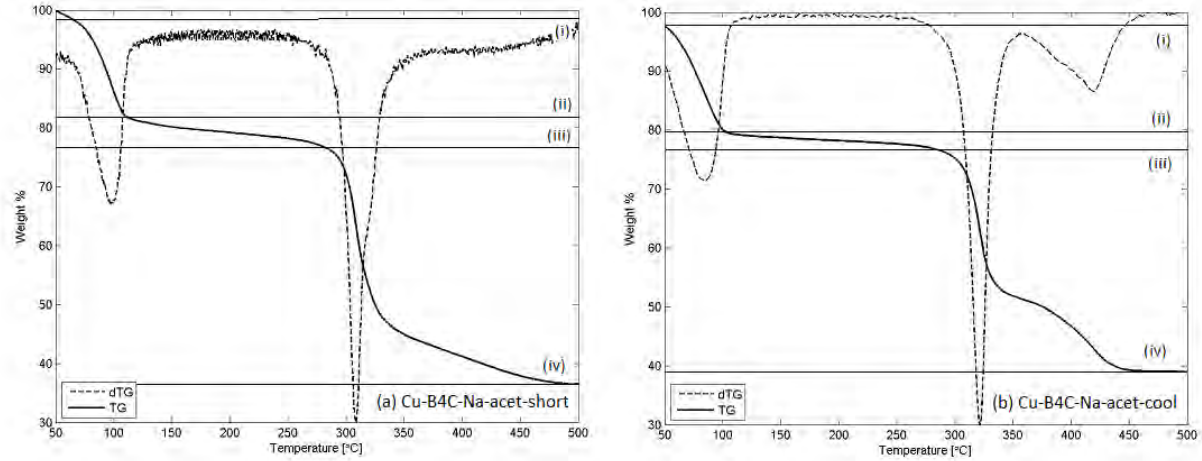

Figure 38: TGA and the associated derivative curve of (a) Cu-B4C-Na-acet-short, (b) Cu-B4C-Na-acet-cool, heated at 10°C.min^{-1} under a nitrogen purge (flow rate 25 ml.min^{-1}).

Table 8: The total mass loss at the end of each TGA mass loss stage, as evidenced by the TGA thermograms given in figure 36, figure 37 and figure 38.

Sample	**Step (i)**	**Step (ii)**	**Step (iii)**	**Step (iv)**
Cu-B4C-Na-acet-pH4	1.2(3)	18.2(9)	23.7(5)	63.0(9)
Cu-B4C-Na-acet-pH5	1.7(1)	20.0(8)	24.7(15)	63.5(9)
Cu-B4C-Na-acet-pH6	1.5(2)	19.9(12)	24.4(19)	60.0(22)
Cu-B4C-Na-acet-pH6.5	1.3(2)	17.3(13)	21.9(10)	56.5(19)
Cu-B4C-Na-acet-12h	1.3(4)	17.9(16)	23.1(7)	60.6(2)
Cu-B4C-Na-acet-48h	1.2(1)	18.9(7)	23.6(12)	60.6(1)
Cu-B4C-Na-acet-72h	1.4(1)	18.9(7)	23.0(13)	60.3(6)
Cu-B4C-Na-acet-short	1.0(1)	17.7(3)	23.7(5)	63.3(9)
Cu-B4C-Na-acet-cool	1.5(1)	19.6(5)	22.9(15)	60.5(7)
Cu-B4C-Na-acet-glass	1.1(2)	19.6(5)	22.9(15)	60.5(7)

The DSC thermograms, shown in figure 40, figure 41 and figure 42, all exhibit the same shape as each other and Cu-B4C-Xtals, supporting the evidence which suggests that the major product in each of the syntheses is indeed Cu-B4C-Xtals. All thermograms exhibited an endotherm between approximately 60°C and 120°C. The enthalpy change associated with each these endotherms per gram of the original sample is given in table 9.

Table 9: The enthalpy changes associated with the water-loss in each of the DSC endotherms of the hydrothermally synthesised products. The DSC thermograms are shown in figure 40, figure 41 and figure 42.

Sample	ΔH [J.g^{-1}]
Cu-B4C-Na-acet-pH4	218(10)
Cu-B4C-Na-acet-pH5	159(11)
Cu-B4C-Na-acet-pH6	223(22)
Cu-B4C-Na-acet-pH6.5	231(12)
Cu-B4C-Na-acet-12h	266(13)
Cu-B4C-Na-acet-48h	299(3)
Cu-B4C-Na-acet-72h	258(19)
Cu-B4C-Na-acet-short	244(80)
Cu-B4C-Na-acet-cool	156(27)
Cu-B4C-Na-acet-glass	231(15)

In all cases, the values were lower than for either Cu-B4C-Xtals or Cu-B4C-Needles. However, it is believed that the crystallite sizes in these samples, being much less than those of either Cu-B4C-Xtals or Cu-B4C-Needles, had the effect of lowering the energies for the hydrothermally synthesised samples, since majority of the void waters were closer to the surface, so any factor, such as a capillary force, would have had a much reduced effect and thus required less energy to remove.

Cu-B4C-Na-acet-pH5 and Cu-B4C-Na-acet-cool demonstrate comparably lower enthalpies when compared to the other samples. Since Cu-B4C-

Na-acet-cool exhibited much smaller crystallite sizes than the other samples (chapter 3.3.2), this lower energy may be interpreted as even more of the pore waters being closer to the surface than in the other samples and thus requires less energy to remove.

Cu-B4C-Na-acet-pH5, on the other hand, exhibited a mass loss characteristic of acetate loss. It is possible that the presence of these acetates lowers the energy required to remove the water molecules by blocking their access to the pores, resulting in more waters closer to the surface. In fact, a closer inspection of the derivative curve (marked by a black box in figure 40b) of the DSC thermogram of Cu-B4C-Na-acet-pH5 suggests a small endotherm between 130°C and 140°C, which is a similar temperature to the mass loss associated with the loss of acetate.

For all samples, exotherms corresponding to the decomposition of the framework were very poorly resolved. The exotherm for Cu-B4C-Na-acet-12h is shown in figure 39 as an example, with all other exotherms following a similar pattern. This is in keeping with the TGA data, which shows that the decomposition process in the hydrothermally synthesised samples occurs over a much broader temperature range.

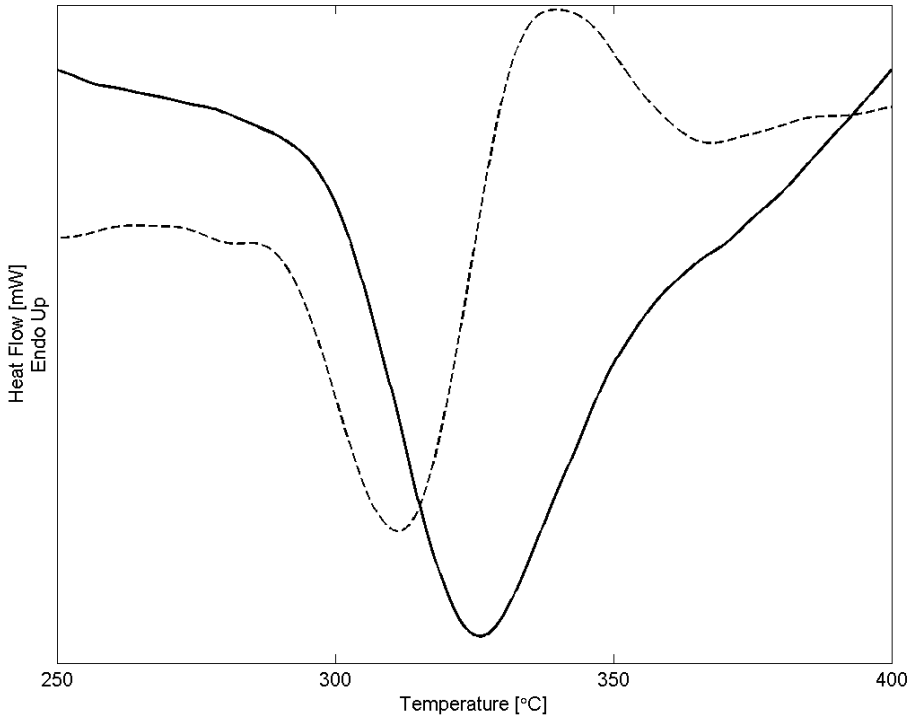

Figure 39: DSC and the associated derivative curve of the decomposition of Cu-B4C-Na-acet-12h, heated at 10°C.min^{-1} under a nitrogen purge (flow rate 20 ml.min^{-1}).

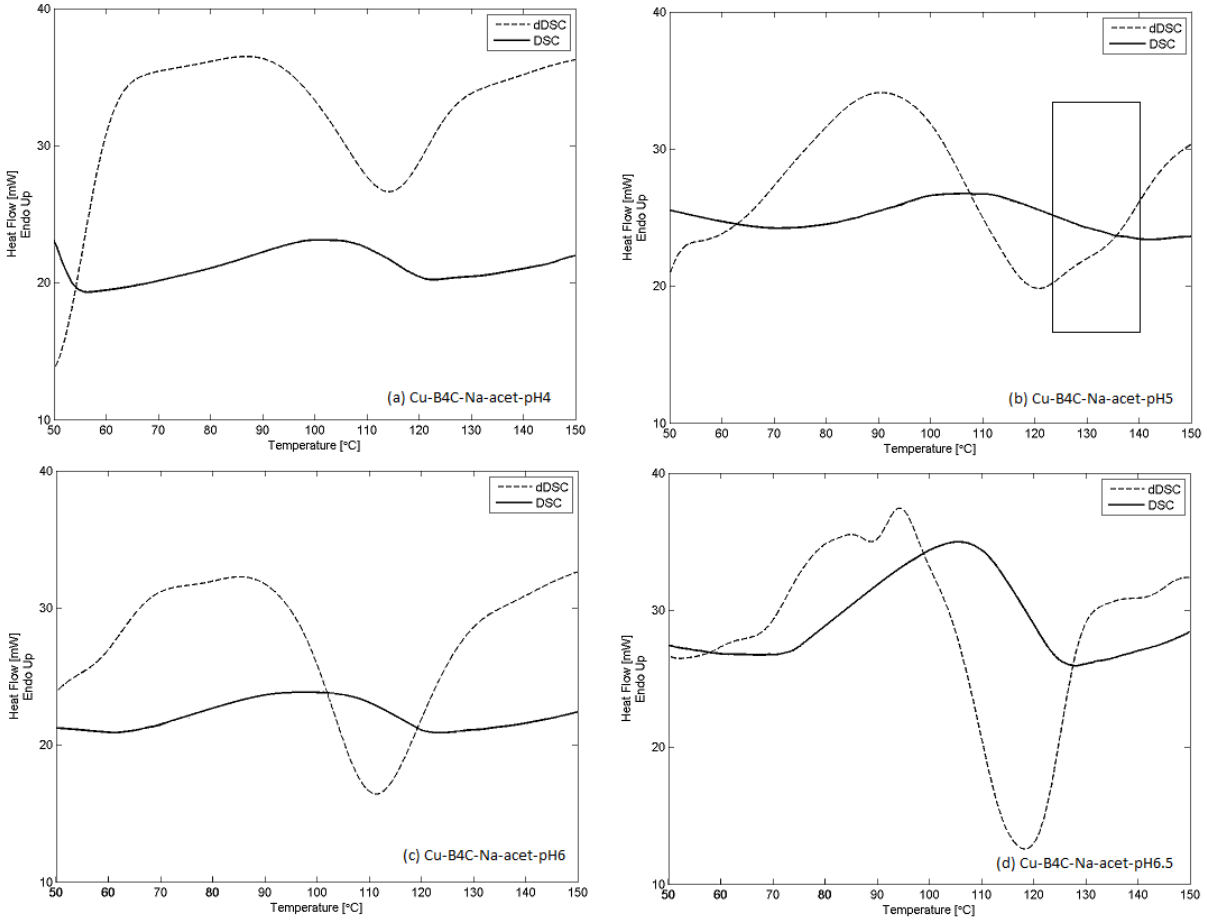

Figure 40: DSC and the associated derivative curve of (a) Cu-B4C-Na-acet-pH4, (b) Cu-B4C-Na-acet-pH5, (c) Cu-B4C-Na-acet-pH6, (d) Cu-B4C-Na-acet-pH6.5, heated at 10°C.min^{-1} under a nitrogen purge (flow rate 20 ml.min^{-1}).

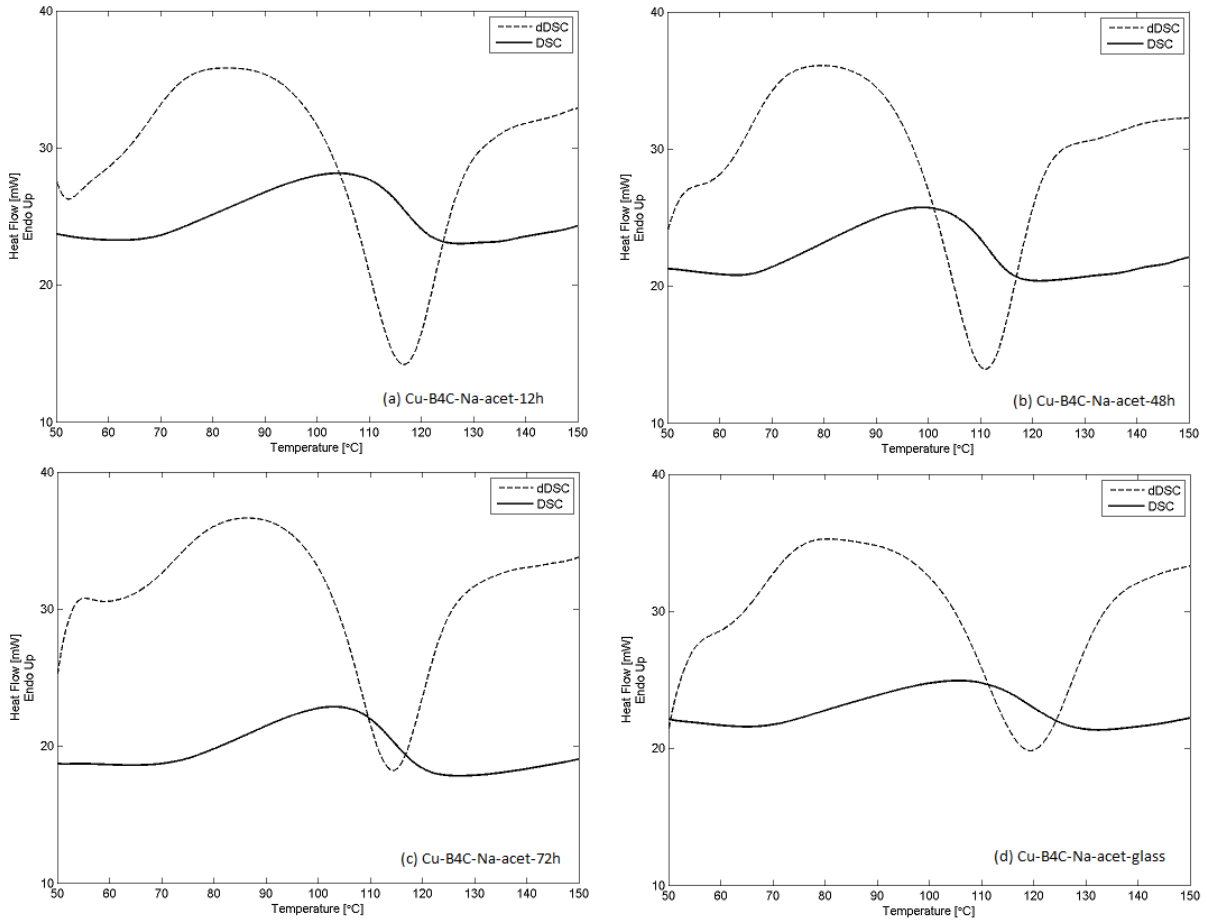

Figure 41: DSC and the associated derivative curve of (a) Cu-B4C-Na-acet-12h, (b) Cu-B4C-Na-acet-48h, (c) Cu-B4C-Na-acet-72h, (d) Cu-B4C-Na-acet-glass, heated at 10°C.min^{-1} under a nitrogen purge (flow rate 20 ml.min^{-1}).

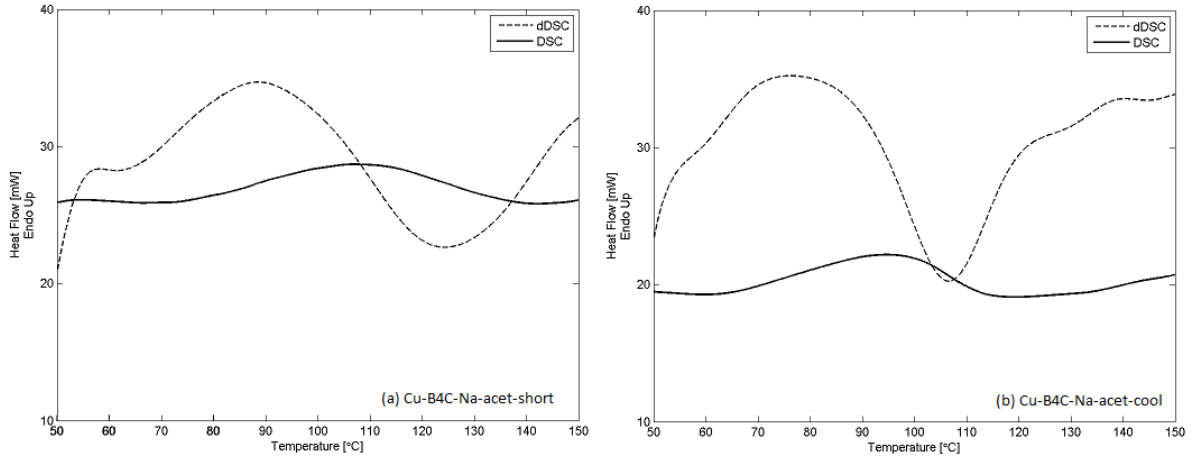

Figure 42: DSC and the associated derivative curve of (a) Cu-B4C-Na-acet-short, (b) Cu-B4C-Na-acet-cool, heated at 10°C.min^{-1} under a nitrogen purge (flow rate 20 ml.min^{-1}).

3.3.4 Conclusions

Based on the elemental analyses, XRPD and thermal analysis data, it is possible to conclude that Cu-B4C-Xtals was synthesised via a hydrothermal method.

The most important factor in this is ensuring that pH correction of the B4C solution, to a pH of 5.0, occurs *before* it comes into contact with the copper(II) acetate solution. This ensures that the major product is indeed Cu-B4C-Xtals.

Since sodium hydroxide was used in pH correction and sodium acetate added to provided sufficient quantity of sodium ions, this opens up the possibility to synthesise MOFs analagous to Cu-B4C-Xtals, with the sodium substituted by potassium or lithium for example. This would require the use of the appropriate hydroxide and acetate (in the examples given, this would become lithium or potassium hydroxide for pH correction and lithium or potassium acetate to provide sufficient cations of interest).

The second most important factor is time spent at an elevated temperature and pressure. Approximately 48 hours at 120°C is needed to ensure almost 100% formation of Cu-B4C-Xtals. Too short and the resulting product is a mixture of Cu-B4C-Xtals and Cu-B4C-Needles, while the crystallites are extremely small.

It seems unlikely that this method will be able to produce Cu-B4C-Needles in a major yield, since the cation present in whichever base is chosen for pH correction is likely to sit at the sodium site. Should Cu-B4C-Needles be desired, an alternative method needs to be investigated, such as ultrasound or microwave-assisted synthesis.

4 Desolvation/Resolvation Studies

The desolvation/resolvation method has already been outlined in section 2.3. The guest molecules chosen for this study consist of water, methanol, ethanol, formaldehyde, acetaldehyde, formamide, N,N'-dimethylformamide, acetonitrile, DMSO, carbon disulfide and pyridine. These solvents were chosen since they offer variety in terms of donor groups, molecular size, polarity and their ability to form hydrogen bonds.

The desolvation/resolvation studies fall into 2 categories. The first involves a single-step desolvation/resolvation, wherby a sample of the original is simply dehydrated and exposed to the guest molecule vapours of interest prior to characterisation. All the potential guest molecules are subject to single-step desolvation/resolvation studies. Those guest molecules that demonstrate appreciable uptake are then investigated in a multi-step dehydration/rehydration study. This involves continual removal of the guest, followed by re-exposure to the guest molecule vapours (the same or a different guest) in order to study the reusability of Cu-B4C-Needles. In all cases, the studies were performed in triplicate (sample size, N, of 3), unless specifically stated. All samples are denoted by Cu-B4C-needles-GUEST, where GUEST is any of the guest molecules mentioned above.

All initial desolvations involved a mass loss of 21.11 $\pm$ 0.53 wt%*. This corresponds to 6.40 $\pm$ 0.16 of the 8 water molecules per formula unit of Cu-B4C-Needles lost during this dehydration process. This leaves a dehydrated structure having the formula $Cu_{2\frac{1}{4}}(OH)_{\frac{1}{2}}B4C{\cdot}1\frac{1}{2}H_2O$. Table 10 shows the percentage mass gain of each of the dehydrated samples *after* exposure to the guest molecule vapours. Of these potential guests that were studied, water showed appreciable uptake, while methanol showed a very slight uptake. Even though some of the samples showed appreciable mass gain on exposure to the guest, this was not attributed to the guest of interest, and each of these is discussed in the relevant section.

*$N = 66$

Table 10: The percentage mass increase of dehydrated Cu-B4C-Needles after exposure to the guest molecule vapours and the associated number of guest molecules taken up. In some cases, it is likely that water was taken up from a wet solvent.

Guest	**% Mass Gained**	**No. Guest Molecules**
Water	19.02 ± 0.35	4.5
Methanol	4.61 ± 0.43	0.6
Ethanol	0.95 ± 0.77	0.1
Formaldehyde	18.25 ± 0.31	2.5 or 4.3 water
Acetaldehyde	10.24 ± 0.99	1.0
Pyridine	0.79 ± 0.63	0.0
Acetonitrile	0.08 ± 0.79	0.0
N,N'-dimethylformamide	0.82 ± 0.11	0.05
DMSO	2.67 ± 0.73	0.1
Formamide	2.10 ± 0.10	0.2
Carbondisulfide	18.72 ± 0.26	1 or 4.4 water

Additionally, the vapour prssures of each of the chosen guest molecules is given in table 11. By comparing it with the mass uptake given in table 10, one can deduce that the uptake (or lack of uptake) of the various guest molecules is not a pressure influenced phenomenon.

Table 11: Vapour pressures of the various guest molecules at 25°C.

Guest	**Vapour Pressure [torr]**
Water[151]	23.8
Methanol[152]	127.9
Ethanol[152]	59
Formaldehyde[153]	3882
Acetaldehyde[151]	923
Pyridine[151]	18.7
Acetonitrile[151]	88.3
N,N'-dimethylformamide[151]	3.7
DMSO[151]	0.42 (at 20°C)
Formamide[151]	0.08 (at 20°C)
Carbondisulfide[152]	355.22

4.1 Water

Cu-B4C-Needles-Water demonstrated a mass gain of 19.02 ± 0.35 wt%. Assuming that all this mass gain is in the form of water molecules, this would equate to an uptake of 4.5 water molecules per formula unit, to give a rehydrated structure having an empirical formula of $Cu_{2\frac{1}{4}}(OH)_{\frac{1}{2}}B4C{\cdot}6H_2O$.

The XRPD pattern of Cu-B4C-Needles-water is shown in figure 43 together with that of Cu-B4C-Needles and Cu-B4C-Needles-Dehydrated. The XRPD pattern of the dehydrated sample was obtained using the same diffractometer as all the other patterns. As such, it was exposed to the atmosphere, which resulted in the uptake of some water molecules. However, the rehydration was only partial, as evidenced by peaks corresponding to both Cu-B4C-Needles as well as the dehydrated structure that was characterised using *in situ* XRPD (chapter 3.2.3).

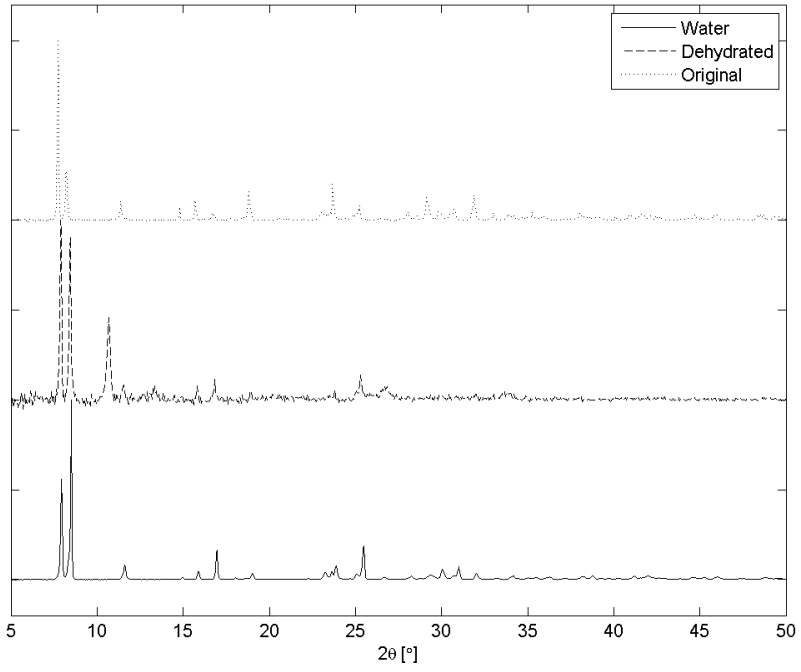

Figure 43: XRPD pattern of Cu-B4C-Needles-Water demonstrating a return to the original structure on exposure to water.

The absence of peaks corresponding to the dehydrated structure suggests that all of the sample has taken up guest molecules. In addition, the similarity between the XRPD pattern of Cu-B4C-Needles-Water and Cu-B4C-Needles suggests that the structure of Cu-B4C-Needles-Water is essentially the same as that of the original framework.

The IR spectrum in figure 44 confirms the restoration of the original structure in Cu-B4C-Needles-Water. As with the XRPD, the IR spectra of Cu-B4C-Needles and Cu-B4C-Needles-Dehydrated are shown for comparison. Cu-B4C-Needles-Dehydrated suffers the same issue of partial rehydration, however it does contain unique bands that may be used in determining a structural change.

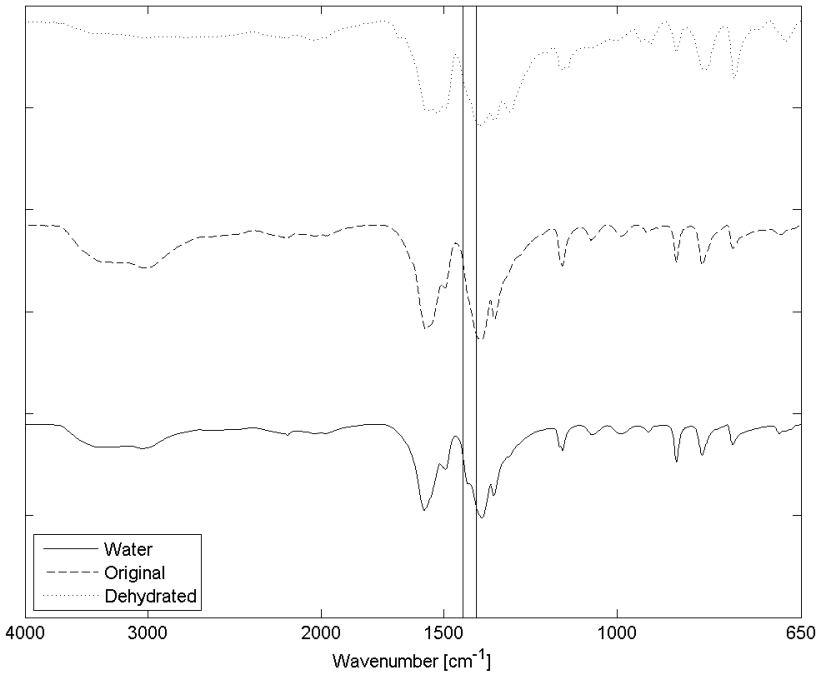

Figure 44: IR spectrum of Cu-B4C-Needles-Water indicating a subtle change in the coordination environment of the carboxylate groups.

All bands of Cu-B4C-Needles-Water correspond to those of Cu-B4C-Needles, with the exception of the band at 1416 cm^{-1}. This band is in

the region associated with a carboxylate stretch. It is also not present in Cu-B4C-Needles-Dehydrated. This suggests that during the uptake of water, there is a subtle change in the coordination of one of the carboxylate groups on B4C to the copper(II) centres.

The TGA data, shown in figure 45, supports this evidence. It exhibits a four-step mass loss, as the original sample does. An initial mass loss of 1.3 ± 0.2 wt% occurs between 50°C and 65°C during mass loss step (i). This may be interpreted as the loss of half a water molecule (calculated loss: 1.7 wt%). Mass loss (ii) follows immediately and results in a total mass loss of 14.6 ± 0.9 wt% by 105°C. This corresponds to the total loss of four water molecules (calculated loss: 14.1 wt%) during steps (i) and (ii). Mass loss (iii) occurs between 105°C and 280°C. This step results in a mass loss of 5.8 wt%, bringing the total mass loss upon completion of mass loss (iii) to 20.4 ± 1.4 wt%. This corresponds to the loss of 1.5 water molecules (calculated loss: 19.4 wt%)during step (iii). The final step (iv) comprises the loss of the remaining 0.5 water molecules, as well as decomposition of the framework, to give a residual mass of 38.6 ± 1.6 wt%. This residual mass is higher than that of the original Cu-B4C-Needles, which supports the fact that less water molecules were taken up by the dehydrated framework. This is contrasted by Cu-B4C-Xtals, which takes up all the water molecules that are removed during dehydration.

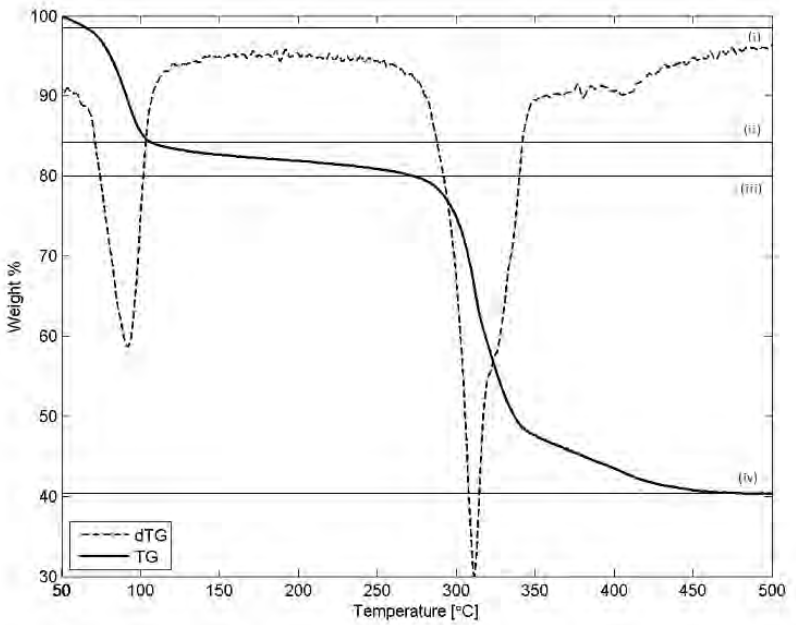

Figure 45: TGA and the associated derivative curve of Cu-B4C-Needles-Water heated at 10°C.min^{-1} under a nitrogen purge (flow rate 25 ml.min^{-1}).

DSC data is given in figure 46. It demonstrates an endothermic process occuring over the temperature range of 60°C to 110°C. The presence of a small endotherm prior to the main endotherm, as was observed for Cu-B4C-Needles, is not observed for Cu-B4C-Needles-Water. The temperature range of this endotherm corresponds to the removal of the water molecules during mass loss stages (i) and (ii). The enthalpy change associated with this process is 262.7 $\pm$ 9.5 J.g^{-1} of parent material. This is considerably lower than 379 $\pm$ 23 J.g^{-1}, the enthalpy change associated with the same endotherm in Cu-B4C-Needles. However, it must be remembered that four water molecules are lost during this process, as opposed to five. The average energy to remove each of the water molecules is 33.5 $\pm$ 1.2 kJ.mol^{-1}. This value is significantly lower to that obtained for Cu-B4C-Needles (41.3 $\pm$ 2.6 kJ.mol^{-1}).

The decomposition process is similar to that of Cu-B4C-Needles, and is mainly an exothermic process containing several endothermic processes.

The IR evidence, which suggests a subtle change in the coordination

environment of a carboxylate group, might explain these data. It is suspected that during dehydration, one of the carboxylate groups undergoes a subtle rotation or repositioning that is not fully reversible on rehydration. As a result of this, the amount of water taken up is less than originally lost, since this rotation results in a loss of hydrogen bonding in the hydrogen bond network that is responsible for holding the water molecules in the voids. A second consequence of this is that the water molecules are less tightly bound to the framework, requiring less energy to remove, as evidenced by the DSC data.

Comparing this system to Cu-B4C-Xtals, it is possible that the presence of the sodium cation prevents this subtle change to the carboxylate group and as a result Cu-B4C-Xtals is capable of fully reversible water-uptake behaviour.

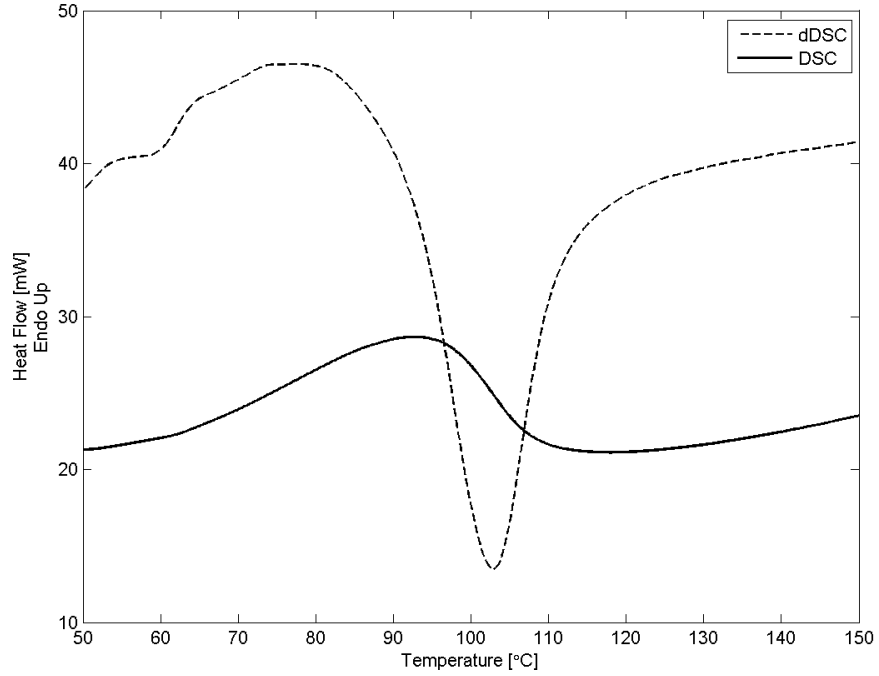

Figure 46: DSC and the associated derivative curve of Cu-B4C-Needles-Water heated at 10°C.min^{-1} under a nitrogen purge (flow rate 25 ml.min^{-1}).

As a result of the significant uptake of water, this guest was studied in multiple desolvation-resolvation steps by DSC. The results are shown in figure 47. The change in the peak area between the original sample and the sample exposed to water for the first time is clearly evident. However, there is almost no change between the sample when it is exposed to water a second time (after a further dehydration step). The actual energy values are summarized in table 12. This suggests that the change responsible for the decreased uptake of water is a once-off process, and that this subtly new structure is capable of exhibiting fully reversible water-uptake behaviour, holding onto the water molecules weaker than either the original Cu-B4C-Needles or Cu-B4C-Xtals.

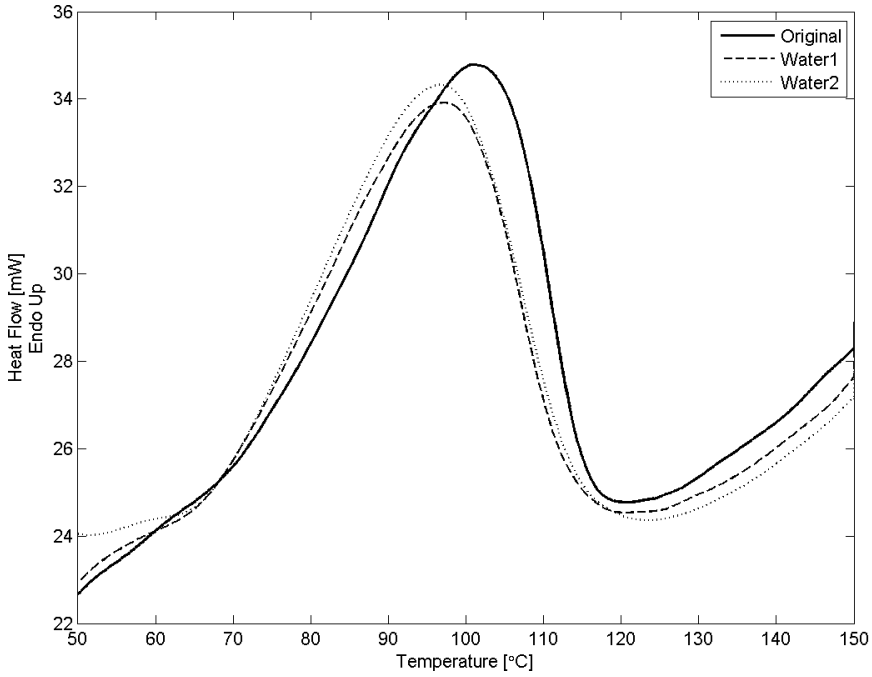

Figure 47: DSC curve of Cu-B4C-Needles exposed to water multiple times, heated at 10°C.min^{-1} under a nitrogen purge (flow rate 25 ml.min^{-1}).

Table 12: Calculated energy values for Cu-B4C-Needles exposed to water multiple times.

Sample	**ΔH [J.g^{-1}]**	**ΔH per Water [kJ.mol^{-1}]**
Cu-B4C-Needles	379(23)	41(3)
Cu-B4C-Needles-Water-1	263(9)	34(1)
Cu-B4C-Needles-Water-2	272(9)	35(1)

4.2 Methanol

Cu-B4C-Needles-Methanol demonstrated a mass gain of 4.61 $\pm$ 0.43 wt%. Assuming that all this mass gain is in the form of methanol molecules, this would equate to a total uptake of 0.5 methanol molecules per formula unit, to give a methanol-containing structure having an empirical formula of $Cu_{2\frac{1}{4}}(OH)_{\frac{1}{2}}B4C{\cdot}1\frac{1}{2}H_2O{\cdot}\frac{1}{2}MeOH$. It may already be noted that this is distinctly different to Cu-B4C-Xtals, which exhibited an uptake of 2.75 methanol molecules per formula unit.

The XRPD pattern of Cu-B4C-Needles-Methanol is shown in figure 48 together with that of Cu-B4C-Needles and Cu-B4C-Needles-Dehydrated. The XRPD pattern contains a peak at $2\theta = 11^\circ$ which is characteristic of Cu-B4C-Needles-Dehydrated. There are three possible reasons for this. The first is that only a small portion of the dehydrated framework was able to take up methanol, likely as a result of very slow kinetics. This seems unlikely, since samples left for periods considerably longer than 24 hours did not demonstrate any greater mass gain. Secondly, it is possible that the sample itself had many of the dehydrated crystallites inaccessable to methanol vapour. Once again, this seems unlikely, since water was able to interact with all of the dehydrated structure. The final, most likely possiblilty is that the methanol does not get included in the pores, but rather simply settles on the surface of the framework via physisorption forces. This would account for the large amount of dehydrated structure present in the XRPD pattern, while the appearance of peaks characteristic of Cu-B4C-Needles may simply

be a result of the sample rehydrating in the presence of atmospheric water during the XRPD run.

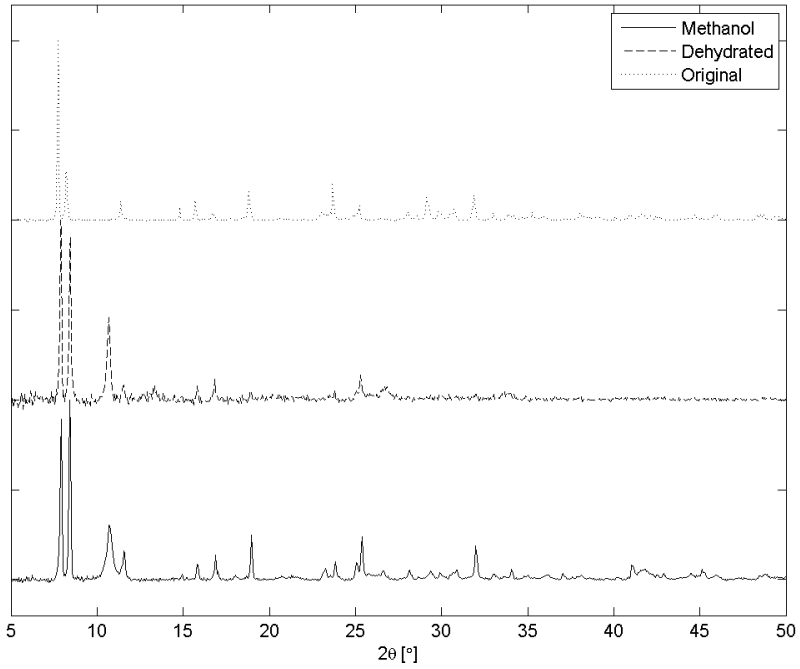

Figure 48: XRPD pattern of Cu-B4C-Needles-Methanol, which suggests a large portion of the framework remains in the dehydrated state.

The IR spectrum in figure 49 does not provide much evidence supporting or rejecting the idea that methanol has been included within the pore. Cu-B4C-Needles-Methanol has bands that coincide with those of Cu-B4C-Needles. The only exception is the band at 1298 cm^{-1}. This band is in the region associated with a carboxylate stretch and is present in Cu-B4C-Needles-Dehydrated. This supports the XRPD data, which suggests that the dehydrated framework is present. It is not possible to distinguish any O-H stretches or bends that are unique to methanol.

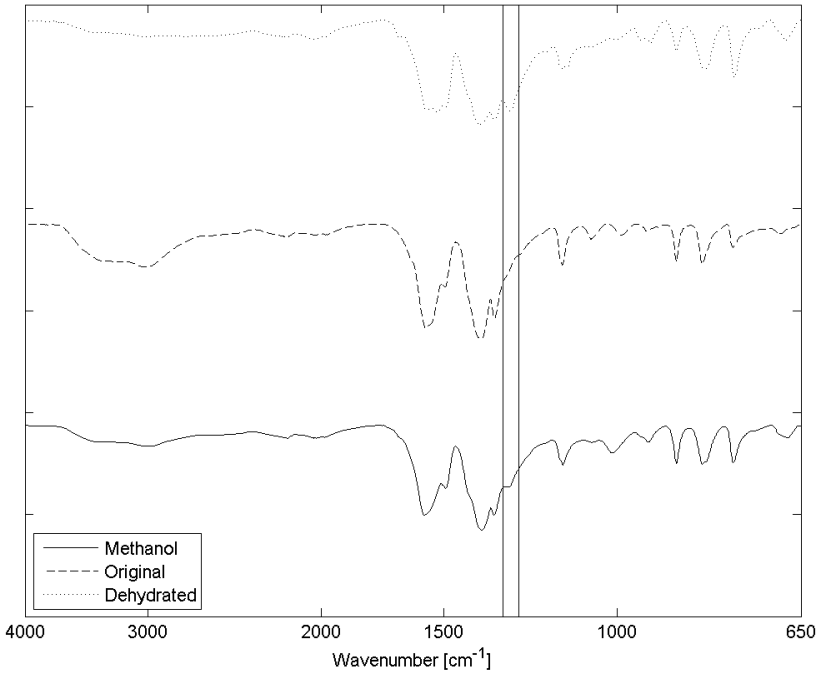

Figure 49: IR spectrum of Cu-B4C-Needles-Methanol. It is not possible to distinguish between O-H stretches and bends belonging to methanol from those belonging to water.

The TGA data, shown in figure 50, supports this evidence. It exhibits a three-step mass loss. An initial mass loss of 3.9 ± 0.1 wt% occurs between 50°C and 90°C during mass loss step (i). This may be interpreted as the loss of half a methanol molecule (calculated loss: 3.6 wt%). Mass loss (ii) follows immediately and results in a final total mass loss of 10.0 ± 1.2 wt% by 250°C. This corresponds to the loss of the remaining 1.5 water molecules that were not removed during the dehydration step (calculated loss: 9.6 wt%) during step (ii). Mass loss (iii) occurs from 250°C, which is at lower temperature than the equivalent mass loss step in Cu-B4C-Needles. This suggests that the methanol molecules might cause some destability to the framework. However, the mass loss between 250° and 280° is sufficiently small that were 280° to be chosen as the end of mass loss (ii), the same conclusions regarding the relative

amounts of water and methanol could be reached. The final residual mass of 43.2 ± 0.9 wt% is higher than that of the original Cu-B4C-Needles, which supports the fact that a lower mass of methanol was taken up compared to the amount of water removed during the dehydration step.

As with water, there is a noticeable difference when comparing Cu-B4C-Needles to Cu-B4C-Xtals, which took up almost three methanol molecules per formula unit.

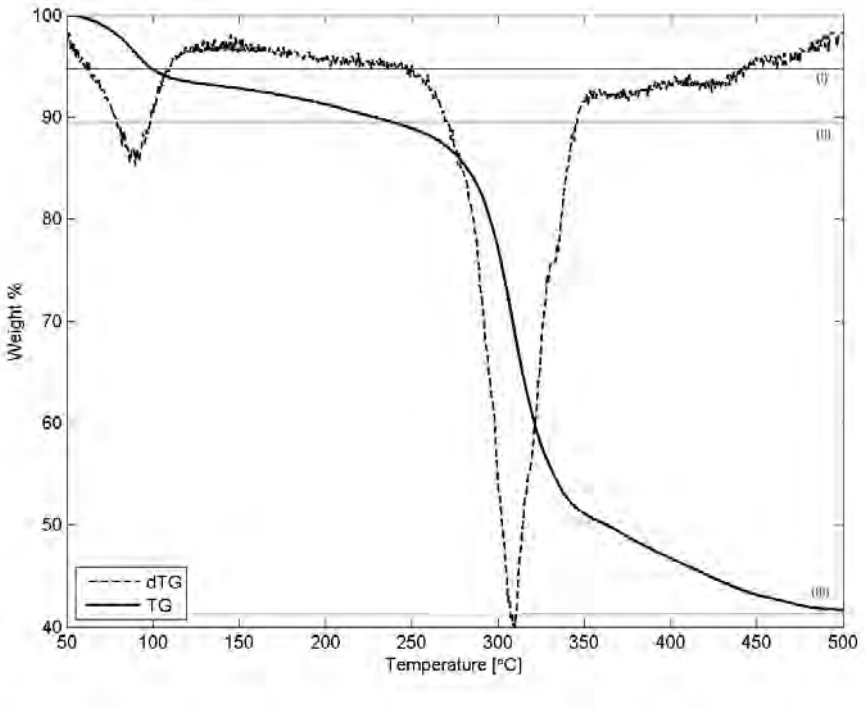

Figure 50: TGA and the associated derivative curve of Cu-B4C-Needles-Methanol heated at 10°C.min^{-1} under a nitrogen purge (flow rate 25 ml.min^{-1}).

DSC data is presented in figure 51. It demonstrates an endothermic process occuring over the temperature range of 55°C to 85°C. The temperature range of this endotherm corresponds to the proposed loss of 0.5 methanol molecules during mass loss stage (i). The enthalpy change associated with this process is 30.6 ± 6.0 J.g^{-1} of parent material. The average energy to remove each of the methanol molecules is thus 27.4 ± 5.4 kJ.mol^{-1}. The

enthalpy change of vaporization[154] for methanol is 35.21 kJ.mol^{-1} . The position of the endotherm, centred at 69°C, is also consistent with the boiling point of methanol, which has a value of 64.6°C.[154] If it is taken into account that a small amount of methanol likely evaporated on moving the Cu-B4C-Needles-Methanol sample to the DSC, this would explain the ΔH value that is slightly lower than expected for the vaporization of methanol. This data lends support to the idea that the methanol has either settled on the surface of the dehydrated framework, or is only at the entrance to the pores, and has not penetrated much deeper.

Since the major difference between Cu-B4C-Xtals and Cu-B4C-Needles is the presence of the sodium cation, it seems likely that the sodium cation is responsible for drawing the methanol into the voids, opening up the pores of the collapsed, dehydrated structure. The absence of the sodium in Cu-B4C-Needles means that there is insufficient force to pull the methanol into the voids and restore the original structure, as is the case with Cu-B4C-Xtals.

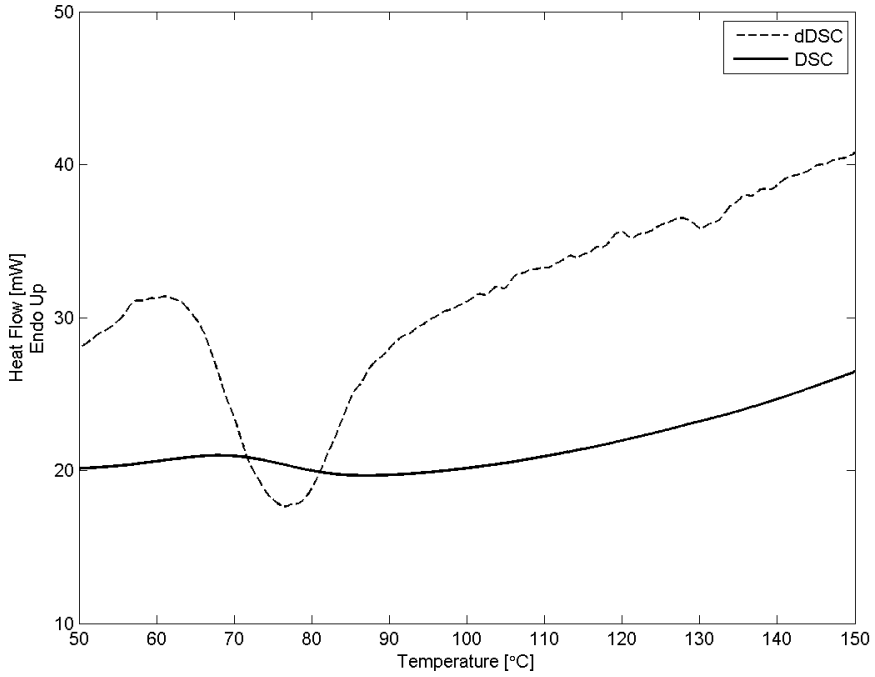

Figure 51: DSC and the associated derivative curve of Cu-B4C-Needles-Methanol heated at 10°C.min^{-1} under a nitrogen purge (flow rate 20 ml.min^{-1}).

In order to make a full comparison with Cu-B4C-Xtals, multiple desolvation/resolvations were studied using methanol. Three different cases were investigated. The first case involved exposure to methanol twice in succession (with the appropriate dehydration step to remove water/methanol prior to exposures). The second case involved exposure to water first, then to methanol, while the third case studied the effect of exposing the sample to methanol first then to water. All cases exhibited endotherms between 50°C and 150°C. The enthalpies associated with each of these endotherms is given in table 13. All cases exhibited endotherms (with associated enthalpies) that were characteristic of the sample when studied in a single-step process. This suggests that methanol did not affect the ability of the dehydrated framework to take up water or not take up methanol. Neither did the change in structure that occurs on the re-uptake of water activate the dehydrated

framework for methanol uptake. As such, the DSC thermograms are not plotted.

Table 13: Calculated energy values for Cu-B4C-Needles exposed to water and methanol multiple times.

Sample	**ΔH [J.g^{-1}]**	**ΔH per Guest [kJ.mol^{-1}]**
Cu-B4C-Needles	379(23)	41(3)
Cu-B4C-Needles-Methanol-1	36(2)	33(1)
Cu-B4C-Needles-Methanol-2	32(7)	29(6)
Cu-B4C-Needles	379(23)	41(3)
Cu-B4C-Needles-Water-1	293(21)	37(3)
Cu-B4C-Needles-Methanol-2	31(9)	28(8)
Cu-B4C-Needles	379(23)	41(3)
Cu-B4C-Needles-Methanol-1	36(2)	33(1)
Cu-B4C-Needles-Water-2	269(11)	35(1)

For comparison, the same enthalpy change for Cu-B4C-Xtals corresponding to the loss of 2.75 methanol molecules per formula unit is 28.9 $\pm$ 3.7 kJ.mol^{-1}. This is essentially the same as that obtained for Cu-B4C-needles. However, the volume of methanol taken up by Cu-B4C-Xtals is considerably larger than that taken up by Cu-B4C-Needles.

In summary, it appears that the sodium cation plays an important role in pulling the methanol molecules into the collapsed, dehydrated framework of Cu-B4C-Xtals, restoring it to its original structure, thus allowing the inclusion of a large amount of methanol. The absence of this sodium cation in Cu-B4C-Needles does not allow the methanol to be pulled in and, as a result, the structure remains in a dehydrated, collapsed state and is unable to accomodate much methanol.

4.3 Acetaldehyde

Cu-B4C-Needles-Acetaldehyde demonstrated a mass gain of 10.2 ± 2.0 wt%. In all cases the sample was wet, suggesting that acetaldehyde had simply settled in the sample pan. There was no colour change exhibited by the sample to suggest uptake. The large uncertainty in the mass uptake also suggests the mass gain is not a result of acetaldehyde inclusion within the voids of the framework. However, if it assumed the acetaldehyde is taken up by the framework, the mass gain would correspond to one acetaldehyde molecule per formula unit, to give a resultant empirical formula of $Cu_{2\frac{1}{4}}(OH)_{\frac{1}{2}}B4C{\cdot}1\frac{1}{2}H_2O{\cdot}1(CH_3CH{=}O)$.

The XRPD pattern in figure 52a indicates the presence of the original structure. This might suggest that the acetaldehyde has indeed been included in the voids and caused a restoration to the original structure. Alternatively, the sample might just have rehydrated in the moist air faster than others. The IR spectrum in figure 52b, however, resembles that of the dehydrated framework, rather than that of the original sample. However, the presence of a vibrational mode at 1731 cm^{-1} may be assigned to the C=O stretch of acetaldehyde,[155] which is expected to be seen at 1730 cm^{-1}. This suggests a small amount of acetaldehyde may be incorporated within the framework, if only at the entrance to the voids, or on the surface of the MOF.

The TGA thermogram in figure 52c consists of four mass losses. The first mass loss at (i) occurs between 50°C and 110°C and ends with a total mass loss of 6.9 ± 3.2 wt%. This likely corresponds to the loss of acetaldehyde from the sample. Acetaldehyde has a boiling point of 20.2°C,[154] so it is expected to evaporate very fast at ambient conditions. The large error is likely a result of a variable amount of acetaldehyde which condensed in each of the sample pans. This supports the idea that most acetaldehyde is not included within the framework, but rather is simply condensate in the sample pan. This mass loss can account for 0.67 of the 1 acetaldehyde molecules (calculated loss: 6.2 wt%). Mass loss (ii) occurs from 110°C to 260°C and has a mass loss of 3.0 ± 1.2 wt%. This may be interpreted as the loss of 1 of the remaining 1.5 water molecules (calculated loss: 3.8 wt%).

Mass loss step (iii), which occurs prior to the main decomposition step, is not observed in other samples, but is reproducible. Cu-B4C-Xtals exhibited a similar shoulder just prior to the main decomposition curve when the sample was exposed to methanol or ethanol,[118] with this loss corresponding to some methanol or ethanol that was strongly coordinated to the framework. For Cu-B4C-Needles-Acetaldehdye, this mass loss is 3.5 ± 0.4 w%. It may be interpreted as the loss of 0.33 acetaldehyde molecules (calculated loss: 3.1 wt%). This suggests that some of the acetaldehyde has indeed been taken up by the framework, which is supported by the IR data. Finally, mass loss (iv) corresponds to the loss of the remaining 0.5 water molecules, as well as the decomposition of the framework, to give a final sample mass equal to 43.0 ± 3.5 wt%.

The DSC data in figure 52d indicates a small endotherm corresponding to mass loss (i). The enthalpy change assciated with this endothermic process is 18.4 ± 4.2 $J.g^{-1}$. This may be interpreted as 17.4 ± 4.2 $kJ.mol^{-1}$ of acetaldehyde molecules that were lost during mass loss step (i). The enthalpy of vapourisation of acetaldehyde[154] is 25.76 $kJ.mol^{-1}$. As with methanol (section 4.2), it is expected that this value will be slightly lower than that expected, since some of the sample would have evaporated prior to analysis. The discrepency is slightly larger, likely a result of a more rapid evaporation in the case of acetaldehyde. No change was evident in the decomposition process. It is likely that if acetaldehyde is given off just prior to the decomposition process, the associated energy change is lost amongst the other energy changes occuring at the same time.

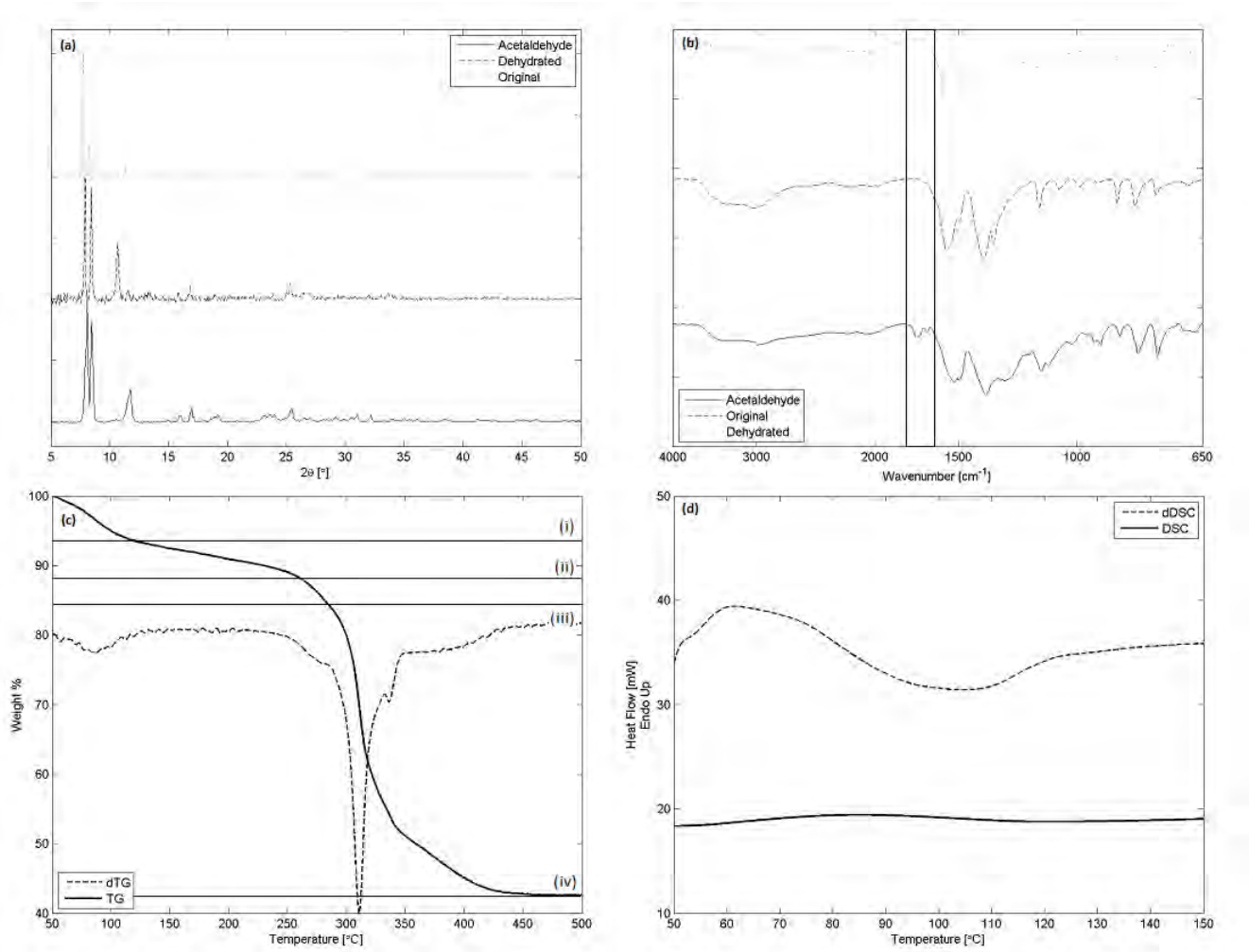

Figure 52: Cu-B4C-Needles-Acetaldehyde: (a) XRPD pattern. (b) IR spectrum. (c) TGA and the associated derivative curve heated at 10°C.min^{-1} under a nitrogen purge (flow rate 25 ml.min^{-1}). (d) DSC and the associated derivative curve heated at 10°C.min^{-1} under a nitrogen purge (flow rate 20 ml.min^{-1}).

4.4 Acetonitrile

Cu-B4C-Needles-Acetonitrile demonstrated a mass gain of 0.08 ± 0.79 wt%. This mass gain was assumed to be zero, giving an empirical structure of $Cu_{2\frac{1}{4}}(OH)_{\frac{1}{2}}B4C{\cdot}1\frac{1}{2}H_2O$, identical to that of Cu-B4C-Needles-Dehydrated.

The XRPD pattern in figure 53a indicates the presence of the dehydrated framework, with the presence of peaks coresponding to Cu-B4C-Needles attributed to partial rehydration upon exposure to moist air during the XRPD run. The IR spectrum in figure 53b also resembles that of the dehydrated framework, rather than that of the original sample. In addition, no C-N stretch was observed in the region of 2260 to 2240 cm^{-1}, the region associated with aliphatic nitrile stretches, to suggest that any acetonitrile was present.[155]

The TGA thermogram in figure 53c exhibits three mass loss stages. The first mass loss at (i) occurs between 50°C and 70°C and ends with a total mass loss of 0.3 ± 0.2 wt%. This is attributed to a small amount of water that was taken up by the sample on transferring from the dessicator to the instrument. Mass loss (ii) follows from 70°C to 275° ends with a total mass loss of 4.4 ± 0.2 %. This may be interpreted as the loss of 1 of the remaining 1.5 water molecules (calculated loss: 4.2 wt%). The final loss step (iii) is the loss of the remaining 0.5 water molecules, together with the decomposition of the framework. The final mass of the sample is 46.0 ± 0.6 wt%, in agreement with what is expected for a structure that has not taken up any guest molecules (calculated final mass: 47 wt%).

The DSC data in figure 53d provides no evidence to suggest that any acetonitrile was taken up by the dehydrated framework.

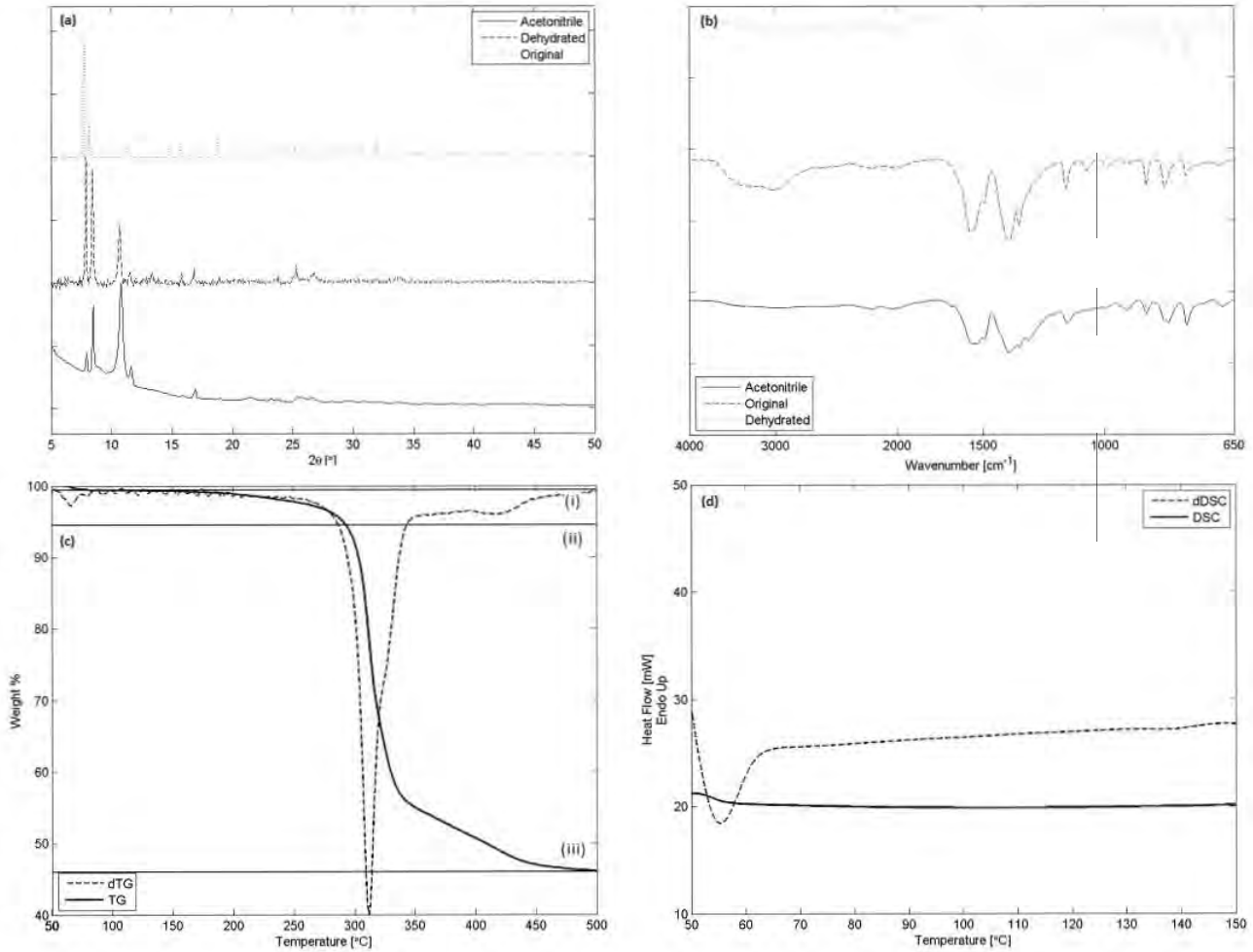

Figure 53: Cu-B4C-Needles-Acetonitrile: (a) XRPD pattern. (b) IR spectrum. (c) TGA and the associated derivative curve heated at 10°C.min^{-1} under a nitrogen purge (flow rate 25 ml.min^{-1}). (d) DSC and the associated derivative curve heated at 10°C.min^{-1} under a nitrogen purge (flow rate 20 ml.min^{-1}).

4.5 Carbon Disulfide

Cu-B4C-Needles-Carbondisulfide demonstrated a mass gain of 18.72 ± 0.26 wt%. The resulting colour change (dark blue to light blue-green) together with the mass change suggested that carbon disulfide was not taken up, but rather that water was, likely the result of wet carbon disulfide. All the data given below is consistent with this hypothesis. Assuming the mass gain is a result of water uptake, the empirical formula for Cu-B4C-Needles-Carbondisulfide is $Cu_{2\frac{1}{4}}(OH)_{\frac{1}{2}}B4C{\cdot}6H_2O$.

The XRPD pattern in figure 54a indicates a restoration to the original Cu-B4C-Needles, while the IR spectrum in figure 54b also resembles that of the original Cu-B4C-Needles, with the additional band at 1416 cm^{-1}, as was observed with Cu-B4C-Needles-Water. In addition, no C-S stretch was observed. However, the intensity of such a band is very weak.[155] As such, it is not good for characterisation, hence IR results likely don't yield any information regarding the presence or absence of carbon disulfide.

The TGA thermogram in figure 54c is comprised of four mass losses. The first mass loss (i) occurs between 50°C and 65°C and ends with a total mass loss of 1.7 ± 0.1 wt%. This is attributed to the loss of 0.5 water molecules (calculated loss: 1.8 wt%). Mass loss (ii) follows from 65°C to 115° with a final total mass loss of 14.5 ± 0.4 wt%. This may be interpreted as the loss of a total four water molecules (calculated loss: 14.1 wt%) by the end of step (ii). Loss step (iii) occurs over the broad range of 115°C to 275°C with a mass loss of 9.3 ± 0.9 wt%. This is larger than the mass loss expected for the expected 1.5 water molecules (calculated loss: 5.3 %). However, a closer examination of the derivative curve reveals that this mass loss may indeed be a two-step process, which might suggest the presence of a small amount of carbon disulfide as well. The final mass of the sample upon completion of mass loss (iv) is 38.1 ± 0.7 wt%.

The DSC data presented in figure 54d indicates an endothermic process associated with mass loss (ii). The enthalpy change of this process is 290 ± 14 $J.g^{-1}$ and is comparable to that obtained for Cu-B4C-Needles-Water. No other deviations from the DSC thermogram of Cu-B4C-Needles were

observed. Most notably, no energy change could be observed to suggest the presence of any carbon disulfide being liberated during the heating profile.

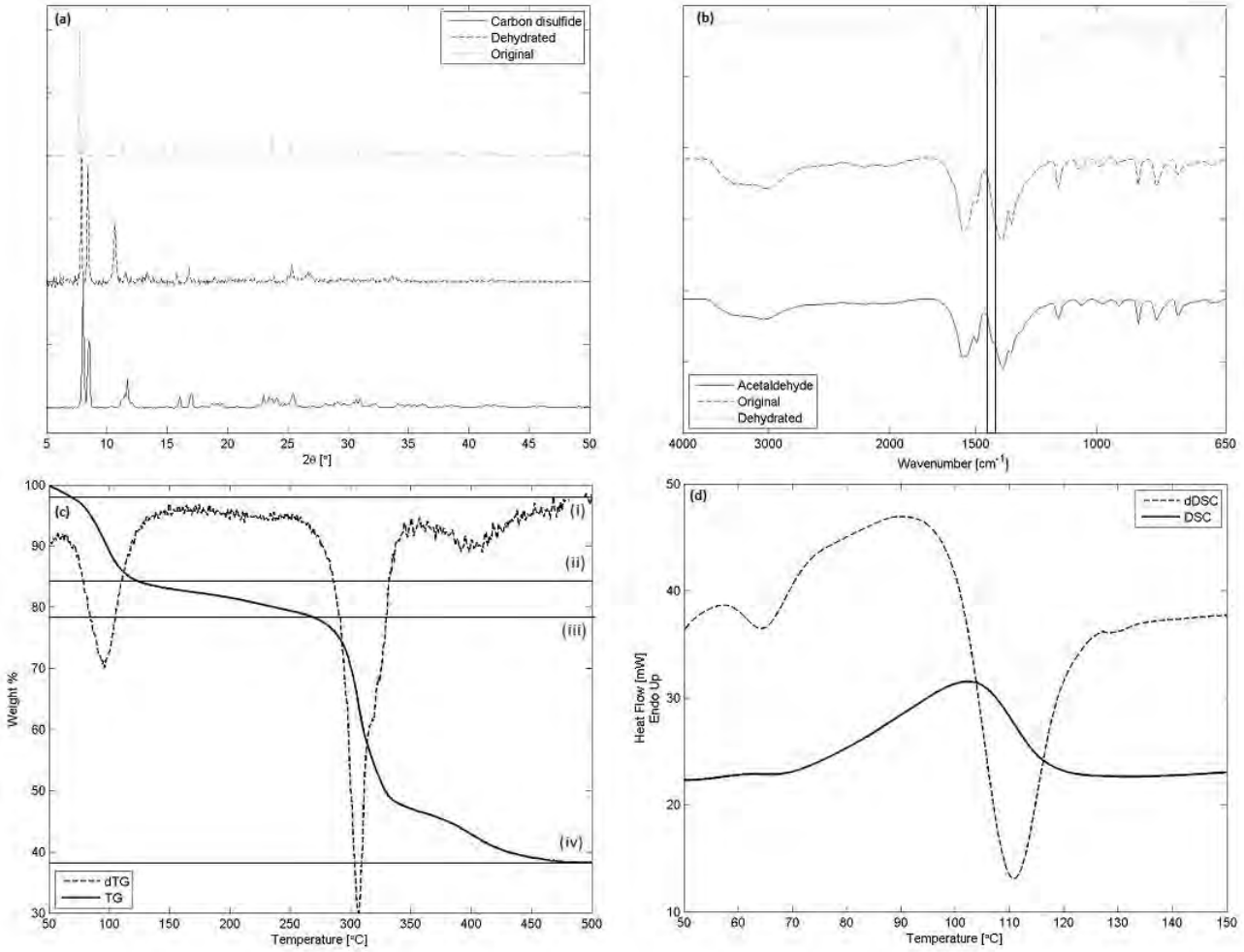

Figure 54: Cu-B4C-Needles-Carbondisulfide: (a) XRPD pattern. (b) IR spectrum. (c) TGA and the associated derivative curve heated at 10°C.min^{-1} under a nitrogen purge (flow rate 25 ml.min^{-1}). (d) DSC and the associated derivative curve heated at 10°C.min^{-1} under a nitrogen purge (flow rate 20 ml.min^{-1}).

4.6 Dimethyl Sulfoxide

Cu-B4C-Needles-DMSO demonstrated a mass gain of 2.7 ± 0.2 wt%. If this mass is attributed to DMSO molecules alone, this would suggest a total of 0.15 DMSO molecules per formula unit, to give an empirical formula of $Cu_{2\frac{1}{4}}(OH)_{\frac{1}{2}}B4C{\cdot}1\frac{1}{2}H_2O{\cdot}0.15((CH_3)_2S{=}O)$. The small amount of DMSO suggests that it is likely located on the surface or at the entrance to the pores, rather than included within the pores themselves.

The XRPD pattern, shown in figure 55a, suggests that DMSO has greatly reduced the crystallite sizes of this MOF, as evidenced by the lack of diffraction peaks. The only peak present does correspond to the XRPD pattern of Cu-B4C-Needles-Dehydrated. This is a reproducible pattern. Slower scans yield a pattern similar to the original Cu-B4C-Needles, likely from rehydration in atmospheric moisture. The IR spectrum in figure 55b, resembles that of the dehydrated framework, rather than that of the original sample. There is no evidence of an S=O stretch, expected at approximately 1050 cm^{-1} which might suggest the presence of DMSO.[155]

The TGA thermogram in figure 55c exhibits three mass losses. The first mass loss at (i) occurs between 50°C and 60°C and ends with a total mass loss of 2.5 ± 1.2 wt%. This might be the removal of 0.15 DMSO molecules (calculated loss: 2.7 wt%). However, the boiling point of DMSO is 189°C, so it is not likely to come off at this low a temperature at such a fast rate. It is more likely that this mass loss correpsonds to that of residual water that was taken up by the sample on transferring it from the dessicator to the TGA instrument. Mass loss (ii) occurs from 60°C to 285° and has a mass loss of 6.6 ± 1.7 wt%. However, the derivative curve suggests this is a two-step process. It is likely that DMSO is liberated during this mass loss step. The loss of one of the remaining 1.5 water molecules, as well as the loss of the 0.15 DMSO molecules (calculated loss: 6.7 wt%) describes this step. Finally, mass loss (iv) corresponds to the loss of the remaining 0.5 water molecules, as well as the decomposition of the framework, to give a final sample mass equal to 44.8 ± 1.5 wt%. There is no noticeable change in the decomposition profile to suggest that DMSO altered the framework in any way.

The DSC data in figure 55d does not show any energy changes that are different to that of Cu-B4C-Needles-Dehydrated. It is likely that with only 0.15 DMSO molecules present per formula unit, the energy change associated with its liberation is too small to be observed. Once again, the decomposition process was unchanged.

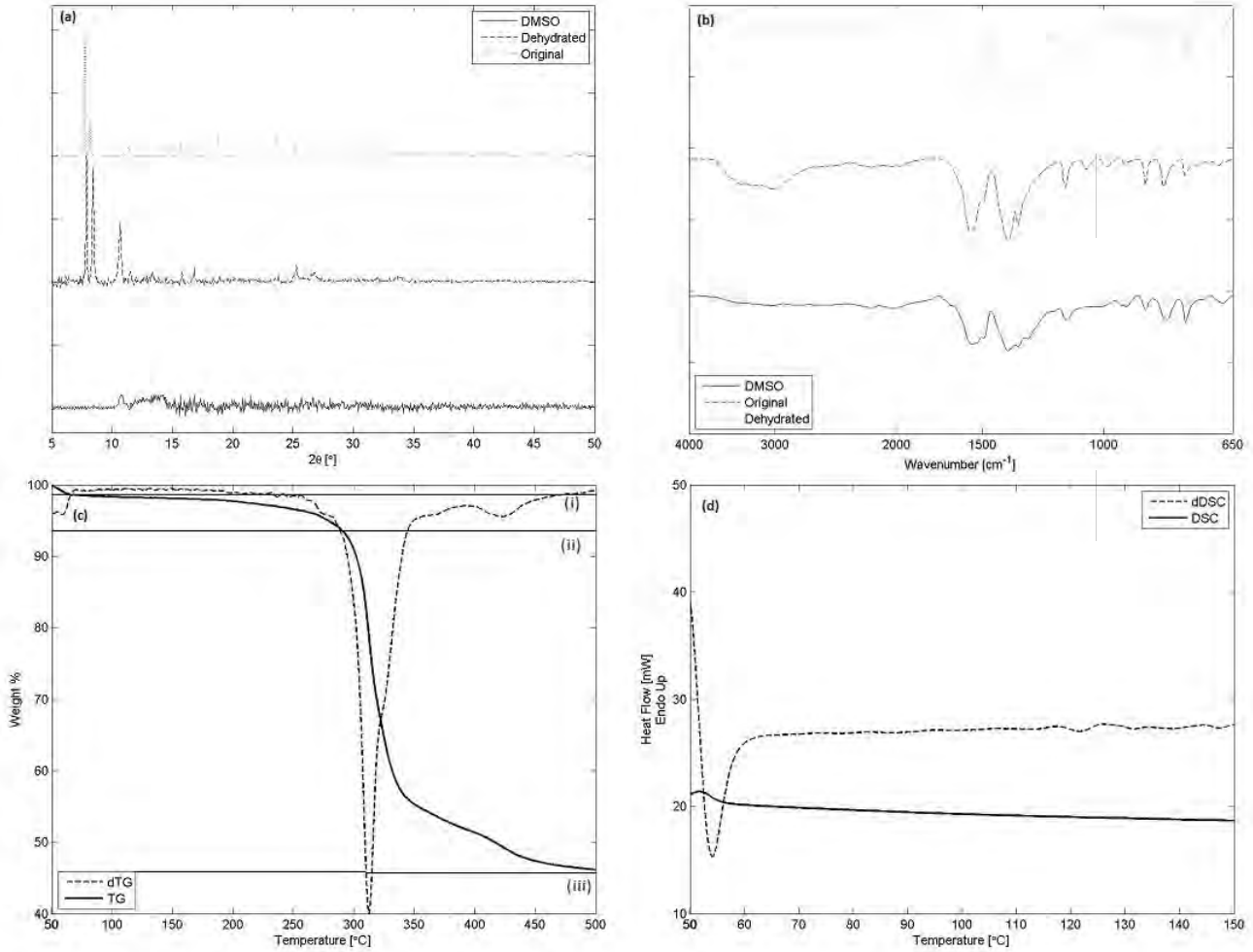

Figure 55: Cu-B4C-Needles-DMSO: (a) XRPD pattern. (b) IR spectrum. (c) TGA and the associated derivative curve heated at 10°C.min^{-1} under a nitrogen purge (flow rate 25 ml.min^{-1}). (d) DSC and the associated derivative curve heated at 10°C.min^{-1} under a nitrogen purge (flow rate 20 ml.min^{-1}).

4.7 Ethanol

Cu-B4C-Needles-Ethanol demonstrated a mass gain of only 0.95 ± 0.77 wt%. This mass gain was assumed to be zero, to yield an empirical structure of $Cu_{2\frac{1}{4}}(OH)_{\frac{1}{2}}B4C{\cdot}1\frac{1}{2}H_2O$, identical to that of Cu-B4C-Needles-Dehydrated.

The XRPD pattern in figure 56a indicates the presence of the dehydrated framework, with the presence of peaks coresponding to Cu-B4C-Needles attributed to partial rehydration upon exposure to moist air during the XRPD run. The IR spectrum in figure 56b also resembles that of the dehydrated framework, rather than that of the original sample. In addition, it was not possible to identify any O-H stretches or bends that might be uniquely assigned to ethanol.

The TGA thermogram, shown in figure 56c, consists of three mass losses. The first mass loss at (i) occurs between 50°C and 70°C and ends with a total mass loss of 0.75 ± 0.04 wt%. This is attributed to a small amount of water that was taken up by the sample on transferring from the dessicator to the instrument, or trace amounts of ethanol that were responsible for the very slight mass gain. Mass loss (ii) follows from 70°C to 280°C and ends with a mass loss of 4.2 ± 0.5 wt%. This may be interpreted as the loss of one of the remaining 1.5 water molecules (calculated loss: 4.2 wt%). The final loss step (iii) is the loss of the remaining 0.5 water molecules, together with the decomposition of the framework. The final mass of the sample is 46.2 ± 0.6 wt%, in agreement with what is expected for a structure that has not taken up any guest molecules (calculated final mass: 47 wt%).

The DSC data presented in figure 56d presents no evidence to suggest that any ethanol was taken up by the dehydrated framework.

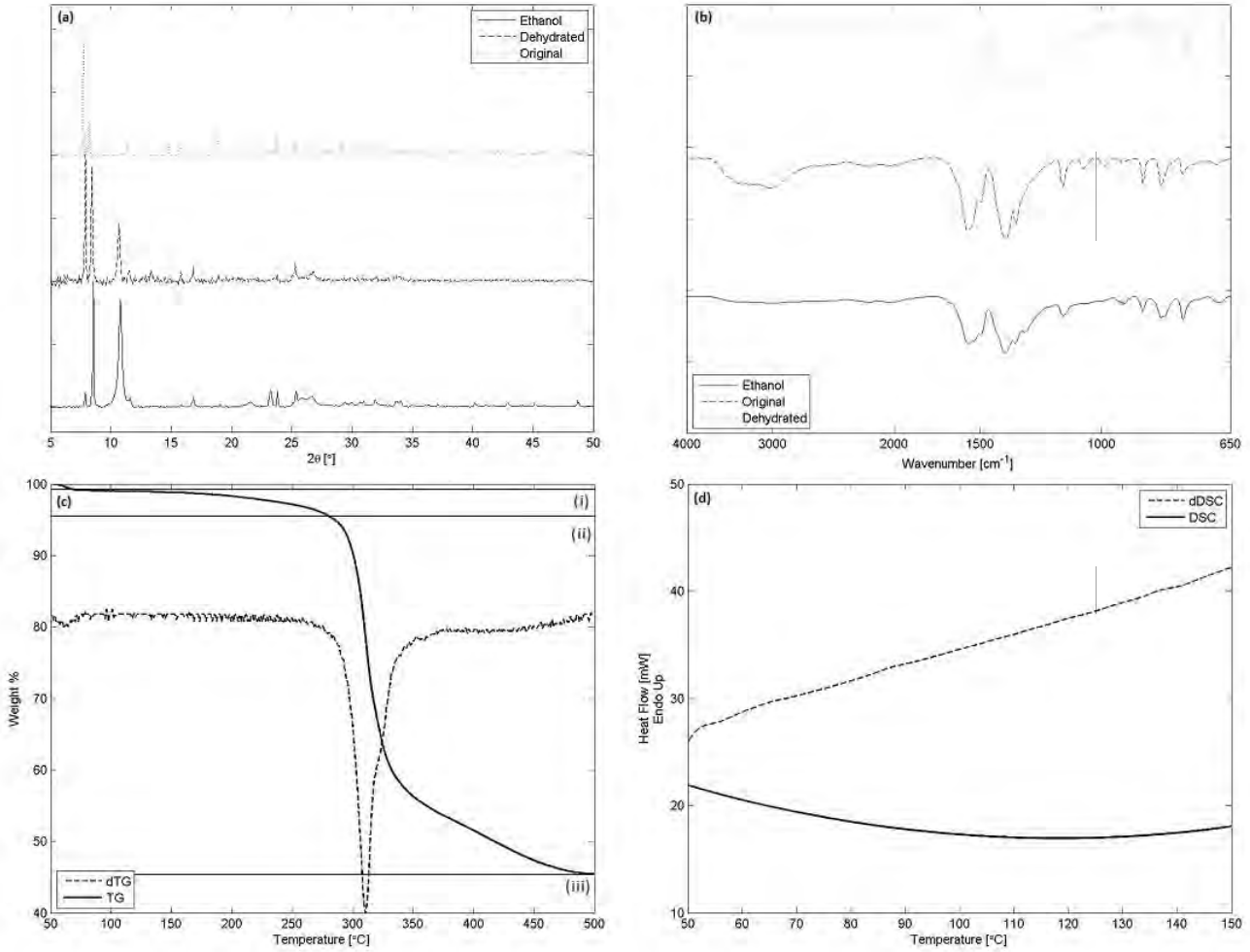

Figure 56: Cu-B4C-Needles-Ethanol: (a) XRPD pattern. (b) IR spectrum. (c) TGA and the associated derivative curve heated at 10°C.min^{-1} under a nitrogen purge (flow rate 25 ml.min^{-1}). (d) DSC and the associated derivative curve heated at 10°C.min^{-1} under a nitrogen purge (flow rate 20 ml.min^{-1}).

4.8 Formaldehyde

Cu-B4C-Needles-Formaldehyde demonstrated a mass gain of 18.25 ± 0.31 wt%. However, formaldehyde was used as a 37% solution in water*. It was assumed, therefore, that the mass increase was a result of water uptake, to yield an empirical formula for Cu-B4C-Needles-Formaldehyde of $Cu_{2\frac{1}{4}}(OH)_{\frac{1}{2}}B4C{\cdot}6H_2O$, the same as that for Cu-B4C-Needles-Water.

The XRPD pattern, shown in figure 57a, indicates a restoration to the original Cu-B4C-Needles, while the IR spectrum in figure 57b also resembles that of the original Cu-B4C-Needles, with the additional band at 1416 cm^{-1} that was also observed in Cu-B4C-Needles-Water. No additional C=O stretch was visible that might be uniquely assigned to formaldehyde.

The TGA thermogram in figure 57c consists of four mass losses. The first mass loss at (i) occurs between 50°C and 65°C and ends with a total mass loss of 1.8 ± 0.2 wt%. This is attributed to the loss of 0.5 water molecules (calucluated loss: 1.8 wt%). Mass loss (ii) follows from 65°C to 115°C, with a final total mass loss of 14.4 ± 0.1 wt%. This may be interpreted as the loss of a total four water molecules (calculated loss: 14.1 wt%) upon completion of step (ii). Loss step (iii) occurs over the broad range of 115°C to 250°C with a mass loss of 5.2 ± 0.4 wt%. This is attributed to the loss of 1.5 of the remaining two water molecules (calculated loss: 5.3 wt%). The final mass of the sample upon completion of mass loss (iv) is 40.0 ± 0.3 wt%, and is described by the removal of the last 0.5 water molecules as well as the decomposition of the framework.

The DSC data in figure 57d indicates an endothermic process associated with mass loss (ii). The enthalpy change of this process is 278 ± 10 $J.g^{-1}$ and is comparable to that obtained for Cu-B4C-Needles-Water. No other deviations from the DSC thermogram of Cu-B4C-Needles were observed.

*It was not possible to distill pure formaldehyde from this, since formaldehyde is gaseous at room temperature - its boiling point is -21°C.[151]

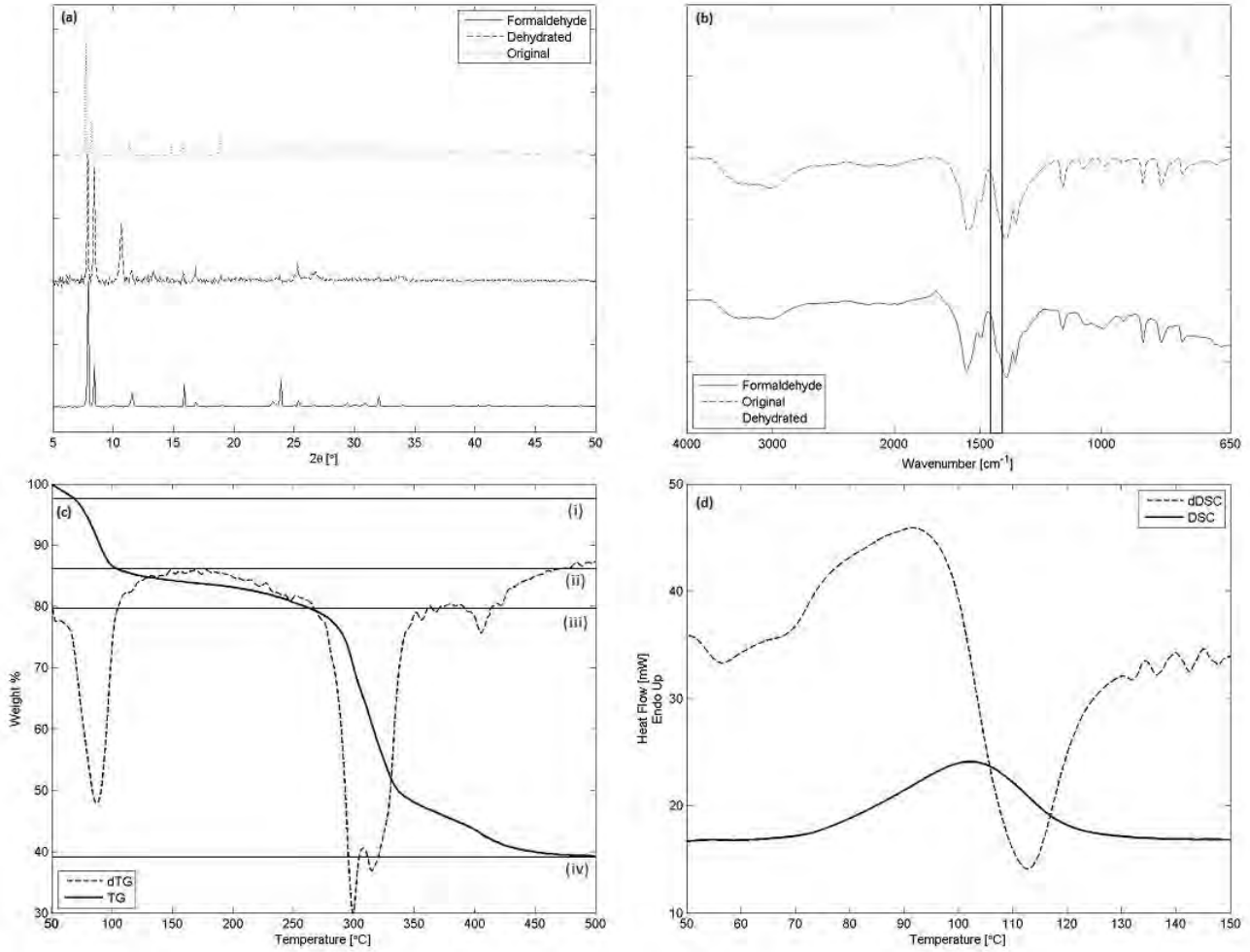

Figure 57: Cu-B4C-Needes-Formaldehyde: (a) XRPD pattern. (b) IR spectrum. (c) TGA and the associated derivative curve heated at 10°C.min^{-1} under a nitrogen purge (flow rate 25 ml.min^{-1}). (d) DSC and the associated derivative curve heated at 10°C.min^{-1} under a nitrogen purge (flow rate 20 ml.min^{-1}).

4.9 Formamide

Cu-B4C-Needles-Formamide demonstrated a mass gain of 2.10 ± 0.20 wt%. Assuming this mass is all a result of formamide, the expected empirical structure of Cu-B4C-Needles-Formamide is $Cu_{2\frac{1}{4}}(OH)_{\frac{1}{2}}B4C{\cdot}1\frac{1}{2}H_2O{\cdot}\frac{1}{5}CHONH_2$.

The XRPD pattern in figure 58a indicates the presence of the dehydrated framework, with the presence of peaks corresponding to Cu-B4C-Needles attributed to partial rehydration upon exposure to moist air during the XRPD run. The IR spectrum in figure 58b also resembles that of the dehydrated framework, rather than that of the original sample. In addition, it was not possible to identify any N-H or C-N stretches or bends that might be assigned to formamide, likely because the relative amount of formamide is so low.

The TGA thermogram in figure 58c consists of 3 mass losses. The first mass loss at (i) occurs between 50°C and 70°C and ends with a total mass loss of 1.2 ± 0.5 wt%. This is attributed to a small amount of water that was taken up by the sample on transferring from the dessicator to the instrument. Mass loss (ii) follows from 70°C to 280° and exhibits a mass loss of 6.4 ± 0.7 wt%. This may be interpreted as the loss of one of the remaining 1.5 water molecules, together with the 0.2 formamide molecules (calculated loss: 6.2 wt%). There is no evidence in the derivative curve to suggest formamide coming off in a separate step, thus it is likely that formamide is not a part of the framework, but is rather just present on the surface of the sample or at the entrance to the voids, since formamide has a boiling point of 210°C.[156] The final loss step (iii) is the loss of the remaining 0.5 water molecules, together with the decomposition of the framework. The final mass of the sample is 45.3 ± 0.5 wt%, slightly lower than what is expected for a structure that has not taken up any guest molecules (calculated final mass: 47 wt%), understandable owing to the small mass of formamide that was present.

The DSC data in figure 58d shows no evidence to suggest that any formamide was taken up by the dehydrated framework.

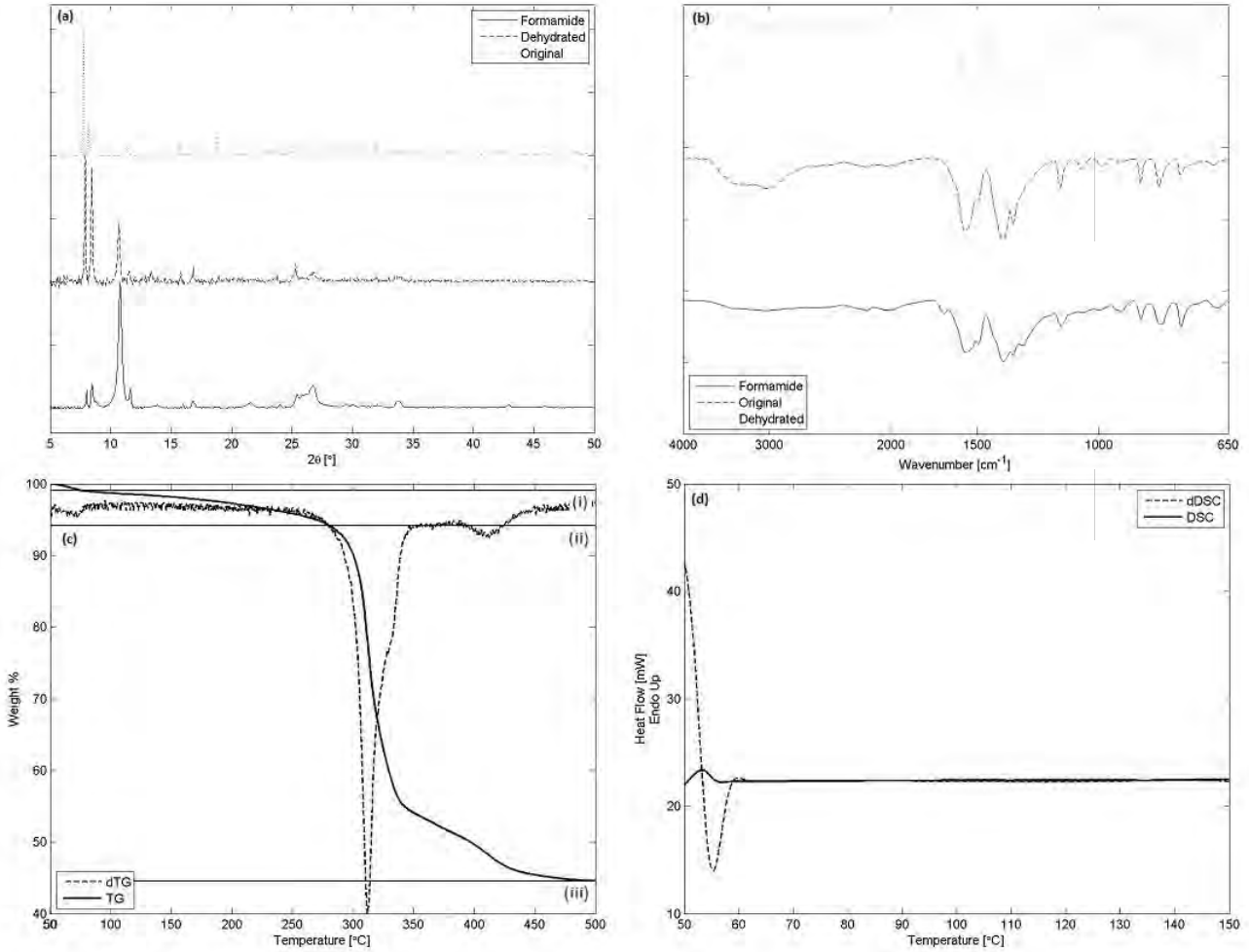

Figure 58: Cu-B4C-Needles-Formamide: (a) XRPD pattern. (b) IR spectrum. (c) TGA and the associated derivative curve heated at 10°C.min^{-1} under a nitrogen purge (flow rate 25 ml.min^{-1}). (d) DSC and the associated derivative curve heated at 10°C.min^{-1} under a nitrogen purge (flow rate 20 ml.min^{-1}).

4.10 N,N'-dimethylformamide

Cu-B4C-Needles-DMF demonstrated a mass gain of 0.82 ± 0.11 wt%. This small increase in mass is attributed to trace amounts of DMF, resulting in an empirical formula for Cu-B4C-Needles-DMF of $Cu_{2\frac{1}{4}}(OH)_{\frac{1}{2}}B4C{\cdot}1\frac{1}{2}H_2O$, the same as Cu-B4C-Needles-Dehydrated.

The XRPD pattern in figure 59a indicates the presence of the dehydrated framework, with the presence of peaks corresponding to Cu-B4C-Needles attributed to partial rehydration upon exposure to moist air during the XRPD run. The IR spectrum in figure 59b also resembles that of the dehydrated framework, rather than that of the original sample. An amide C=O stretch at approximately 1650 cm^{-1}, characteristic of DMF, is not observed, which suggests no N,N'-dimethylformamide is present.[155]

The TGA thermogram in figure 59c exhibits only two mass losses. The first mass loss at (i) occurs between 50°C and 280°C, with a total mass loss of 6.2 ± 1.8 wt%. This is attributed to the loss of one of the remaining 1.5 water molecules, as well as a residual amount of DMF (calculated loss: 5.1 wt%)). Mass loss (ii) is the loss of the remaining 0.5 water molecules, together with the decomposition of the framework. The final mass of the sample is 48.3 ± 0.9 wt%, in agreement with the value expected for a structure that has not taken up any guest molecules (calculated final mass: 47 wt%).

The DSC data in figure 59d shows no evidence to suggest that any DMF was taken up by the dehydrated framework.

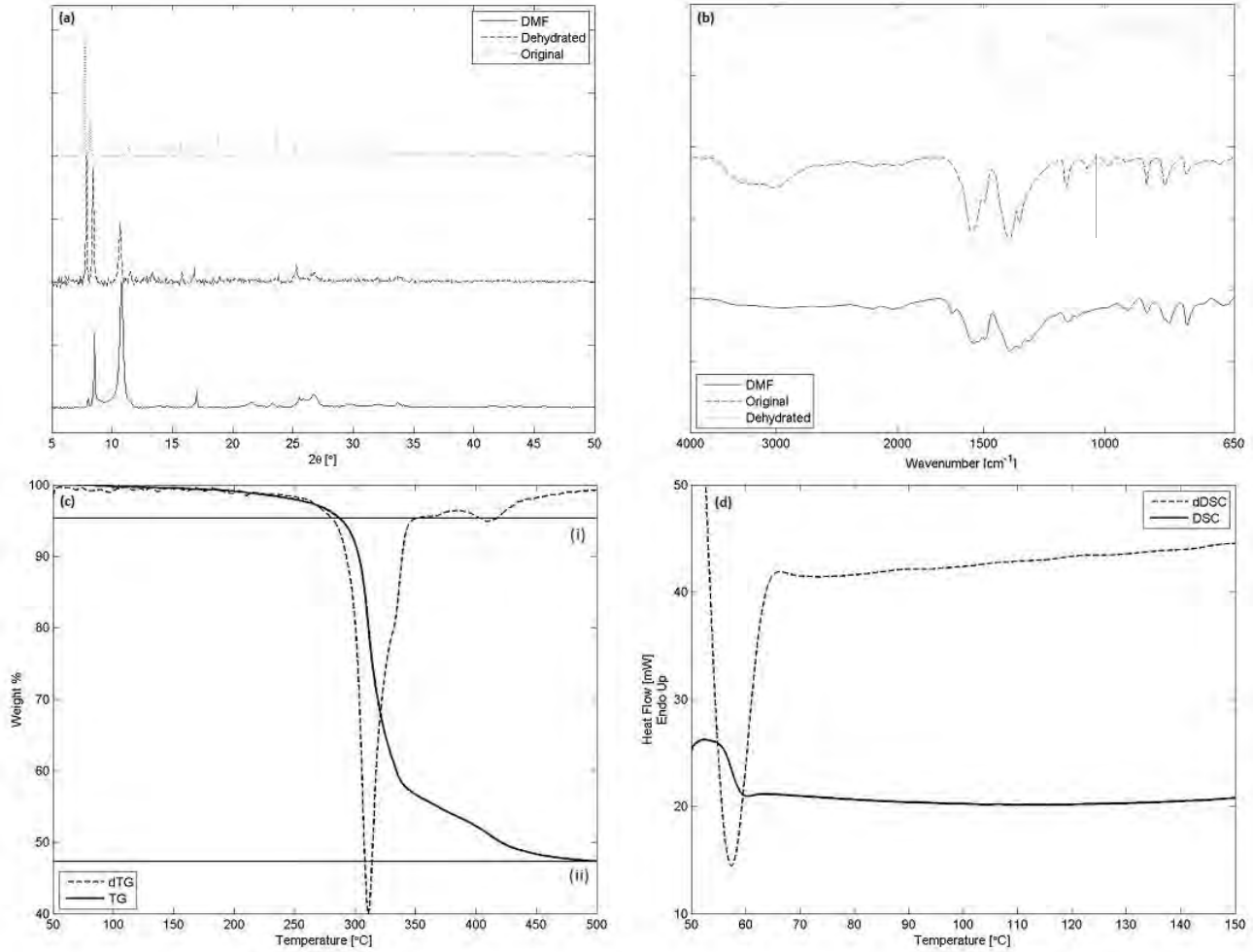

Figure 59: Cu-B4C-Needles-DMF: (a) XRPD pattern. (b) IR spectrum. (c) TGA and the associated derivative curve heated at 10°C.min^{-1} under a nitrogen purge (flow rate 25 ml.min^{-1}). (d) DSC and the associated derivative curve heated at 10°C.min^{-1} under a nitrogen purge (flow rate 20 ml.min^{-1}).

4.11 Pyridine

Cu-B4C-Needles-Pyridine demonstrated a mass gain of 0.79 ± 0.63 wt%. This mass increase was assumed to be zero, leaving an empirical formula for Cu-B4C-Needles-Pyridine of $Cu_{2\frac{1}{4}}(OH)_{\frac{1}{2}}B4C{\cdot}1\frac{1}{2}H_2O$, the same as Cu-B4C-Needles-Dehydrated.

The XRPD pattern in figure 60a indicates the presence of the dehydrated framework, with almost no contributions from the peaks corresponding to Cu-B4C-Needles. However, they are still present, likely a result of partial rehydration on exposure to atmospheric moisture. The IR spectrum in figure 60b also resembles that of the dehydrated framework, rather than that of the original sample.

The TGA thermogram in figure 60c exhibits only two mass losses. The first mass loss at (i) occurs between 50°C and 280°C, with a total mass loss of 4.1 ± 1.3 wt%. This is attributed to the loss of one of the remaining 1.5 water molecules (calculated loss: 4.2 wt%)). Mass loss (ii) is the loss of the remaining 0.5 water molecules, together with the decomposition of the framework. The final mass of the sample is 46.3 ± 0.5 wt%, in agreement with the value expected for a structure that has not taken up any guest molecules (calculated final mass: 47 wt%).

The DSC data in figure 60d presents no evidence to suggest that any pyridine was taken up by the dehydrated framework.

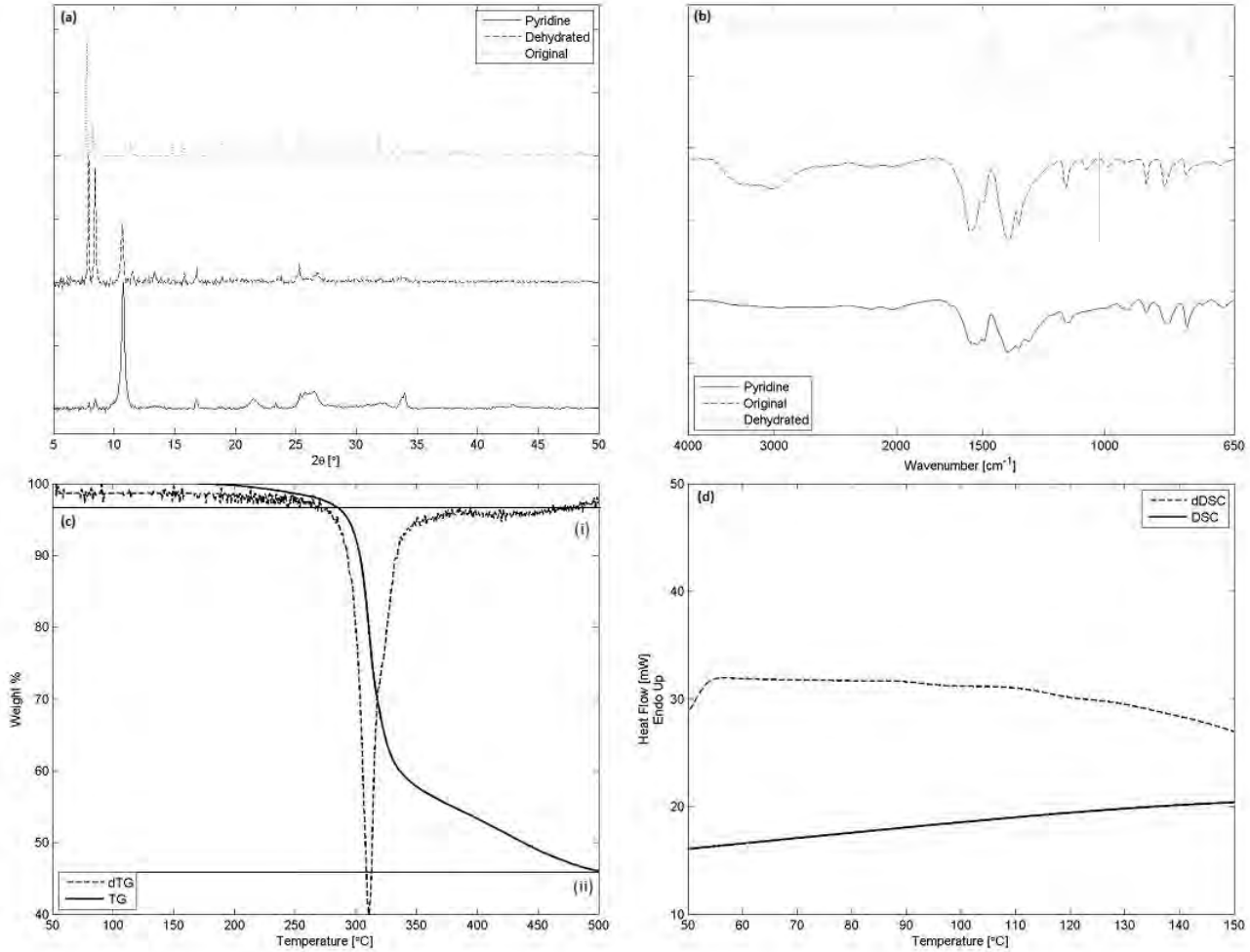

Figure 60: Cu-B4C-Needles-Pyridine: (a) XRPD pattern. (b) IR spectrum. (c) TGA and the associated derivative curve heated at 10°C.min^{-1} under a nitrogen purge (flow rate 25 ml.min^{-1}). (d) DSC and the associated derivative curve heated at 10°C.min^{-1} under a nitrogen purge (flow rate 20 ml.min^{-1}).

5 Molecular Dynamics

In order to further investigate the effect of the sodium cation on the methanol inclusion behaviour of these MOFs, some Car-Parinello molecular dynamics studies were performed. Since the structure of Cu-B4C-Needles is unknown, the molecular dynamics studies were performed on Cu-B4C-Xtals.

As methanol coordination occurs in the dehydrated framework, it was required that some of the waters be removed from the unit cell. There are a total of 16 water molecules within one unit cell of Cu-B4C-Xtals*. Of these, six are coordinated to sodium cations (three to each sodium cation) while the rest are bound by hydrogen bonds. Since these waters are most likely to be released first, they were removed from the structure. However, TGA data suggests that 12 of the 16 water molecules are lost during the dehydration process, thus the water molecules with the greatest Na-O bond lengths were also removed, leaving a total of two water molecules bound to each sodium site. The CPMD input code and the visualisations of these dynamics runs may be found in appendix B.

Initially, one methanol molecule was placed in the void space of the dehydrated framework. As the system evolved with time, the methanol moved closer to one of the sodium sites, eventually coordinating to it via its oxygen atom (average Na-O distance: 2.67 Å). This is better illustrated by figure 61, which shows the distance over time between sodium and the oxygen groups on the methanol and two water molecules coordinated to that sodium. This suggests that the methanol molecules interact strongly with this sodium cation. Figure 62 is a visualisation of the system upon completion of the dynamics run, showing the coordination of methanol to the sodium cation.

*CPMD makes use of periodic boundary conditions (chapter 2.2.8), thus it is only necessary to consider 1 unit cell of Cu-B4C-Xtals.

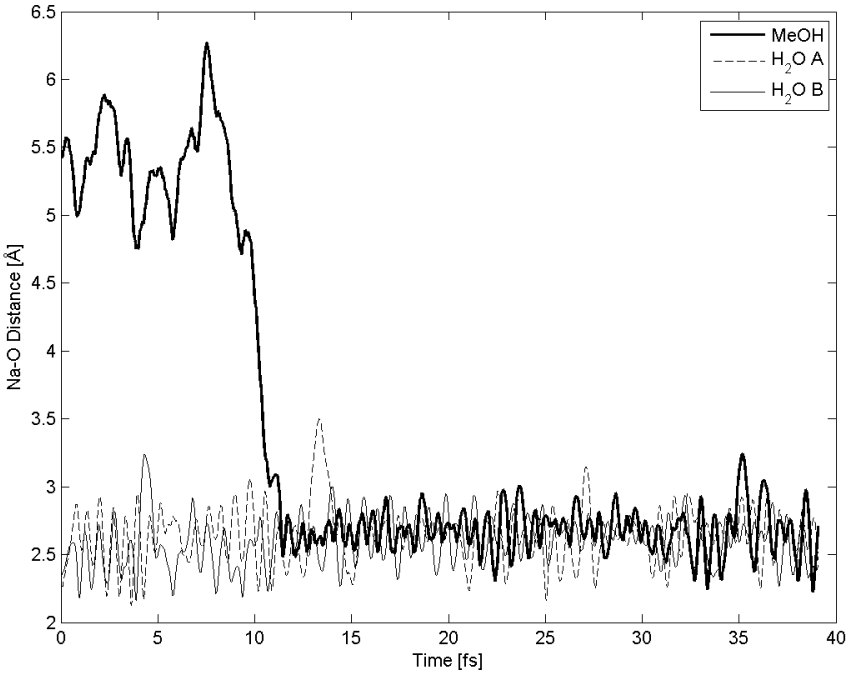

Figure 61: Na-O distances for methanol-sodium and water-sodium over the period of the molecular dynamics run, indicating the coordination of methanol to the sodium cation.

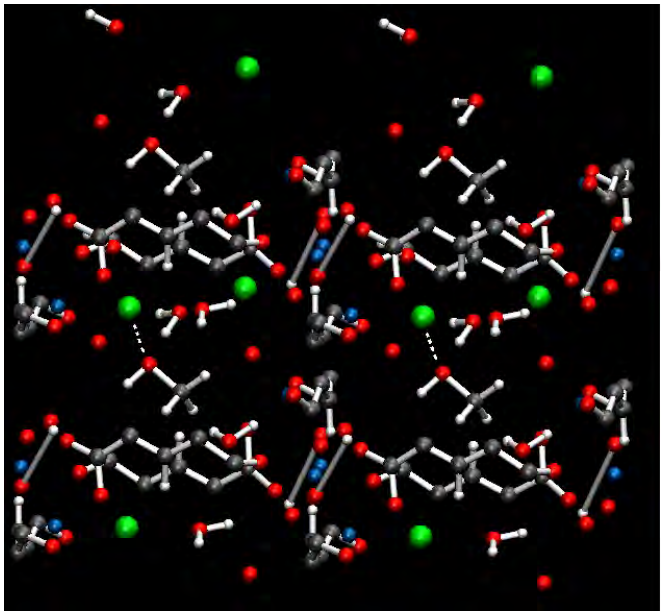

Figure 62: Cu-B4C-Xtals with one methanol molecule per unit cell, illustrating the coordination of methanol to the sodium sites - marked by dotted white lines (blue = copper, red = oxygen, green = sodium, grey = carbon).

When two methanol molecules were added to each unit cell, a similar trend was observed, with each methanol molecule coordinating to a separate sodium cation. A coordinated water molecule was displaced at one of the sites and was instead bound by a hydrogen bond network that existed between it, the methanol molecules and the coordinated water molecules. This suggests that the methanol interacts more strongly with the sodium than the water.

With three methanol molecules in the unit cell, all methanol molecules coordinated to sodium cations (two to one, one to the other). Coordinated water was once again displaced by the methanol. Since the methanol is beginning to occupy majority of the free space in the void, the hydrogen bond network is considerably extended compared to the system containing two methanol molecules. This increase in hydrogen bonding is likely to further stabilise the system.

To evaluate the effect this hydrogen bond network has on the stability of the structure, the energy of formation for each system was calculated. In

order to do this, single point energies were calculated for each system, as well as for methanol and the dehydrated structure. The energy of formation may then be calculated by:

$$\Delta E_{formation} = E_{system} - (E_{dehydrated} + nE_{methanol})$$

where E_{system} is the energy of the framework with methanol in the voids, $E_{dehydrated}$ is the energy of the framework with no methanol molecules present, n is the number of methanol molecules and $E_{methanol}$ is the energy of one methanol molecule.

The energies of formation for each of the systems is given in table 14*. The energy per methanol molecule is also given. This illustrates quite clearly that with more methanol molecules to extend the hydrogen bonding network, the system becomes more stable.

Table 14: The energies of formation for Cu-B4C-Xtals with a different number of methanol molecules in the voids and the average energy of formation per methanol molecule.

Number of MeOH	Δ**E**$_{formation}$	Δ**E**$_{formation}$ **per MeOH**
One	-66.68 kJ.mol^{-1}	-66.68 kJ.mol^{-1}
Two	-193.42 kJ.mol^{-1}	-96.71 kJ.mol^{-1}
Three	-309.79 kJ.mol^{-1}	-103.27 kJ.mol^{-1}

A system with four methanol molecules in each unit cell was also simulated, but carboxylate bonds to the copper vertices break and reform during the run. This is likely a result of the methanol molecules being in too close a proximity to one another, resulting in repulsive forces strong enough to alter the structure of the MOF. Figure 63 and figure 64 illustrate the simulated structure of the framework before the structural change and after the structural change respectively. The carboxylate bonds that change are circled in white.

*A lower energy indicates a more stable system.

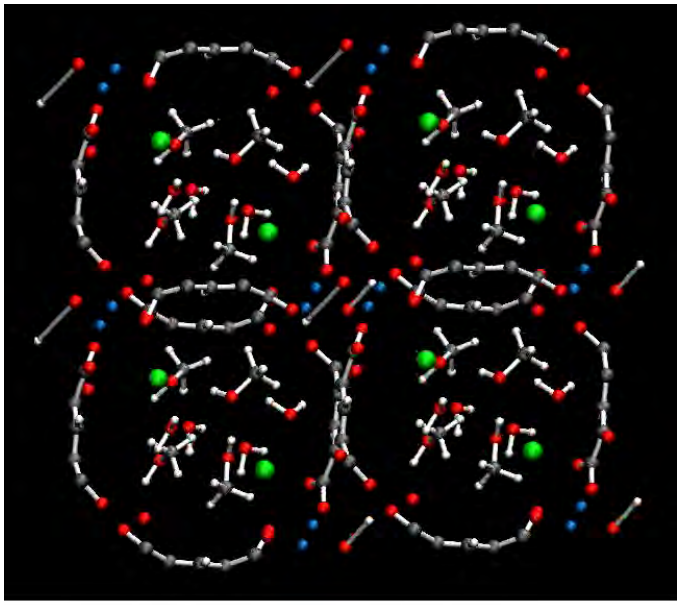

Figure 63: Cu-B4C-Xtals with four methanol molecules per unit cell prior to structural change (blue = copper, red = oxygen, green = sodium, grey = carbon).

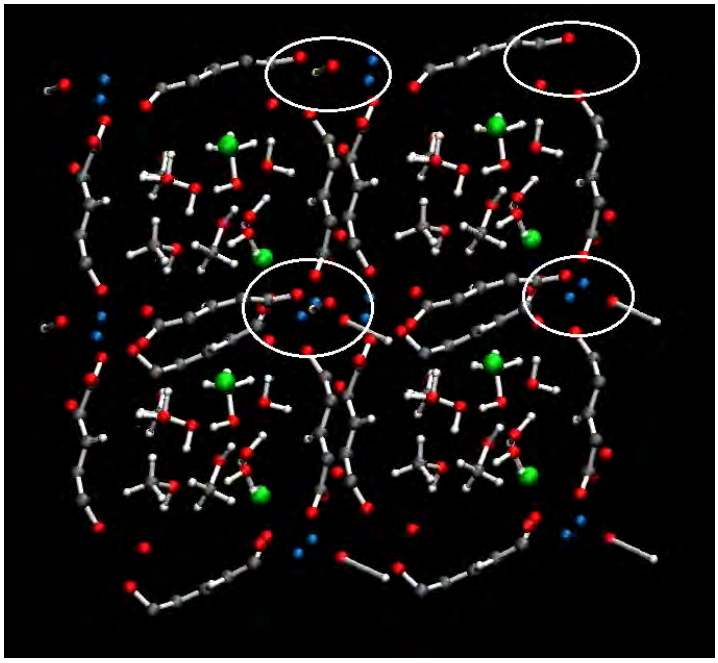

Figure 64: Cu-B4C-Xtals with four methanol molecules per unit cell after structural change. Carboxylate bonds that broke and reformed are indicated by white circles (blue = copper, red = oxygen, green = sodium, grey = carbon).

This data strengthens suggests that a strong interaction between methanol and sodium exists and that it is this interaction that is responsible for pulling methanol into Cu-B4C-Xtals, opening up the structure. The absence of sodium in Cu-B4C-Needles means no methanol-sodium interaction and explains the lack of methanol uptake that is observed.

Cu-B4C-Xtals also exhibited ethanol uptake, while Cu-B4C-Needles did not. Dynamics studies once again suggest it is a strong interaction between the sodium and the oxygen atom on the ethanol that is responsible for the inclusion. Cu-B4C-Xtals does however take up less ethanol than methanol, with the increased size and mass of the ethanol molecules occupying more space in the voids.

6 Conclusions

Throughout the course of this study, Cu-B4C-Xtals and Cu-B4C-Needles were further characterised by *in situ* XRPD and XPS. The *in situ* XRPD was able to provide clear evidence of a structural change upon dehydration in both MOFs.

XPS indicated that these two MOFs are essentially identical, giving further support to the proposed structure of Cu-B4C-Needles. Unfortunately, the high resolution XPS scans were unable to identify the disordered copper that is present in Cu-B4C-Needles, likely because its binding energies are almost identical to the copper atoms at the MOF vertices.

Arguably the most significant result of this study is the observation that Cu-B4C-Needles is unable to incorporate methanol in its voids, while Cu-B4C-Xtals is able to fully revert back to its original structure with the inclusion of methanol. It has been proposed (chapter 4.2) that the attraction between methanol and the sodium cation present in Cu-B4C-Xtals is responsible for the force required to pull the methanol molecules into the collapsed, dehydrated structure. Once methanol has entered the MOF, the structure begins to open up (revert back to its original structure), allowing for the uptake of a larger amount of methanol. This hypothesis was strengthened on the back of molecular dynamics data, presented in chapter 5. It showed a strong interaction between the oxygen atom of the methanol molecules with the sodium site present in Cu-B4C-Xtals. This interaction is not expected in Cu-B4C-Needles owing to the absence of the sodium cation.

The final difference in the guest inclusion behaviour between Cu-B4C-Xtals and Cu-B4C-Needles was observed when the dehydrated frameworks were exposed to water. Cu-B4C-Xtals exhibits a fully reversible rehydration, but Cu-B4C-Needles only undergoes partial restoration. There are two possible explanations for this.

Firstly, although water is able to enter the dehydrated framework of both systems, the presence of sodium in Cu-B4C-Xtals provides a strong enough pull to the water molecules to fully restore the structure. This is not possible in Cu-B4C-Needles owing to the absence of the sodium cation.

The second possibility is that during dehydration, one of the carboxylate groups in Cu-B4C-Needles undergoes a subtle rotation and repositioning within the framework that is irreversible upon rehydration. As a result, this reduces the ability of water to form hydrogen bonds within the framework, and thus less water is taken up. This hypothesis is supported by the decrease in enthalpy per water molecule that is observed in the rehydrated structure (chapter 4.1). It is possible that the presence of the sodium cation either prevents this rotation to the carboxylate group, or that the extra energy provided by the sodium-water interaction is sufficiently strong to reverse it.

All the other solvents that were investigated showed either minimal uptake, which was likely on the surface or at the very entrance to the voids, or no uptake at all. This is common to both Cu-B4C-Needles and Cu-B4C-Xtals.

The final aim of this study was to synthesise Cu-B4C-Xtals and Cu-B4C-Needles via an alternative method that is faster and more efficient than the gel-based synthesis described in chapter 2.1.1 and 2.1.2. A hydrothermal method was investigated and proved successful at synthesising Cu-B4C-Xtalas in almost 100% yield. This conclusion is supported by elemental analysis, XRPD data and thermal analysis data presented in chapter 3.3.

The most critical factor in this is ensuring that pH correction of the B4C solution, to a pH of approximately 5.0, occurs *before* it comes into contact with the copper(II) acetate solution. This ensures that the major product is indeed Cu-B4C-Xtals. Failure to do so results in a mixture of a variety of products.

Since the source of sodium ions for hydrothermally synthesised Cu-B4C-Xtals is the sodium hydroxide used in pH correction and sodium acetate, a logical extension of this result is the synthesis of MOFs analagous to Cu-B4C-Xtals, with the sodium substituted by potassium or lithium for example. This substitution will require the use of the appropriate hydroxide and acetate (in the examples given, this would become lithium or potassium hydroxide for pH correction and lithium or potassium acetate to provide sufficient cations of interest). Since sodium plays such a crucial role in the methanol inclusion of Cu-B4C-Xtals, it is likely that the presence of different cations will allow the MOF to be sensitive to different small guest molecules.

During the synthesis, it is also important that the reaction spends at least 48 hours at 120°C to ensure almost 100% formation of Cu-B4C-Xtals. If the time is too short, the resulting product is a mixture of Cu-B4C-Xtals and Cu-B4C-Needles, while the crystallites are extremely small.

It seems unlikely that this method will be able to produce Cu-B4C-Needles in a major yield, since the cation present in whichever base is chosen for pH correction is likely to sit at the sodium site. Should Cu-B4C-Needles be desired, an alternative method, such as ultrasound or microwave synthesis, needs to be investigated.

A Crystal Data

Table 15 lists the basic crystal data for both Cu-B4C-Xtals and Cu-B4C-Needles. The single crystal data for Cu-B4C-Needles was collected and interpretted by three different crystallographers, with all three agreeing on the unit cell. However, the complete structure was not able to be solved.

Table 15: Crystal data of Cu-B4C-Xtals and Cu-B4C-Needles illustrating the similarities between the two MOFs.

Property	**Cu-B4C-Xtals**	**Cu-B4C-Needles**
Crystal System	Triclinic	Triclinic
Symmetry	$P\bar{1}$	$P\bar{1}$
a	7.8427(2) Å	7.8483(16) Å
b	10.5462(2) Å	10.564(2) Å
c	11.6728(3) Å	11.691(2) Å
α	92.310(1)°	90.95(3)°
β	105.606(1)°	105.42(3)°
γ	91.073(1)°	90.99(3)°
Cell Volume	928.68(4) Å^3	934.0(3) Å^3

Figure 65 illustrates the framework structure of Cu-B4C-Xtals, while figure 66 illustrates the best refinement of Cu-B4C-Needles that was obtained from the single crystal data. It can be seen that the framework itself is nearly identical to that of Cu-B4C-Xtals. However, water molecules were not able to be identified, neither were the copper(II) centres that are expected to be found at the sodium sites of Cu-B4C-Xtals. This is likely a result of the copper(II) being disordered at these sites throughout the framework.

A MOF has been reported[157] which involves post-synthetic functionalization with copper ions to transform it from [Zn(iso)(L)]·2(DMF) (L = N,N'-bis(pyridin-4-yl)-2,2-bipyridine-5,5-dicarboxamide, iso = isophthalate) to a second structure: $[ZnCu_{\frac{1}{3}}(iso)(L)]\cdot\frac{1}{3}Cl\cdot[CuCl_2]_{0.3}\cdot n(DMF)$. The single

crystal structure of the copper-containing MOF was determined using synchrotron radiation (not conventional single crystal analysis with a molybdenum source) suggesting that a synchrotron source might be beneficial in assisting with the identification of the position of the disordered coppers within Cu-B4C-Needles.

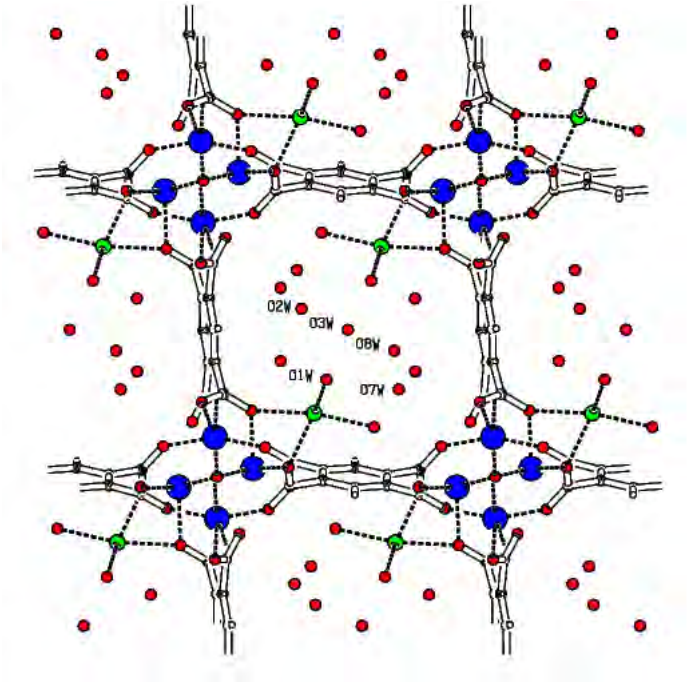

Figure 65: Crystal structure of Cu-B4C-Xtals illustrating the large cavities containing guest water molecules (blue = copper, red = oxygen, green = sodium, white = carbon).

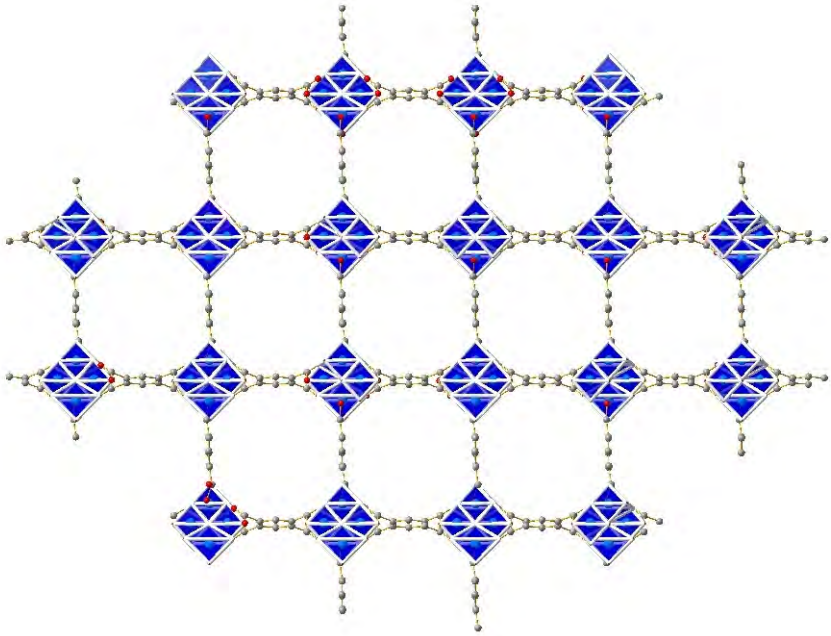

Figure 66: Best refinement for crystal structure of Cu-B4C-Needles. The image was obtained from Alexander Gerisch, Bruker AXS GmbH. Note its similarity to Cu-B4C-Xtals in figure 65 (blue = copper, red = oxygen, grey = carbon).

B CPMD Data

All CPMD input code used during this study may be found on the attached DVD, in the directory CPMD Data/Input Code.

Visualisations of the molecular dynamics runs may be found on the attached DVD, in the directory CPMD Data/Visualisations.

C Hydrothermal Synthesis Rationale

As mentioned in chapter 1.5, Cu-B4C-Xtals is formed over a period of several months, usually 4-6 months, while Cu-B4C-Needles is formed over several weeks, usually 6-8 weeks. This is a very long period of time and is too long should these MOFs become viable for some use on any scale outside that of the laboratory. Another drawback of the gel synthesis setup is that there is alot of waste. Much of the original reagents remain unreacted, while only the larger crystals may be easily separated from the gel medium, thus many of the smaller crystals are lost. As such, the resultant yield is not high.

The hydrothermal method of synthesis[158] is one commonly employed in the synthesis of MOFs and has been used to prepare many copper-based MOFs,[159] most often by utilizing temperatures between 100°C and 200 °C. During the original synthesis of Cu-B4C-Xtals and Cu-B4C-Needles, only 2 hydrothermal syntheses were attempted,[118] using copper(II) acetate or copper(II) carbonate in solution with H_4B4C. Both syntheses resulted in the same product having the empirical formula Cu_2B4C·0.65H_2O. However, this synthesis was performed without any pH correction, so the pH of the resulting solution was between 0 and 1. Figure 67 shows the species distribution of the various protonated forms of H_4B4C under different pH conditions. From this, it may be seen that essentially all the H_4B4C was unprotonated in these syntheses. It was thus important to attempt syntheses involving deprotonated B4C species, since a fully deprotonated B4C anion is found in the MOFs of interest.

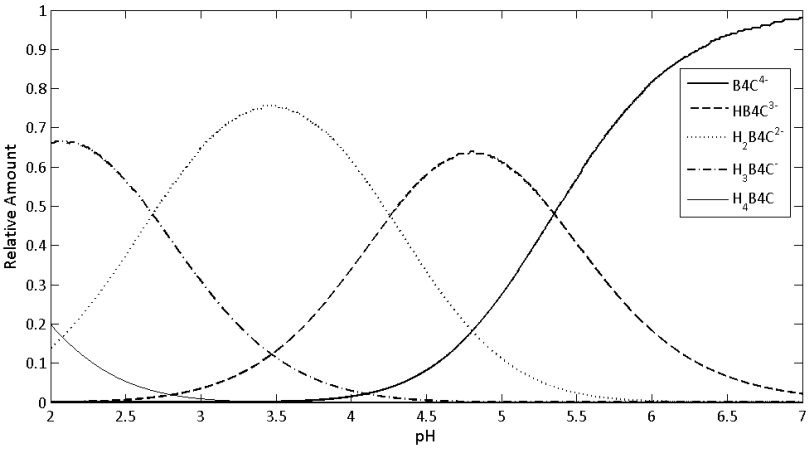

Figure 67: Speciation curve of H_4B4C showing the relative amount of the various species with varying pH, in an aqueous solution. The speciation curves were modelled using the HySS software.[160] The dissociation constants for H_4B4C used in the model were:[161] $k_1 = 1.20 \times 10^{-2}$; $k_2 = 1.34 \times 10^{-3}$; $k_3 = 3.2 \times 10^{-5}$; $k_4 = 2.35 \times 10^{-6}$.

Since the only difference in the synthesis of the Cu-B4C-Needles and Cu-B4C-Xtals is the presence of chloride/nitrate/sulfate and acetate precursors (these are the conjugate bases of a strong and a weak acid respectively), it is believed that pH does have an effect on the formation of the products. As such, the initial hydrothermal syntheses involved variations in the initial pH of the H_4B4C precursor solution. Initially, a pH of 6.5 was used, since this is the pH to which the gels are corrected. Attempts to use a pH of 7 and higher resulted in the formation of metal hydroxides, as was observed with the gels. As such, only pH values below 6.5 were used. These values, were 6.0, 5.0 and 4.0, chosen to cover a broad range. Lower pH values were not studied owing to the need for a fully deprotonated B4C anion in the two MOFs of interest.

Since reaction time and temperature also have an influence on the product during a hydrothermal synthesis,[16,17] it was decided to vary the reaction times and temperatures at a constant pH, in order to investigate what effect this has on the resulting product. In addition to these, a hydrothermal synthesis was performed in a glass vessel, to investigate the effect of the nature of the

reaction vessel on the product.

References

[1] **O. K. Farha and J. T. Hupp**. "Rational design, synthesis, purification, and activation of metal-organic framework materials". *Accounts of Chemical Research* **43**(8) (2010) 1116–1175.

[2] **J. L. Rowsell and O. M. Yaghi**. "Metal-organic rameworks: a new class of porous materials". *Microporous and Mesoporous Materials* **73** (2004) 3–14.

[3] **A. D. Burrows, C. G. Frost, M. F. Mahon and C. Richardson**. "Sulfur-tagged metal-organic frameworks and their post-synthetic oxidation". *Chemical Communications* (28) (2009) 4218–4220.

[4] **A. D. Burrows, C. G. Frost, M. F. Mahon and C. Richardson**. "Post-synthetic modification of tagged metal-organic frameworks". *Angewandte Chemie International Edition in English* **47**(44) (2008) 8482–8486.

[5] **K. K. Tanabe, Z. Wang and S. M. Cohen**. "Systematic functionalization of a metal-organic framework via a postsynthetic modification approach". *Journal of the American Chemical Society* **130**(26) (2008) 8508–8517.

[6] **D. J. Tranchemontagne, J. L. Mendoza-Cortés, M. O'Keeffe and O. M. Yaghi**. "Secondary building units, nets and bonding in the chemistry of metal-organic frameworks". *Chemical Society Reviews* **38**(5) (2009) 1257–1283.

[7] **J.-L. Zhuang, D. Ceglarek, S. Pethuraj and A. Terfort**. "Rapid room-temperature synthesis of metal-organic framework HKUST-1 crystals in bulk and as oriented and patterned thin films". *Advanced Functional Materials* **21**(8) (2011) 1442–1447.

[8] **N. A. Khan, E. Haque and S. H. Jhung**. "Rapid syntheses of a metal-organic framework material $Cu_3(BTC)_2(H_2O)_3$ under mi-

crowave: a quantitative analysis of accelerated syntheses". *Physical Chemistry Chemical Physics* **12**(11) (2010) 2625–31.

[9] **J.-S. Choi, W.-J. Son, J. Kim and W.-S. Ahn**. "Metal-organic framework MOF-5 prepared by microwave heating: factors to be considered". *Microporous and Mesoporous Materials* **116** (2008) 727–731.

[10] **Z.-Q. Li, L.-G. Qiu, T. Xu, Y. Wu, W. Wang, Z.-Y. Wu and X. Jiang**. "Ultrasonic synthesis of the microporous metal-organic framework $Cu_3(BTC)_2$ at ambient temperature and pressure: an efficient and environmentally friendly method". *Materials Letters* **63**(1) (2009) 78–80.

[11] **N. A. Khan, M. M. Haque and S. H. Jhung**. "Accelerated syntheses of porous isostructural lanthanide-benzenetricarboxylates (Ln-BTC) under ultrasound at room temperature". *European Journal of Inorganic Chemistry* **2010**(31) (2010) 4975–4981.

[12] **H. Yang, S. Orefuwa and A. Goudy**. "Study of mechanochemical synthesis in the formation of the metal-organic framework $Cu_3(BTC)_2$ for hydrogen storage". *Microporous and Mesoporous Materials* **143**(1) (2011) 37–45.

[13] **S. Kitagawa, R. Kitaura and S.-i. Noro**. "Functional porous coordination polymers". *Angewandte Chemie International Edition in English* **43**(18) (2004) 2334–2375.

[14] **Y. Qi, F. Luo, Y. Che and J. Zheng**. "Hydrothermal synthesis of metal-organic frameworks based on aromatic polycarboxylate and flexible bis(imidazole) ligands". *Crystal Growth & Design* **8**(2) (2008) 606–611.

[15] **J. An, S. J. Geib and N. L. Rosi**. "High and selective CO_2 uptake in a cobalt adeninate metal-organic framework exhibiting pyrimidine- and amino-decorated pores". *Journal of the American Chemical Society* **132**(1) (2010) 38–39.

[16] **K. Wang, H. Wang, Y. Bian and W. Li**. "Zn(II) metal-organic frameworks (MOFs) assembled from semirigid multicarboxylate ligands: synthesis, crystal structures, and luminescent properties". *Solid State Sciences* **12**(10) (2010) 1791–1796.

[17] **R. He, H. Song and Z. Wei**. "Manganese(II) and zinc(II) compounds via amino acid derivatives: effects of temperature and solvents". *Inorganica Chimica Acta* **363**(11) (2010) 2631–2636.

[18] **J.-G. Lin, Y.-Y. Xu, L. Qiu, S.-Q. Zang, C.-S. Lu, C.-Y. Duan, Y.-Z. Li, S. Gao and Q.-J. Meng**. "Ligand-to-metal ratio controlled assembly of nanoporous metal-organic frameworks." *Chemical Communications* (23) (2008) 2659–2661.

[19] **H. J. Park, D.-W. Lim, W. S. Yang, T.-R. Oh and M. P. Suh**. "A highly porous metal-organic framework: structural transformations of a guest-free MOF depending on activation method and temperature". *Chemistry - A European Journal* **17**(26) (2011) 7251–7602.

[20] **J.-R. Li, Y. Ma, M. C. McCarthy, J. Sculley, J. Yu, H.-K. Jeong, P. B. Balbuena and H.-C. Zhou**. "Carbon dioxide capture-related gas adsorption and separation in metal-organic frameworks". *Coordination Chemistry Reviews* **255**(15-16) (2011) 1791–1823.

[21] **H. K. Chae, D. Y. Siberio-Pérez, J. Kim, Y. Go, M. Eddaoudi, A. J. Matzger, M. O'Keeffe and O. M. Yaghi**. "A route to high surface area, porosity and inclusion of large molecules in crystals". *Nature* **427**(6974) (2004) 523–527.

[22] **G. Férey, C. Mellot-Draznieks, C. Serre, F. Millange, J. Dutour, S. Surblé and I. Margiolaki**. "A chromium terephthalate-based solid with unusually large pore volumes and surface area". *Science* **309**(5743) (2005) 2040–2043.

[23] **K. Koh, A. G. Wong-Foy and A. J. Matzger**. "A porous coordination copolymer with over 5000 m^2/g BET surface area." *Journal of the American Chemical Society* **131**(12) (2009) 4184–4185.

[24] **A. W. C. van den Berg and C. O. Areán**. "Materials for hydrogen storage: current research trends and perspectives". *Chemical Communications* (6) (2008) 668–681.

[25] **B. Panella, M. Hirscher, H. Pütter and U. Müller**. "Hydrogen adsorption in metal-organic frameworks: Cu-MOFs and Zn-MOFs compared". *Advanced Functional Materials* **16**(4) (2006) 520–524.

[26] **K. Sumida, J.-h. Her, M. Dincă, L. J. Murray, O. J. M. Schloss, C. J. Pierce, B. A. Thompson, S. A. Fitzgerald, C. M. Brown and J. R. Long**. "Neutron scattering and spectroscopic studies of hydrogen adsorption in $Cr_3(BTC)_2$ - a metal-organic framework with exposed Cr^{2+} Sites". *Journal of Physical Chemistry C* **115**(16) (2011) 8414–8421.

[27] **H. Furukawa, M. A. Miller and O. M. Yaghi**. "Independent verification of the saturation hydrogen uptake in MOF-177 and establishment of a benchmark for hydrogen adsorption in metal-organic frameworks". *Journal of Materials Chemistry* **17**(30) (2007) 3197–3204.

[28] **L. J. Murray, M. Dincă and J. R. Long**. "Hydrogen storage in metal-organic frameworks". *Chemical Society Reviews* **38**(5) (2009) 1294–1314.

[29] **C. M. Brown, Y. Liu, T. Yildirim, V. K. Peterson and C. J. Kepert**. "Hydrogen adsorption in HKUST-1: a combined inelastic neutron scattering and first-principles study". *Nanotechnology* **20**(20) (2009) 204025.

[30] **C. O. Arean, B. Bonelli, M. R. Delgado and E. Garrone**. "Hydrogen storage via physisorption: the combined role of adsorption enthalpy and entropy". *Turkish Journal of Chemistry* **33**(5) (2009) 599–606.

[31] **A. R. Millward and O. M. Yaghi**. "Metal-organic frameworks with exceptionally high capacity for storage of carbon dioxide at room temperature". *Journal of the American Chemical Society* **127**(51) (2005) 17998–17999.

[32] **H. Wu, J. M. Simmons, G. Srinivas, W. Zhou and T. Yildirim**. "Adsorption sites and binding nature of CO_2 in prototypical metal-organic frameworks: a combined neutron diffraction and first-principles study". *The Journal of Physical Chemistry Letters* **1**(13) (2010) 1946–1951.

[33] **P. D. C. Dietzel, V. Besikiotis and R. Blom**. "Application of metal-organic frameworks with coordinatively unsaturated metal sites in storage and separation of methane and carbon dioxide". *Journal of Materials Chemistry* **19**(39) (2009) 7362–7370.

[34] **R. Vaidhyanathan, S. S. Iremonger, K. W. Dawson and G. K. H. Shimizu**. "An amine-functionalized metal organic framework for preferential CO_2 adsorption at low pressures". *Chemical Communications* (35) (2009) 5230–5232.

[35] **Y. Liu, J.-H. Her, A. Dailly, A. J. Ramirez-Cuesta, D. A. Neumann and C. M. Brown**. "Reversible structural transition in MIL-53 with large temperature hysteresis". *Journal of the American Chemical Society* **130**(35) (2008) 11813–11818.

[36] **Z. Wang and S. M. Cohen**. "Modulating metal-organic frameworks to breathe: a postsynthetic covalent modification approach". *Journal of the American Chemical Society* **131**(46) (2009) 16675–16677.

[37] **S. Keskin, T. M. van Heest and D. S. Sholl**. "Can metal-organic framework materials play a useful role in large-scale carbon dioxide separations?" *ChemSusChem* **3**(8) (2010) 879–891.

[38] **A. Demessence, D. M. D'Alessandro, M. L. Foo and J. R. Long**. "Strong CO_2 binding in a water-stable, triazolate-bridged metal-

organic framework functionalized with ethylenediamine". *Journal of the American Chemical Society* **131**(25) (2009) 8784–8786.

[39] **M. Eddaoudi, J. Kim, N. Rosi, D. Vodak, J. Wachter, M. O'Keeffe and O. M. Yaghi**. "Systematic design of pore size and functionality in isoreticular MOFs and their application in methane storage". *Science* **295**(5554) (2002) 469–72.

[40] **N. Lamia, M. Jorge, M. A. Granato, F. A. Almeida Paz, H. Chevreau and A. E. Rodrigues**. "Adsorption of propane, propylene and isobutane on a metal-organic framework: molecular simulation and experiment". *Chemical Engineering Science* **64**(14) (2009) 3246–3259.

[41] **S. Wang, Q. Yang and C. Zhong**. "Adsorption and separation of binary mixtures in a metal-organic framework Cu-BTC: a computational study". *Separation and Purification Technology* **60**(1) (2008) 30–35.

[42] **A. Corma, H. García and F. X. Llabrés i Xamena**. "Engineering metal-organic frameworks for heterogeneous catalysis". *Chemical Reviews* **110**(8) (2010) 4606–4655.

[43] **F. X. Llabrés i Xamena, A. Abad, A. Corma and H. Garcia**. "MOFs as catalysts: activity, reusability and shape-selectivity of a Pd-containing MOF". *Journal of Catalysis* **250**(2) (2007) 294–298.

[44] **L. Alaerts, E. Séguin, H. Poelman, F. Thibault-Starzyk, P. A. Jacobs, D. E. De Vos and E. Séguin**. "Probing the Lewis acidity and catalytic activity of the metal-organic framework $[Cu_3(btc)_2]$ (BTC=benzene-1,3,5-tricarboxylate)". *Chemistry - A European Journal* **12**(28) (2006) 7353–7363.

[45] **C. Prestipino, L. Regli, J. G. Vitillo, F. Bonino, A. Damin, C. Lamberti, A. Zecchina, P. L. Solari, K. O. Kongshaug and**

S. Bordiga. "Local Structure of framework Cu(II) in HKUST-1 metallorganic framework: spectroscopic characterization upon activation and interaction with adsorbates". *Chemistry of Materials* **18**(5) (2006) 1337–1346.

[46] **M. Dincă, A. Dailly, Y. Liu, C. M. Brown, D. A. Neumann and J. R. Long**. "Hydrogen storage in a microporous metal-organic framework with exposed Mn^{2+} coordination sites". *Journal of the American Chemical Society* **128**(51) (2006) 16876–16883.

[47] **D. N. Dybtsev, A. L. Nuzhdin, H. Chun, K. P. Bryliakov, E. P. Talsi, V. P. Fedin and K. Kim**. "A homochiral metal-organic material with permanent porosity, enantioselective sorption properties, and catalytic activity". *Angewandte Chemie International Edition in English* **45**(6) (2006) 916–920.

[48] **B. Gomez-Lor, E. Gutiérrez-Puebla, M. Iglesias, M. A. Monge, C. Ruiz-Valero and N. Snejko**. "$In_2(OH)_3(BDC)_{1.5}$ (BDC = 1,4-benzenedicarboxylate): an In(III) supramolecular 3D framework with catalytic activity". *Inorganic Chemistry* **41**(9) (2002) 2429–2432.

[49] **M. Banerjee, S. Das, M. Yoon, H. J. Choi, M. H. Hyun, S. M. Park, G. Seo and K. Kim**. "Postsynthetic modification switches an achiral framework to catalytically active homochiral metal-organic porous materials". *Journal of the American Chemical Society* **131**(22) (2009) 7524–7525.

[50] **S. Hasegawa, S. Horike, R. Matsuda, S. Furukawa, K. Mochizuki, Y. Kinoshita and S. Kitagawa**. "Three-dimensional porous coordination polymer functionalized with amide groups based on tridentate ligand: selective sorption and catalysis". *Journal of the American Chemical Society* **129**(9) (2007) 2607–2614.

[51] **L. E. Kreno, K. Leong, O. K. Farha, M. Allendorf, R. P. Van Duyne and J. T. Hupp**. "Metal-organic framework materials as chemical sensors". *Chemical Reviews* **112**(2) (2012) 1105–11025.

[52] **M. D. Allendorf, C. A. Bauer, R. K. Bhakta and R. J. T. Houk**. "Luminescent metal-organic frameworks". *Chemical Society Reviews* **38**(5) (2009) 1330–1352.

[53] **M. Du, X.-J. Jiang and X.-J. Zhao**. "Molecular tectonics of mixed-ligand metal-organic frameworks: positional isomeric effect, metal-directed assembly, and structural diversification". *Inorganic Chemistry* **46**(10) (2007) 3984–3995.

[54] **X.-l. Wang, Y.-F. Bi, H.-y. Lin and G.-c. Liu**. "Three novel Cd(II) metal-organic frameworks constructed from mixed ligands of dipyrido[3,2-*d*:2,3-*f*]quinoxaline and benzene-dicarboxylate: from a 1-D ribbon, 2-D layered network, to a 3-D architecture". *Crystal Growth & Design* **7**(6) (2007) 1086–1091.

[55] **C. Serre, F. Millange, C. Thouvenot, N. Gardant, F. Pellé and G. Férey**. "Synthesis , characterisation and luminescent properties of a new three-dimensional lanthanide trimesate: M($(C_6H_3)(CO_2)_3$) (M = Y, Ln) or MIL-78". *Journal of Materials Chemistry* **14**(10) (2004) 1540–1543.

[56] **P. C. R. Soares-Santos, L. Cunha-Silva, F. A. Almeida Paz, R. A. Sá Ferreira, J. Rocha, T. Trindade, L. D. Carlos and H. I. S. Nogueira**. "Photoluminescent 3D lanthanide-organic frameworks with 2,5-pyridinedicarboxylic and 1,4-phenylenediacetic acids". *Crystal Growth & Design* **8**(7) (2008) 2505–2516.

[57] **W.-H. Zhu, Z.-M. Wang and S. Gao**. "Two 3D porous lanthanide-fumarate-oxalate frameworks exhibiting framework dynamics and luminescent change upon reversible de- and rehydration." *Inorganic Chemistry* **46**(4) (2007) 1337–1342.

[58] **Y. K. Park, S. B. Choi, H. Kim, K. Kim, B.-H. Won, K. Choi, J.-s. Choi, W.-s. Ahn, N. Won, S. Kim, D. H. Jung, S.-h. Choi, G.-h. Kim, S.-s. Cha, Y. H. Jhon, J. K. Yang and J. Kim**. "Crystal structure and guest uptake of a mesoporous metal-organic

framework containing cages of 3.9 and 4.7 nm in Diameter". *Angewandte Chemie International Edition in English* **46**(43) (2007) 8230 –8233.

[59] **B. D. Wagner, G. J. Mcmanus, B. Moulton and M. J. Zaworotko**. "Exciplex fluorescence of $\{[Zn(bipy)_{1.5}(NO_3)_2]\cdot CH_3OH\cdot 0.5pyrene\}_n$: a coordination polymer containing intercalated pyrene molecules (bipy = 4,4'-bipyridine)". *Chemical Communications* (18) (2002) 2176–2177.

[60] **Z.-Z. Lu, R. Zhang, Y.-Z. Li, Z.-J. Guo and H.-G. Zheng**. "Solvatochromic behavior of a nanotubular metal-organic framework for sensing small molecules". *Journal of the American Chemical Society* **133**(12) (2011) 4172–4174.

[61] **L. G. Beauvais, M. P. Shores and J. R. Long**. "Cyano-bridged Re_6Q_8 (Q = S, Se) cluster-cobalt(II) framework materials : versatile solid chemical sensors". *Journal of the American Chemical Society* **122**(12) (2000) 2763–2772.

[62] **G. Lu and J. T. Hupp**. "Metal-organic frameworks as sensors: a ZIF-8 based Fabry-Pérot device as a selective sensor for chemical vapors and gases". *Journal of the American Chemical Society* **132**(23) (2010) 7832–7833.

[63] **L. E. Kreno, J. T. Hupp and R. P. Van Duyne**. "Metal-organic framework thin film for enhanced localized surface plasmon resonance gas sensing". *Analytical Chemistry* **82**(19) (2010) 8042–8046.

[64] **M. Meilikhov, K. Yusenko, D. Esken, S. Turner, G. Van Tendeloo and R. a. Fischer**. "Metals@MOFs - loading MOFs with metal nanoparticles for hybrid functions". *European Journal of Inorganic Chemistry* **2010**(24) (2010) 3701–3714.

[65] **M. S. El-Shall, V. Abdelsayed, A. E. R. S. Khder, H. M. A. Hassan, H. M. El-Kaderi, T. E. Reich and J. Hu**. "Metallic

and bimetallic nanocatalysts incorporated into highly porous coordination polymer MIL-101". *Journal of Materials Chemistry* **19**(41) (2009) 7625–7631.

[66] **R. J. Kuppler, D. J. Timmons, Q.-R. Fang, J.-R. Li, T. A. Makal, M. D. Young, D. Yuan, D. Zhao, W. Zhuang and H.-C. Zhou**. "Potential applications of metal-organic frameworks". *Coordination Chemistry Reviews* **253**(23-24) (2009) 3042–3066.

[67] **P. Horcajada, C. Serre, M. Vallet-Regí, M. Sebban, F. Taulelle and G. Férey**. "Metaloorganic frameworks as efficient materials for drug delivery". *Angewandte Chemie International Edition in English* **45**(36) (2006) 5974–5978.

[68] **I. J. Bruno, J. C. Cole, P. R. Edgington, M. Kessler, C. F. Macrae, P. McCabe, J. Pearson and R. Taylor**. "New software for searching the Cambridge Structural Database and visualizing crystal structures". *Acta Crystallographica Section B: Structural Science* **58**(3) (2002) 389–397.

[69] **F. H. Allen**. "The Cambridge Structural Database: a quarter of a million crystal structures and rising". *Acta Crystallographica Section B: Structural Science* **58**(3) (2002) 380–388.

[70] **H.-P. Xiao, M.-L. Hu and X.-H. Li**. "Bis[bis(1,10-phenanthroline) chlorocopper(II)]benzene-1,2,4,5-tetracarboxylate(2-) dihydrate". *Acta Crystallographica Section E: Structure Reports Online* **60**(1) (2003) m71–m72.

[71] **A. M. Baruah, A. Karmakar and J. B. Baruah**. "Hydrolytic ring opening reactions of anhydrides for first row transition metal dicarboxylate complexes". *Polyhedron* **26**(15) (2007) 4518–4524.

[72] **J. Cho, A. J. Lough and J. Chang**. "Monomeric and polymeric copper(II) hexaaza macrocyclic complexes with btc anions (btc = 1,2,4,5-benzenetetracarboxylic acid)". *Inorganica Chimica Acta* **342** (2003) 305–310.

[73] **J. Yuan, H. Xiao and M. Hu**. "Crystal structure of μ-benzene-1,2,4,5-tetracarboxylato-bis[bis(1,10-phenanthroline) copper(II)]benzene-1,2,4,5-tetracarboxylic acid solvate, $[Cu(C_{12}H_8N_2)_2$ $C_{10}H_2O_8]\cdot C_{10}H_6O_8$". *Zeitschrift für Kristallographie - New Crystal Structures* **219**(3) (2004) 224–226.

[74] **J. C. Kim, A. J. Lough and H. Jo**. "Syntheses and X-ray crystal structures of 14-membered tetraaza macrocyclic copper(II) complexes with polycarboxylate ligands". *Inorganic Chemistry Communications* **5**(8) (2002) 616–620.

[75] **W. Chen, N. Tioh, J. Zou, Z. Xu and X. You**. "A tetracarboxylatobenzene-bridged binuclear copper(II) complex". *Acta Crystallographica Section C: Crystal Structure Communications* **52**(1) (1996) 43–45.

[76] **S. S. Massoud, F. A. Mautner, F. R. Louka, S. Demeshko, S. Dechert and F. Meyer**. "Diverse coordination of polynuclear copper(II) complexes constructed from benzene tetracarboxylates". *Inorganica Chimica Acta* **370**(1) (2011) 435–443.

[77] **Y. Y. Karabach, A. M. Kirillov, M. Haukka, J. Sanchiz, M. N. Kopylovich and A. J. L. Pombeiro**. "Multicopper(II) pyromellitate compounds: self-assembly synthesis, structural topologies, and magnetic features". *Crystal Growth & Design* **8**(11) (2008) 4100–4108.

[78] **D. Cheng, C. Feng, M. Hu, D. Xu, Y. Xu and Y. Zheng**. "Synthesis and crystal structure of a polymeric 1,2,4,5-benzenetetracarboxylato complex of Cu(II) with imidazole, $Cu_2(C_{10}H_2O_8)(C_3H_4N_2)_6(H_2O)_4\cdot 4H_2O$". *Journal of Coordination Chemistry* **52**(3) (2006) 245–251.

[79] **W. Li-Ya, L.-C. Li, L. Dai-Zheng, Z.-H. Jiang and Y. Shi-Ping**. "Synthesis, crystal structure and magnetic properties of a 1-D polymer, $[Cu(NITpPy)_2(H_2TCB)(H_2O)]\cdot 2H_2O$". *Chinese Journal of Chemistry* **21**(5) (2003) 500–504.

[80] **Q. Shi, R. Cao, D.-F. Sun, M.-C. Hong and Y.-C. Liang**. "Solvothermal syntheses and crystal structures of two metal coordination polymers with double-chain structures". *Polyhedron* **20**(28) (2001) 3287–3293.

[81] **J. C. Kim, H. Jo, A. J. Lough, J. Cho, U. Lee and S. Y. Pyun**. "Polymeric nickel(II) and copper(II) complexes with btc^{2-} ions as bridging ligands (btc^{2-}=1,2,4,5-benzenetetracarboxylic acid dianion)". *Inorganic Chemistry Communications* **6**(5) (2003) 474–477.

[82] **Y. Y. Karabach, A. M. Kirillov, M. Haukka, M. N. Kopylovich and A. J. L. Pombeiro**. "Copper(II) coordination polymers derived from triethanolamine and pyromellitic acid for bioinspired mild peroxidative oxidation of cyclohexane". *Journal of Inorganic Biochemistry* **102**(5-6) (2008) 1190–1194.

[83] **Y. Yang, H.-L. Wang, N. Liang, B.-L. Li and Y. Zhang**. "Syntheses and structures of two hydrogen bonding frameworks with bis(triazole) and 1,2,4,5-benzenetetracarboxylate". *Journal of Molecular Structure* **929**(1-3) (2009) 73–78.

[84] **M. D. Stephenson and M. J. Hardie**. "Extended structures of transition metal complexes of 6,7-dicyanodipyridoquinoxaline: π-stacking, weak hydrogen bonding, and CN—π interactions". *Crystal Growth & Design* **6**(2) (2006) 423–432.

[85] **K. Brown, S. Zolezzi, P. Aguirre, D. Venegas-Yazigi, V. Paredes-García, R. Baggio, M. A. Novak and E. Spodine**. "$[Cu(H_2btec)(bipy)]_\infty$: a novel metal-organic framework (MOF) as heterogeneous catalyst for the oxidation of olefins". *Dalton Transactions* (8) (2009) 1422–1427.

[86] **E.-C. Yang, Y. Feng, Z.-Y. Liu, T.-Y. Liu and X.-J. Zhao**. "Diverse mixed-ligand metal complexes with in situ generated 5-(pyrazinyl)tetrazolate chelating-bridging ligand: *in situ* synthesis, crys-

tal structures, magnetic and luminescent properties". *CrystEngComm* **13**(1) (2011) 230.

[87] **N. Ohata, H. Masuda and O. Yamauchi**. "Aromatic carboxylate-controlled self-organization of copper(II)-L-arginine complexes". *Inorganica Chimica Acta* **286**(1) (1999) 37 – 45.

[88] **C. C. Corrêa, L. B. Lopes, L. H. dos Santos, R. Diniz, M. I. Yoshida, L. F. de Oliveira and F. C. Machado**. "Four new coordination polymers involving transition metals with 1,2,4,5-benzenetetracarboxylate and pyridyl-donor ligand di(4-pyridyl) sulfide". *Inorganica Chimica Acta* **367**(1) (2011) 187–193.

[89] **Z.-Q. Liu, Y.-T. Li, Z.-Y. Wu and S.-F. Zhang**. "$[Cu_4(H_2O)_4(dmapox)_2(btc)]_n \cdot 10nH_2O$: The first two-dimensional polymeric copper(II) complex with bridging μ-trans-oxamidate and μ_4-1,2,4,5-benzentetracarboxylato ligands: synthesis, crystal structure and DNA binding studies". *Inorganica Chimica Acta* **362**(1) (2009) 71–77.

[90] **A. Majumder, V. Gramlich, G. M. Rosair, S. R. Batten, J. D. Masuda, M. S. E. Fallah, J. Ribas, J.-P. Sutter, C. Desplanches and S. Mitra**. "Five new cobalt(II) and copper(II)-1,2,4,5-benzenetetracarboxylate supramolecular architectures: syntheses, structures, and magnetic properties". *Crystal Growth & Design* **6**(10) (2006) 2355–2368.

[91] **M. L. Hu, H. P. Xiao, S. Wang and X. H. Li**. "*Catena*-poly[[(1,10-phenanthroline-κ^2 N,N)copper(II)]-μ-(dihydrogen benzene-1,2,4,5-tetracarboxylato)-κ^2O^1:O^4]". *Acta Crystallographica Section C: Crystal Structure Communications* **59**(11) (2003) m454–m455.

[92] **B. Usubaliev, A. Shnulin and K. S. Mamedov**. "Crystal and molecular structure of a decahydrate complex of copper with 1,2,4,5-benzenetetracarboxylic acid". *Koordinatsionnaya Khimiya (Russian Journal of Coordination Chemistry)* **8** (1982) 1532–1538.

[93] **N. Zhang, M.-X. Li, Z.-X. Wang, M. Shao and S.-R. Zhu**. "Synthesis, structures and thermal stabilities of five copper(II) coordination polymers based on 2,4,6-tris(pyridyl)-1,3,5-triazine and 1,2,4,5-benzenetetracarboxylate ligands". *Inorganica Chimica Acta* **363**(1) (2010) 8–14.

[94] **E.-C. Yang, W. Feng, J.-Y. Wang and X.-J. Zhao**. "Crystal structure, thermal stability and theoretical investigation on four 1,3-bis(1,2,4-triazol-1-yl)propane-based copper(II) complexes". *Inorganica Chimica Acta* **363**(2) (2010) 308–316.

[95] **P. Wang, C. N. Moorefield, M. Panzer and G. R. Newkome**. "Helical and polymeric nanostructures assembled from benzene tri- and tetracarboxylic acids associated with terpyridine copper(II) complexes". *Chemical Communications* (4) (2005) 465–467.

[96] **S. Gehring, I. W. Haase and I. B. Nuber**. "Moderately strong intramolecular magnetic exchange interaction between the copper(II) ions separated by 11.25 Å in $[L_2Cu_2(OH_2)_2(\mu\text{-terephthalto})](ClO_4)_2$ (L = 1,4,7-trimethyl-1,4,7-triazacyclononane)". *Journal of the American Chemical Society* **110**(11) (1988) 3657–3658.

[97] **J. Yang, J.-F. Ma, Y.-Y. Liu, J.-C. Ma and S. R. Batten**. "A series of Cu(II) complexes based on different bis(imidazole) ligands and organic acids: formation of water clusters and fixation of atmospheric carbon dioxide". *Crystal Growth & Design* **8**(12) (2008) 4383–4393.

[98] **W. Li, M.-X. Li, M. Shao, Z.-X. Wang and H.-J. Liu**. "Ferromagnetic and mixed-valence copper coordination polymers assembled by polycarboxylates and 2,6-bis(1,2,4-triazolyl)pyridine". *Inorganic Chemistry Communications* **11**(9) (2008) 954–957.

[99] **C. C. Corrêa, R. Diniz, J. Janczak, M. I. Yoshida, L. F. de Oliveira and F. C. Machado**. "High dimensional coordination polymers based on transition metals, 1,2,4,5-benzenetetracarboxylate

anion and 1,3-bis(4-pyridyl)propane nitrogen ligand". *Polyhedron* **29**(16) (2010) 3125–3131.

[100] **G.-L. Wen, Y.-Y. Wang, P. Liu, C.-Y. Guo, W.-H. Zhang and Q.-Z. Shi**. "A series of 1-D to 3-D metal-organic coordination architectures assembled with V-shaped bis(pyridyl)thiadiazole under co-ligand intervention". *Inorganica Chimica Acta* **362**(6) (2009) 1730–1738.

[101] **D. Cheng, M. A. Khan and R. P. Houser**. "Copper(II) and cobalt(II) coordination polymers with bridging 1,2,4,5-benzenetetracarboxylate and N-methylimidazole: coordination number-determined sheet topology". *Journal of the Chemical Society, Dalton Transactions* (24) (2002) 4555–4560.

[102] **R. Cao, Q. Shi, D. Sun, M. Hong, W. Bi and Y. Zhao**. "Syntheses and characterizations of copper(II) polymeric complexes constructed from 1,2,4,5-benzenetetracarboxylic acid". *Inorganic Chemistry* **41**(23) (2002) 6161–6168.

[103] **F.-P. Huang, J.-L. Tian, W. Gu and S.-P. Yan**. "Three 3D Cu(II) coordination polymers constructed from 1,2,4,5-benzenetetracarboxylate acid and three positional isomeric ligands". *Inorganic Chemistry Communications* **13**(1) (2010) 90–94.

[104] **S. K. Ghosh and P. K. Bharadwaj**. "Puckered-boat conformation hexameric water clusters stabilized in a 2D metal-organic framework structure built from Cu(II) and 1,2,4,5-benzenetetracarboxylic acid". *Inorganic chemistry* **43**(17) (2004) 5180–5182.

[105] **H.-Y. Lin, B. Mu, X.-L. Wang, J. Li and G.-C. Liu**. "Synthesis, structure and electrochemical property of a new copper(II) complex based on benzene-1,2,4,5-tetracarboxylate and 2,5-bis(3-pyridyl)-1,3,4-oxadiazole ligands". *Journal of Chemical Crystallography* **41**(5) (2011) 635–640.

[106] **J. Yang, J.-F. Ma, Y.-Y. Liu, S.-L. Li and G.-L. Zheng**. "Four novel 3D copper(II) coordination polymers with different topologies". *European Journal of Inorganic Chemistry* **2005**(11) (2005) 2174–2180.

[107] **M.-X. Li, Z.-X. Miao, M. Shao, S.-W. Liang and S.-R. Zhu**. "Metal-organic frameworks constructed from 2,4,6-tris(4-pyridyl)-1,3,5-triazine". *Inorganic Chemistry* **47**(11) (2008) 4481–4489.

[108] **A. L. Spek**. *PLATON, a multipurpose crystallographic tool*. Utrecht University, Utrecht (2005).

[109] **Zhong-xiang, J.-x. Li and J.-h. Qin**. "Crystal structure of *catena*-(hexakis(2-aqua)-diaqua-disodium(I) copper(II) bis(μ_2-dihydrogen-1,2,4,5-benzenetetracarboxylate-O,O')) dihydrate, $Na_2Cu(H_2O)_8(C_{10}H_4O_8)_2{\cdot}2H_2O$". *Zeitschrift für Kristallographie - New Crystal Structures* **223**(1) (2008) 105–106.

[110] **J. H. Luo, C. C. Huang, X. H. Huang and X. J. Chen**. "Two pseudo-polymorphic copper-benzene-1,2,4,5-tetracarboxylate complexes". *Acta Crystallographica Section C: Crystal Structure Communications* **C63** (2007) m273–276.

[111] **M. Rafizadeh, V. Amani, L. Dehghan, F. Azadbakhta, E. Sahlolbeia, F. Azadbakht and E. Sahlolbei**. "Poly[ethylenediammonium [cuprate(II)-μ_4-benzene-1,2,4,5-tetracarboxylato-$\kappa^4O:O':O'':O'''$] 2.5-hydrate]". *Acta Crystallographica Section E: Structure Reports Online* **63**(7) (2007) m1841–m1842.

[112] **R. Diniz, H. A. de Abreu, W. B. de Almeida, M. T. C. Sansiviero and N. G. Fernandes**. "X-ray crystal structure of triaquacopper(II) dihydrogen 1,2,4,5-benzenetetracarboxylate trihydrate and raman spectra of Cu^{2+}, Co^{2+} , and Fe^{2+} salts of 1,2,4,5-benzenetetracarboxylic (pyromellitic) Acid". *European Journal of Inorganic Chemistry* **2002**(5) (2002) 1115–1123.

[113] **J.-Y. Guo, T.-L. Zhang, J.-G. Zhang, Z.-J. Qiao, L. Yang, W. Yu and R.-F. Wu**. "Non-isothermal kinetics and crystal structure of one-dimensional coordination polymer $\{[Cu(H_2bttc)(H_2O)_3]\cdot 3H_2O\}_n$". *Chinese Journal of Inorganic Chemistry* **22**(12) (2006) 2179–2185.

[114] **S. S. Chui, S. M. Lo, J. P. H. Charmant, A. G. Orpen and I. D. Williams**. "A chemically functionalizable nanoporous material $[Cu_3(TMA)_2(H_2O)_3]_n$". *Science* **283**(4530) (1999) 1148–1150.

[115] **S.-F. Si, R.-J. Wang and Y.-D. Li**. "Synthesis and crystal structure of three dimensional complex from copper(II) and 1,2,4,5-benzenetetracarboxylate". *Inorganic Chemistry Communications* **6**(8) (2003) 1152–1155.

[116] **D. W. Breck**. *Zeolite molecular sieves: structure, chemistry, and use.* 1st edition. Wiley, New York (1973).

[117] **D. Poleti and L. Karanović**. "1,3-Propanediammonium [μ_4-1,2,4,5-benzenetetracarboxylato(4-)]copper(II) dihydrate with a microporous structure". *Journal of the Serbian Chemical Society* **70**(12) (2005) 1441–1450.

[118] **E. Lamprecht**. *Thermal, spectroscopic and X-ray diffraction studies of copper(II) 1,2,4,5,-benzenetetracarboxylates and copper(II) oxalate: a study of metal-organic frameworks.* Ph.D. thesis, Rhodes University (2008).

[119] **M. Coombes**. *Synthesis , characterisation and computational study of the copper-based metal-organic framework* $Cu_2Na(OH)B_4C\cdot 7H_2O$. Honours Project Report, Rhodes University, Grahamstown (2010).

[120] **H. K. Henisch**. *Crystal growth in gels.* Dover Publications, Mineola (1996).

[121] **D. A. Skoog, D. M. West, F. J. Holler and S. R. Crouch**. *Fundamentals of analytical chemistry*. 8th edition. Thomson Brooks/Cole (2004).

[122] **B. Welz**. *Atomic absorption spectroscopy*. 1st edition. Verlag Chemie, Weinheim (1976).

[123] **W. Price**. *Spectrochemical analysis by atomic absorption*. Heyden Son Ltd., London (1979).

[124] **K. Nakamoto**. *Infrared and raman spectra of inorganic and coordination compounds*. Third edition. John Wiley & Sons, Inc., New York (1978).

[125] **F. D. Bloss**. *Crystallography and crystal chemistry*. Holt, Rinehart and Winston, Inc., New York (1971).

[126] **W. F. de Jong**. *General crystallography: a brief compendium*. W.H. Freeman and Company, New York (1959).

[127] **P. J. Haines**. *Thermal methods of analysis: principles, applications and problems*. 1st edition. Blackie Academic and Professional, an imprint of Chapman Hall, Glasgow (1995).

[128] **H. Oswald and H. Wiedemann**. "Factors influencing thermoanalytical curves". *Journal of Thermal Analysis* **12**(2) (1977) 147–168.

[129] **M. E. Brown**. *Introduction to thermal analysis techniques and applications*. 2nd edition. Kluwer Academic Publishers, Dordrecht (2001).

[130] **S. Ma and H.-C. Zhou**. "Gas storage in porous metal-organic frameworks for clean energy applications". *Chemical Communications* **46**(1) (2010) 44–53.

[131] **R. A. Scott and C. M. Lukehart** (editors). *Applications of physical methods to inorganic and bioinorganic chemistry*. 1st edition. John Wiley & Sons Ltd. (2007).

[132] **T. G. Rochow and E. G. Rochow**. *An introduction to microscopy by means of light, electrons, X-rays, or ultrasound.* 2nd edition. Plenum Press, New York (1979).

[133] **M. J. Frisch, G. W. Trucks, H. B. Schlegel, G. E. Scuseria, M. A. Robb, J. R. Cheeseman, J. A. Montgomery Jr, T. Vreven, K. N. Kudin, J. C. Burant, J. M. Millam, S. S. Iyengar, J. Tomasi, V. Barone, B. Mennucci, M. Cossi, G. Scalmani, N. Rega, G. A. Petersson, H. Nakatsuji, M. Hada, M. Ehara, K. Toyota, R. Fukuda, J. Hasegawa, M. Ishida, T. Nakajima, Y. Honda, O. Kitao, H. Nakai, M. Klene, X. Li, J. E. Knox, H. P. Hratchian, J. B. Cross, V. Bakken, C. Adamo, J. Jaramillo, R. Gomperts, R. E. Stratmann, O. Yazyev, A. J. Austin, R. Cammi, C. Pomelli, J. W. Ochterski, P. Y. Ayala, K. Morokuma, G. A. Voth, P. Salvador, J. J. Dannenberg, V. G. Zakrzewski, S. Dapprich, A. D. Daniels, M. C. Strain, O. Farkas, D. K. Malick, A. D. Rabuck, K. Raghavachari, J. B. Foresman, J. V. Ortiz, Q. Cui, A. G. Baboul, S. Clifford, J. Cioslowski, B. B. Stefanov, G. Liu, A. Liashenko, P. Piskorz, I. Komaromi, R. L. Martin, D. J. Fox, T. Keith, M. A. Al-Laham, C. Y. Peng, A. Nanayakkara, M. Challacombe, P. M. W. Gill, B. Johnson, W. Chen, M. W. Wong, C. Gonzalez and J. A. Pople**. *Gaussian 03, Revision E.01.* Gaussian, Inc., Wallingford CT (2004).

[134] **CPMD**. *http://www.cpmd.org/*. Copyright IBM Corp (1990-2008) Copyright MPI für Festkörperforschung Stuttgart (1997-2001).

[135] **P. Pulay**. "Convergence acceleration of iterative sequences. The case of SCF iteration". *Chemical Physics Letters* **73**(2) (1980) 393–398.

[136] **V. Eyert**. "A comparative study on methods for convergence acceleration of iterative vector sequences". *Journal of Computational Physics* **124**(2) (1996) 271–285.

[137] **W. Humphrey, A. Dalke and K. Schulten**. "VMD: Visual Molecular Dynamics". *Journal of Molecular Graphics* **14**(1) (1996) 33–38.

[138] **J. M. Goodman**. *Chemical applications of molecular modelling*. 1st edition. The Royal Society of Chemistry, Cambridge (1998).

[139] **A. R. Leach**. *Molecular modelling: principles and applications*. 2nd edition. Pearson Education Limited, Harlow (2001).

[140] **R. Car and M. Parrinellow**. "Unified approach for molecular dynamics and density-functional theory". *Physical Review Letters* **55**(22) (1985) 2471–2474.

[141] **A. Walton**. *Molecular and crystal structure models*. 1st edition. Ellis Horwood Limited, Chichester (1978).

[142] **A. A. Coelho**. *TOPAS-Academic, version 4.1*. Coelho Software, Brisbane (2007).

[143] **A. C. Thompson, J. Kirz, D. T. Attwood, E. M. Gullikson, M. R. Howells, J. B. Kortright, Y. Liu, A. L. Robinson, J. H. Underwood, K.-J. Kim, I. Lindau, P. Pianetta, H. Winick, G. P. Williams and J. H. Scofield**. *X-ray Data Booklet*. 3rd edition. Lawrence Berkeley National Laboratory, California (2009).

[144] **M. Yin, C.-K. Wu, Y. Lou, C. Burda, J. T. Koberstein, Y. Zhu and S. O'Brien**. "Copper oxide nanocrystals". *Journal of the American Chemical Society* **127**(26) (2005) 9506–9511.

[145] **Y. Zhu, W.-Y. Wang, M.-W. Guo, G. Li and H.-j. Lu**. "An unprecedented 1-D mixed-valence Cu(II)/Cu(I) metal-organic framework bearing 2-phenyl imidazole dicarboxylates". *Inorganic Chemistry Communications* **14**(9) (2011) 1432–1435.

[146] **C. F. Macrae, I. J. Bruno, J. A. Chisholm, P. R. Edgington, P. McCabe, E. Pidcock, L. Rodriguez-Monge, R. Taylor, J. van de Streek and P. A. Wood**. "Mercury CSD 2.0 - new features

for the visualization and investigation of crystal structures". *Journal of Applied Crystallography* **41**(2) (2008) 466–470.

[147] **S. Asbrink and L.-J. Norrby**. "A refinement of the crystal structure of copper(II) oxide with a discussion of some exceptional e.s.d.'s". *Acta Crystallographica Section B: Structural Science* **26**(1) (1970) 8–15.

[148] **H. R. Oswald, A. Reller, H. W. Schmalle and E. Dubler**. "Structure of copper(II) hydroxide, $Cu(OH)_2$". *Acta Crystallographica Section C: Crystal Structure Communications* **46**(12) (1990) 2279–2284.

[149] **H. M. Rietveld**. "Line profiles of neutron powder-diffraction peaks for structure refinement". *Acta Crystallographica* **22** (1967) 151–152.

[150] **C. L. Carnes, J. Stipp, K. J. Klabunde and J. Bonevich**. "Synthesis , characterization , and adsorption studies of nanocrystalline copper oxide and nickel oxide". *Langmuir* **18**(4) (2002) 1352–1359.

[151] **R. C. Weast** (editor). *Handbook of chemistry and physics*. 51st edition. The Chemical Rubber Co., Cleveland (1971).

[152] **T. Boublík, V. Fried and E. Hála**. *The vapour pressures of pure substances*. 1st edition. Elsevier Scientific Publishing Company, Amsterdam (1973).

[153] **T. Boublík, V. Fried and E. Hála**. *The vapour pressure of pure substances - vol. 17*. Elsevier, Amsterdam (1984).

[154] **V. Majer and V. Svoboda**. *Enthalpies of vaporization of organic compounds*. 1st edition. Blackwell Scientific Publications, Oxford (1985).

[155] **R. M. Silverstein, F. X. Webster and D. J. Kiemle**. *Spectrometric identification of organic compounds*. 7th edition. John Wiley & Sons, Inc. (2005).

[156] **R. P. Pohanish**. *Sittig's handbook of toxic and hazardous chemicals and carcinogens*. 6th edition. Elsevier Inc., Kidlington, Oxford (2012).

[157] **T. Jacobs, R. Clowes, A. I. Cooper and M. J. Hardie**. "A chiral, self-catenating and porous metal-organic framework and its post-synthetic metal uptake". *Angewandte Chemie International Edition in English* **51**(21) (2012) 5192–5195.

[158] **A. Rabenau**. "The role of hydrothermal synthesis in preparative chemistry". *Angewandte Chemie International Edition in English* **24**(12) (1985) 1026–1040.

[159] **J. Y. Lu**. "Crystal engineering of Cu-containing metal-organic coordination polymers under hydrothermal conditions". *Coordination Chemistry Reviews* **246**(1-2) (2003) 327–347.

[160] **L. Alderighi, P. Gans, A. Ienco, D. Peters, A. Sabatini and A. Vacca**. "Hyperquad simulation and speciation (HySS): a utility program for the investigation of equilibria involving soluble and partially soluble species". *Coordination Chemistry Reviews* **184**(1) (1999) 311–318.

[161] **W. Maxwell and J. Partington**. "The dissociation constants of some polybasic acids. - part III". *Transactions of the Faraday Society* **33** (1937) 670–678.